Copyright Warning & Restrictions

The copyright law of the United States (Title 17, United States Code) governs the making of photocopies or other reproductions of copyrighted material.

Under certain conditions specified in the law, libraries and archives are authorized to furnish a photocopy or other reproduction. One of these specified conditions is that the photocopy or reproduction is not to be "used for any purpose other than private study, scholarship, or research." If a, user makes a request for, or later uses, a photocopy or reproduction for purposes in excess of "fair use" that user may be liable for copyright infringement,

This institution reserves the right to refuse to accept a copying order if, in its judgment, fulfillment of the order would involve violation of copyright law.

Please Note: The author retains the copyright while the New Jersey Institute of Technology reserves the right to distribute this thesis or dissertation

Printing note: If you do not wish to print this page, then select "Pages from: first page # to: last page #" on the print dialog screen

NJIT
New Jersey's Science & Technology University

The Van Houten library has removed some of the personal information and all signatures from the approval page and biographical sketches of theses and dissertations in order to protect the identity of NJIT graduates and faculty.

ABSTRACT

MODELING HYDROGEN DIFFUSION FOR SOLAR CELL PASSIVATION AND PROCESS OPTIMIZATION

by
Yi Zhang

A diffusion model for hydrogen (H) in crystalline silicon was established which takes into account the charged state conversion, junction field, mobile traps, and complex formation and dissociation at dopant and trap sites. Carrier exchange among the various charged species is a "fast" process compared to the diffusion process. A numerical method was developed to solve the densities of various charged species from the Poisson's equation that involves shallow-level dopants and one "negative U" impurity, e.g., H. Time domain implicit method was adopted in finite difference scheme to solve the fully coupled equations.

Limiting versions of the model were applied to the problems that are of interest to photovoltaics. Simplified trap-limited model was used to describe the low temperature diffusion profiles, assuming process-induced traps, a constant bulk trap level, and trapping / detrapping mechanisms. The results of the simulation agreed with those obtained from experiments. The best fit yielded a low surface free H concentration, C_s, ($\sim 10^{14}$ cm^{-3}) from high temperature extrapolated diffusivity value. In the case of ion beam hydrogenation, mobile traps needed to be considered. PAS analysis showed the existence of vacancy-type defects in implanted Si substrates. Simulation of hydrogen diffusion in p-n junction was first attempted in this work. The order of magnitude of C_s ($\sim 10^{14}$ cm^{-3}) was confirmed. Simulation results showed that the preferred charged state of H is H^- (H^+) in n^- (p^-) side of the junction. The accumulation of H^- (H^+) species on n^+ (p^+) side of the n^+-p (p^+-n) junction was observed, which could retard the diffusion in junction. The diffusion of hydrogen through heavily doped region in a junction is trap-limited. Several popular hydrogenation techniques were evaluated by means of modeling and experimental observations. In particular, PECVD followed by RTP hydrogenation was found to be two-step process: PECVD deposition serves as a predeposition step of H and during RTP anneal step, H is released from the surface traps and redistributed into the bulk.

MODELING HYDROGEN DIFFUSION FOR SOLAR CELL PASSIVATION AND PROCESS OPTIMIZATION

by
Yi Zhang

A Dissertation
Submitted to the Faculty of
New Jersey Institute of Technology and
Rutgers, the State University of New Jersey-Newark
In Partial Fulfillment of the Requirements for the Degree of
Doctor of Philosophy in Applied Physics

Federated Physics Department

January 2002

Copyright © 2002 by Yi Zhang

ALL RIGHTS RESERVED

APPROVAL PAGE

MODELING HYDROGEN DIFFUSION FOR SOLAR CELL PASSIVATION AND PROCESS OPTIMIZATION

Yi Zhang

Dr. Nuggehalli M. Ravindra, Dissertation Advisor — Date
Professor of Physics, NJIT

Dr. Bhushan Sopori, Dissertation Co-advisor — Date
Principal Engineer, NCPV, NREL, CO

Dr. Earl D. Shaw, Committee Member — Date
Professor and Chairman, Rutgers University-Newark, NJ

Dr. John C. Hensel, Committee Member — Date
Distinguished Research Professor of Physics, NJIT

Dr. Anthony T. Fiory, Committee Member — Date
Research Professor of Physics, NJIT

Dr. Oktay H. Gokce, Committee Member — Date
Special Lecturer of Physics, NJIT

Dr. Suffian M. Abedrabbo, Committee Member — Date
Member of Technical Staff, Kirana Networks, NJ

BIOGRAPHCAL SKETCH

Author: Yi Zhang

Degree: Doctor of Philosophy

Date: January 2002

Undergraduate and Graduate Education:

- Doctor of Philosophy in Applied Physics,
  New Jersey Institute of Technology and Rutgers, Newark, NJ, 2001

- Bachelor of Science in Physics
  Shanghai University of Science of Technology, Shanghai, P. R. China, 1995

Major: Applied Physics

Presentations and Publications:

Y. Zhang, B. L. Sopori, R. Reedy, K. Jones and N. M. Ravindra,
"Modeling low-temperature diffusion of H in Si: influence of impurities and defects," 11th Workshop on Crystalline Silicon Solar Cell materials and Processes: Extended Abstracts and Papers from the Workshop held 19-22 August 2001, Estes Park, CO, pp. 279-284.

Y. Zhang, N. M. Ravindra and B. L. Sopori,
"Interface states and H(D) passivation at Si-SiO2 interface," 10th Workshop on Crystalline Silicon Solar Cell materials and Processes: Extended Abstracts and papers from the Workshop, August 2000, Copper Mountain, CO, pp. 241-246.

B. L. Sopori, Y. Zhang, and N. M. Ravindra,
"Si device processing in H-ambients: H-diffusion mechanisms and influence on electronic properties," J. Electronic Mat. **30**, 1616 (2001).

B. L. Sopori and Y. Zhang,
"H-diffusion mechanism(s) in PECVD-passivation of solar cells," Proc. 2001 NCPV Program Review Meeting, October 2001, Lakewood, CO, pp. 301-302.

Y. Zhang, B. Sopori, R. Reedy and K. Jones,
"Modeling low-temperature diffusion of H in Si," to be submitted to Appl. Phys. Lett.

To my beloved family

ACKNOWLEDGMENT

The work presented in this dissertation was suggested and supervised by my advisors, Dr. Bhushan Sopori at NREL and Prof. Nuggehalli M. Ravindra at NJIT. I am deeply grateful for their valuable advice and encouragement.

This work is supported by the U. S. Department of Energy under Contract No. DE-AC36-00G010337 and by the DOE Center of Excellence for Advanced Materials Processing. I am also very grateful to Kim Jones and Robert Reedy at the Measurement and Characterization Division of NREL for their support of TEM and SIMS analyses.

I owe many thanks to Prof. Michael J. Stavola, Department of Physics, Lehigh University, for the stimulating discussion about hydrogen theory and modeling in Silicon.

Thanks also go to Prof. Xiaochuan Cai, Department of Computer Science, University of Colorado at Boulder, and Dr. Kent Paul, Solid State Theory Group, at NREL, for their advice on advanced numerical computation techniques, without which the effective implementation of the diffusion model would not have been possible.

I benefited greatly from the advice and insights of the members of my Dissertation and Oral Examination Committees - Prof. Earl D. Shaw of Rugters, John C. Hensel, Anthony T. Fiory, Oktay H. Gokce of NJIT and Suffian M. Abedrabbo from Kirana Networks. I am very thankful to Dr. Haijiang Ou for his friendship and helpful discussions. I also acknowledge the support of Dr. Wei Chen during my initial stages at NREL. Sincere thanks also go to Amol Deshmukh, Joe Vinod Kumar Albert and Narashihan Chakravarthy for their assistance in editing this thesis.

Last, but not least, I would especially like to thank my dear wife, Yongmei Huang, and my friends and family members for their strong support of my work and my life.

TABLE OF CONTENTS

Chapter **Page**

1 INTRODUCTION... 1

1.1 Introduction to Solar Cells.. 1

1.2 Solar Cell Performance and Limiting Factors.................................. 3

1.3 Role of Defects and Hydrogenation in PV Materials.......................... 10

1.4 Dissertation Outline.. 15

2 HYDROGEN IN SILICON: A REVIEW.. 17

2.1 Introduction to Hydrogen in Semiconductors................................... 17

2.2 Hydrogenation Techniques... 18

2.2.1 Introduction.. 18

2.2.2 Ion Bean Hydrogenation... 18

2.2.3 Plasma Methods... 20

2.2.4 Electrochemical Techniques.. 22

2.2.5 Forming Gas Anneal.. 23

2.3 Ion Beam Depth Profiling Techniques... 24

2.4 Isolated Hydrogen in Silicon... 26

2.5 Hydrogen Passivation of Crystalline Defects in Silicon...................... 30

2.6 Hydrogen Interactions with Shallow Level Dopants........................... 31

2.7 Hydrogen Interactions with Other Impurities in Silicon...................... 34

2.8 Hydrogen Diffusion in Silicon.. 35

2.8.1 Diffusivity and Solubility of Hydrogen in Silicon.............. 35

TABLE OF CONTENTS
(Continued)

Chapter **Page**

2.8.2 Theoretical Framework....... 37

2.8.3 Past Research on H Diffusion in PV Silicon Materials....... 48

3 MODELING OF HYDROGEN DIFFUSION IN CRYSTALINE SILICON....... 55

3.1 Introduction to Modeling of Hydrogen Diffusion in Silicon....... 55

3.2 Formulation of the "Complete" Diffusion Model....... 58

3.2.1 Solving Poisson's Equation with Dual-level "Negative-U" Impurity....... 61

3.2.2 Convergence of the Method....... 66

3.2.3 Solving Hydrogen Diffusion Problem....... 69

3.2.4 1-D Mesh and 3-point Asymmetric Numerical Difference....... 72

3.3 Trap-limited Hydrogen Diffusion at Low Temperatures....... 74

3.3.1 Review and Introduction....... 74

3.3.2 Formulation of Trap-limited Diffusion....... 77

3.3.3 Numerical Solution – Finite Difference Scheme....... 79

3.3.4 Simulation and Discussion....... 81

3.4 Mobile-Traps in Hydrogen Diffusion....... 86

3.4.1 Formulation of the Limiting case....... 86

3.4.2 Experimental Observations....... 87

3.4.3 Discussion....... 89

3.5 Hydrogen Diffusion p-n Junction....... 93

4 UNDERSTANDING HYDROGENATION PROCESSES....... 104

TABLE OF CONTENTS
(Continued)

Chapter **Page**

4.1 Forming Gas Anneal Passivation.. 104

4.2 Ion Beam Passivation by Kaufman Source.. 108

4.3 PECVD – RTP Passivation.. 113

5 CONCLUSIONS AND FUTURE DIRECTION.. 124

5.1 Conclusion on Hydrogen Diffusion and Process Modeling.......................... 124

5.2 Future Direction.. 127

REFERENCES.. 129

LIST OF TABLES

Table **Page**

2.1 Values of the energy (per H atom) of H configuration in Si [137]...................... 24

2.2 Ion beam depth profiling techniques, their detection limits and depth resolutions.... 25

3.1 Expressions of 3-point asymmetric first-order finite difference 73

3.2 Expressions of 3-point asymmetric second-order finite difference 74

3.3 Dose of total trap injection and diffusivity of mobile traps.............................. 90

LIST OF FIGURES

Figure **Page**

1.1 Cross section of a typical silicon solar cell 2

1.2 Energy band and quasi-Fermi levels in a p-n junction under illumination............. 4

1.3 The idealized equivalent circuit of a solar cell... 6

1.4 Current-voltage characterization curve for an illuminated solar cell.................... 7

1.5 A generalized two-terminal semiconductor device.. 9

1.6 Percentage increase in cell efficiency with PECVD nitride AR coating compared to no coating.. 14

1.7 The effect of Al and FGA treatment on efficiency and IQE of EFG cells [41]........ 15

2.1 Schematic of a typical plasma hydrogenation system...................................... 20

2.2 A sketch of the Si lattice showing important interstitial sites, after Ref. [76].......... 27

2.3 Illustration of H bonding with an acceptor in Si.. 32

2.4 The broken-bond T_d site model of donor-hydrogen complex in silicon [99].......... 33

2.5 Diffusivity of H reported by various researchers... 36

2.6 Transition diagram of different charge states of an impurity in semiconductor, given the co-existence of both donor and acceptor levels.................................. 39

2.7 Hydrogen diffusion profiles for (a) LRC ribbon, (b) FZ, (c) CZ, and (d) EFG ribbon, by ion implantation... 49

2.8 Apparent diffusivities fitted for materials grown with different methods.............. 49

2.9 Schematic representation of the diffusion mechanism for the (V, H) pair in Si........ 52

3.1 Flowchart diagram that illustrates the steps of solving fully coupled differential equations by numerical method.. 71

LIST OF FIGURES
(Continued)

Figure **Page**

3.2 Illustration of structure and notations of a mesh.. 73

3.3 Experimental deuterium profiles (dotted lines) of a plasma-deuterated, n-type Si, at 200°C, fitted with erfc.. 81

3.4 Experimental deuterium profiles (dotted lines) of a plasma-deuterated, n-type Si, at 200°C, fitted with the current model... 82

3.5 Experimental data of Ref. [162] (dotted lines) and fitted with $R_c = 10$ A, $C_s = 2.75 \times 10^{14}$ cm^{-3}, $T = 200$°C, 15 min, B doping = 1.3×10^{18} cm^{-3}................ 83

3.6 Experimental and calculated profiles: deuterium was implanted at 1.5 KeV, at 250 °C for 30 min. Parameters used were $Nt_b = 1.2 \times 10^{17}$ cm^{-3}, $k_th' = 0.1$ s^{-1}.... 85

3.7 PAS depth profiles on Si-ribbon at two locations on the sample, a H-implanted Si ribbon and for comparison FZ grown defect free silicon with a native oxide on the surface.. 88

3.8 Hydrogen diffusion profiles fitted with fixed + mobile trap distribution.............. 91

3.9 SIMS profile of total deuterium density across p-n junctions formed by Implanting phosphorus into a (100) silicon wafer uniformly doped with 10^{17} boron per cm^3 for various times of deuteration at 150 °C. Deuteration was from downstream gases from a plasma discharge... 95

3.10 SIMS profile of total deuterium density in three composite samples subjected to 2 hour deuteration in the downstream product from a hydrogen plasma discharge at 300°C. All samples had a substrate containing 8×10^{18} B/cm^3, which was covered with expitaxial layers containing 8×10^{18}, 3×10^{18}, 5×10^{17} As/cm^3, respectively, to form n-p junctions.. 96

3.11 Simulation of H diffusion in an n^+-p junction with the parameters: T = 300°C, $(E_d - E_i) = 0.36$ eV, $(E_i - E_a) = - 0.20$ eV, $D_0 = 5.82 \times 10^{-7}$, $D_+ = 5.82 \times 10^{-7}$, $D_- = 2.91 \times 10^{-7}$, cm^{2}s^{-1}, $k_{DH}' = 3.54 \times 10^3$ s^{-1}, $k_{AH}' = 1.56 \times 10^3$ s^{-1}, t = 0.04 s. Dotted curves are the dopant profiles.. 100

3.12 Simulation of H diffusion in an n^+-p junction with the parameters: T = 300°C, $(E_d - E_i) = 0.36$ eV, $(E_i - E_a) = - 0.20$ eV, $D_0 = 5.82 \times 10^{-7}$, $D_+ = 5.82 \times 10^{-7}$, $D_- = 2.91 \times 10^{-7}$, cm^{2}s^{-1}, $k_{DH}' = 3.54 \times 10^3$ s^{-1}, $k_{AH}' = 1.56 \times 10^3$ s^{-1}, t = 0.4 s. Dotted curves are the dopant profiles.. 101

LIST OF FIGURES
(Continued)

Figure **Page**

3.13 Simulation of H diffusion in a p+-n junction with the parameters: T = 300°C, $(E_d - E_i) = 0.36$ eV, $(E_i - E_a) = - 0.20$ eV, $D_0 = 5.82 \times 10^{-7}$, $D_+ = 5.82 \times 10^{-7}$, $D_- = 2.91 \times 10^{-7}$, cm^2s^{-1}, $k_{DH}' = 3.54 \times 10^3\ s^{-1}$, $k_{AH}' = 1.56 \times 10^3\ s^{-1}$, t = 0.04 s. Dotted curves are the dopant profiles.......... 102

3.14 Simulation of H diffusion in a p+-n junction with the parameters: T = 300°C, $(E_d - E_i) = 0.36$ eV, $(E_i - E_a) = - 0.20$ eV, $D_0 = 5.82 \times 10^{-7}$, $D_+ = 5.82 \times 10^{-7}$, $D_- = 2.91 \times 10^{-7}\ cm^2s^{-1}$, $k_{DH}' = 3.54 \times 10^3\ s^{-1}$, $k_{AH}' = 1.56 \times 10^3\ s^{-1}$, t = 0.4 s. Dotted curves are the dopant profiles.......... 103

4.1 SIMS deuterium profiles of an LRC ribbon treated with a forming gas anneal. Surface damage was created by a grit size of 0.2, 0.1, 0.05, and 0.01 µm, respectively.......... 104

4.2 SIMS H/D profiles of an n^+-p junction treated in FGA at 400°C for 1 hour.......... 105

4.3 ASE Americas substrate of p/n junction with 0.03-µm grit followed by a D_2 FGA at 400°C for 1 hour.......... 106

4.4 XTEM photos of hydrogenated Si samples, showing segregation of H at the dislocations (a) and along a grain boundary (b). 109

4.5 XTEM photo showing defects generated near the surface by a 1.5 KeV H-implantation. 110

4.6 XTEM photos showing (a) series of platelets in edge-on position and (b) tilted configuration.......... 111

4.7 Steps used in backside hydrogenation by using Kaufman ion source and RTP.......... 112

4.8 Total H concentration in predeposition at 300ºC, $N_b = 10^{17}\ cm^{-3}$, $C_s = 2.75 \times 10^{14}\ cm^{-3}$, Rc = 10 A, k' = 0.2 s^{-1}, t = 6 min.......... 120

4.9 Total H concentration in 800ºC anneal after 300ºC predeposition, $N_b = 10^{17}\ cm^{-3}$, $J_s = 0$, $R_c = 10$ A, k' = 40 s^{-1}.......... 120

4.10 Untrapped H concentration in 800ºC anneal after 300ºC predeposition, $N_b = 10^{17}\ cm^{-3}$, $J_s = 0$, $R_c = 10$ A, k' = 40 s^{-1}.......... 121

4.11 Untrapped H concentration in 800ºC anneal, $N_b = 10^{16}\ cm^{-3}$, $J_s = 0$, $R_c = 1$ A, k' = 40 s^{-1}.......... 121

LIST OF FIGURES
(Continued)

Figure **Page**

4.12 Predeposition at 300ºC, $N_b = 10^{16}$ cm^{-3}, C_s=2.75 × 10^{14} cm^{-3}, R_c = 10 A, k' = 0.2 s^{-1}, t = 6 min........ 122

4.13 Total H concentration in 800ºC anneal after 300ºC predeposition, $N_b = 10^{16}$ cm^{-3}, J_s = 0, R_c = 1 A, k' = 40 s^{-1}........ 122

4.14 Calculated reflectance from Si/Buffer interface of Si/Buffer/Al back reflector structure. (a) shows the noncoherent component same for both 0.4- and 1.0-μm thick buffer layer. (b) and (c) show the coherent component for 0.4- and 1.0-μm thick buffer layer, respectively........ 123

CHAPTER 1

INTRODUCTION

1.1 Introduction to Solar Cells

It is amazing that the ultimate energy source for survival and prosperity of human beings is the sun. Sunlight keeps the earth warm and replenishes oxygen in the air with the help of green plants. Before this modern industrialization, everything on earth was clean and natural. Activities of mankind, however, have created many environmental problems. Most of the energy currently being used comes from coal, oil or natural gas. They are all fossil fuels, an ancient form of solar energy formed by the decay of plants and animals over millions of years. By burning fossil fuel products, enormous pollution is being created that disturbs the ecological system. Related issues include deteriorating air quality, pollution-related diseases, and global warming. Furthermore, fossil fuels are not renewable, and they are being exploited at a rate faster than they can be replenished.

Since this world depends heavily on energy, new sources of energy are needed that can last a long time. If possible, they should never run out, or are renewable. The new energy sources should produce as little pollution as possible and be environmentally friendly. A good candidate is the electrical power obtained directly from sunlight using photovoltaic (PV) effect.

Solar cell is a PV device fabricated using semiconductor materials. The main task of cell design is to obtain as high an energy-conversion efficiency as possible to deliver electricity into a suitable external load. Heinrich Hertz first studied the effect in solids, such as selenium, in the 1870s. In 1951, a grown p-n junction device of germanium was fabricated, but the PV effect in CdS [1] was reported only in 1954 by Rappaport, Loferski

and Jenny at RCA. Major improvement in cell design occurred in 1960s and 1970s. Solar cells readily found their applications in space as well as in terrestrial use.

Figure 1.1 illustrates the structure of a single-junction solar cell [2]. The n-type emitter is formed by a very thin heavily doped region. Front Ohmic contact is made to the emitter in a way such that the series resistance is small and as much light falls on the front side as possible. Ohmic contact is also made on the backside of the cell. An anti-reflection (AR) coating is deposited by sputtering or evaporation methods. Solar cell companies, such as ASE Americas, routinely use plasma enhanced chemical vapor deposition (PECVD) to deposit a silicon nitride (SiN) layer on their cells [3]. The thickness and refractive index of this layer are optimized such that the light lost by reflection from the front surface is reduced to a minimum. On top of the AR coating layer is usually an encapsulation glass cover with additional AR and ultraviolet rejection filters for the purpose of preventing high-energy radiative particles from reaching and degrading the device.

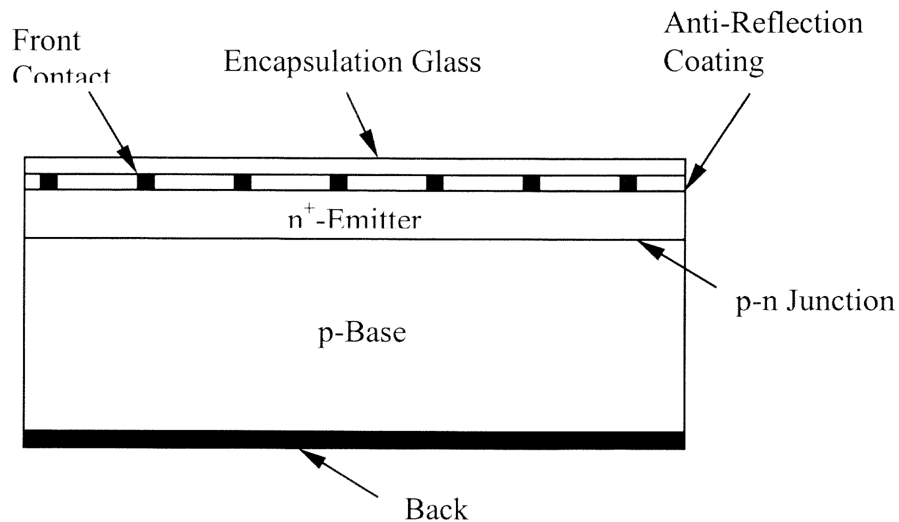

Figure 1.1 Cross section of a typical silicon solar cell.

Currently, solar cells are based on a number of semiconductor materials. The ideal solar cell efficiency at 300 K was theoretically calculated as a function of energy bandgap under one sun AM1.5 [4]. The efficiency has a broad maximum and the material with a bandgap between 1 and 2 eV can all be considered. Some examples are Si, a-Si:H, InP, GaAs, CdTe, copper indium gallium diselenide (CIGS). However, one of the concerns in production line is the cost of the material. To lower the cost, new crystal growth approaches have been developed including using casting process, the edge-defined film-fed growth (EFG) technique, the ribbon-to-ribbon process, and the dendrite-web process [5].

There has been a dilemma for the silicon solar cell manufacturers for years about the need for low-cost material and processing. On one hand, the cost of materials has to be low enough to be profitable; on the other hand, low-grade materials usually possess unwanted impurities and defects that compromise the cell efficiency. Discussion of the solar cell parameters and the limiting factors is presented in the next section.

1.2 Solar Cell Performance and Limiting Factors

The basic form of solar cell consists of a p-n junction with front and back contacts. When isolated, the majority carrier is hole in p-type material and electron in n-type material. As the two types of semiconductors are brought together, concentration gradient of carriers near the metallurgical junction leads to a carrier flow. As the junction region gets "depleted" of carriers, the ionized dopant cores left behind build up an electric field across the junction, which induces "drift current" that is opposite to the diffusion current. An equilibrium situation will be obtained as the two currents match.

In the dark, the equilibrated p-n junction should have a spatially uniform Fermi level and no net current flow is observed.

When a p-n junction is illuminated, excess electron-hole pairs are generated by light throughout the cell. This disturbs the equilibrium state of carriers in the p-n junction. The excess electrons (hole) in n-type (p-type) region then diffuse towards the junction and are quickly pulled across the depletion region by the electric field. Fermi-Dirac statistics has been assumed valid in non-equilibrium cases.

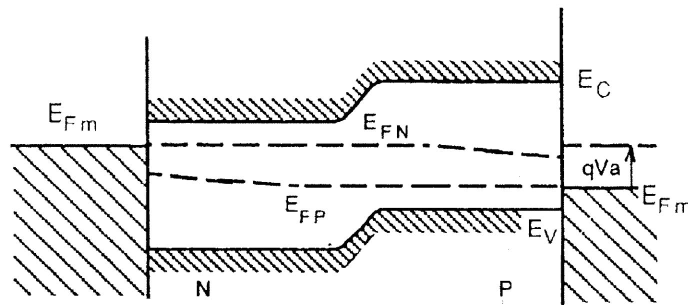

Figure 1.2 Energy band and quasi-Fermi levels in a p-n junction under illumination.

Figure 1.2 illustrates the quasi-Fermi levels (imrefs, or electrochemical potentials) of electrons and holes of a non-equilibrium p-n junction under illumination. In the bulk quasi-neutral regions, the majority carrier imrefs are approximately constant, because their concentrations are large and only small gradients can support large current flows. If the carrier recombination at depletion region is negligible, imrefs across the junction can be assumed to be constant. The photo-generated carriers that flow across the depletion region constitute the major contributions to the light-generated current, I_L. This contribution is primarily from a region within a minority carrier diffusion length on either

side of the depletion region. The excess carriers generated recombine locally with majority carriers and scarcely contribute to I_L.

The accumulation of light-generated carriers produces a forward biased p-n junction. Rigorous solutions can be obtained by solving the following steady-state carrier transport equations, provided heavy doping effect is negligible.

- Current transport equations:

$$\vec{j}_n = n\mu_n \nabla E_f^n \tag{1.1}$$

$$\vec{j}_p = p\mu_p \nabla E_f^p \tag{1.2}$$

- Continuity equations:

$$\nabla \cdot \vec{j}_p = -\nabla \cdot \vec{j}_n = e(G - U) \tag{1.3}$$

- Poisson equation:

$$\nabla^2 \phi = \frac{e}{\varepsilon}\left(n + p_A^- - p - n_D^+\right) \tag{1.4}$$

- Carrier density equations:

$$n = n_i e^{\frac{1}{kT}\cdot\left(E_f^n - E_i\right)} \tag{1.5}$$

$$p = n_i e^{-\frac{1}{kT}\cdot\left(E_f^p - E_i\right)} \tag{1.6}$$

The symbols used here have their standard meanings and are as follows: j_n, electron current density; j_p, hole current density; n, electron density; p, hole density; μ_n, μ_p, electron and hole mobilities; ϕ, electron potential at E_i, ε, dielectric constant; e, electron charge; G, photogeneration rate per unit volume; U, net recombination rate per unit volume; p_A^-, ionized acceptor density; n_D^+, ionized donor density.

The equations need a set of boundary conditions, which usually consists of a relation between the projected surface minority current and the surface recombination rate. Terminal current can be extracted by integrating the projected total current density, $(j_n + j_p)$, over the terminal contact area. Terminal voltage will be the difference between the majority carrier imrefs at terminals given the contact voltage drop to be small.

Although the method solves the I-V behavior exactly, under low injection condition, superposition principle can be used to greatly simplify the solution. In such cases, the complete I-V curve can be written as the sum of light-generation current and the I-V characteristics of a diode. Figure 1.3 shows the corresponding equivalent circuit including a current source, I_L, connected in parallel with an ideal diode. A typical I-V characteristics curve [6] agrees well with this assumption and is shown in Figure 1.4 (a).

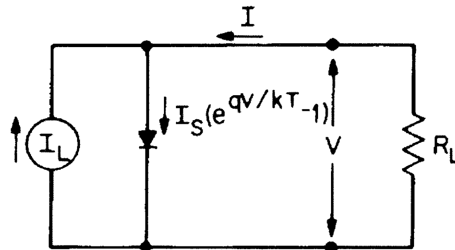

Figure 1.3 The idealized equivalent circuit of a solar cell.

In general, the I-V characteristics of a solar cell can be written as

$$I = I_s\left(e^{\frac{qV}{A_0 kT}} - 1\right) - I_L \tag{1.7}$$

where

$$I_s = AeN_c N_v\left(\frac{1}{N_A}\sqrt{\frac{D_n}{\tau_n}} + \frac{1}{N_D}\sqrt{\frac{D_p}{\tau_p}}\right)e^{-\frac{E_g}{kT}} \tag{1.8}$$

and

$$I_L = AeG(L_e + W + L_h).\tag{1.9}$$

I_s is the diode saturation current. A is area of the cell. D_n and D_p are the diffusivities of electron and hole in p- and n-type regions respectively. L_e and L_h are the minority carrier diffusion length in the respective p- and n-type regions. W is the depletion region width. A_0 is the perfection factor of the diode. For a "perfect" junction, A_0 is equal to 1 and open-circuit voltage (V_{oc}) reaches its highest values. The expression for I_s and I_L is exact for a single junction thick diode. For other cases, the qualitative relations are still valid.

The I-V curve passes through the fourth quadrant. The maximum power output corresponds to the maximum product of I and V as shown in Figure 1.4 (a). It is convenient to plot that quadrant only and invert the I-axis as shown in Figure 1.4 (b), after Ref. [7].

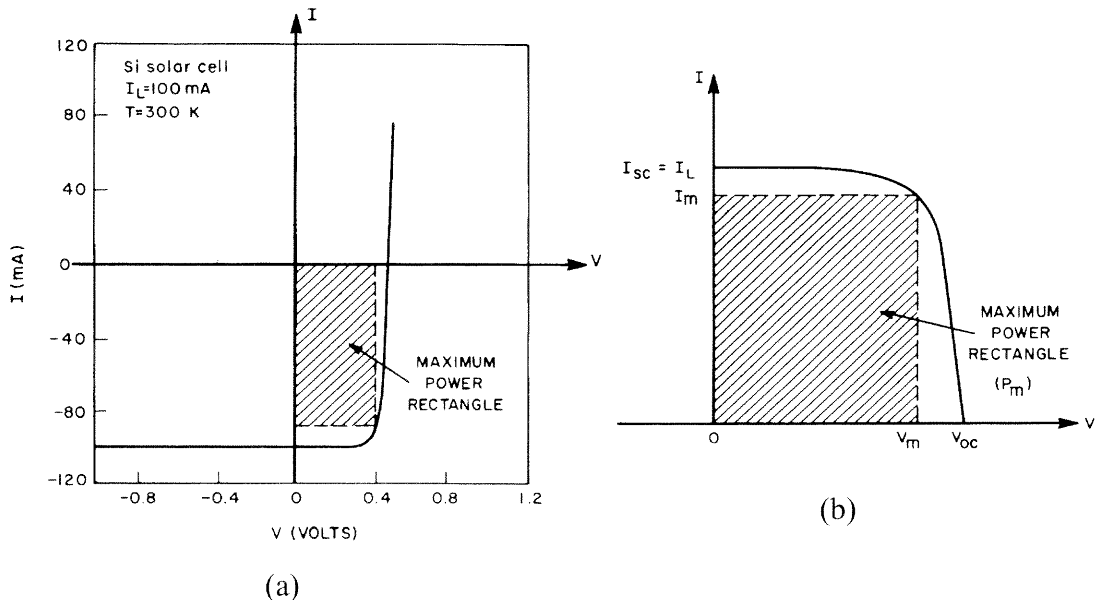

Figure 1.4 Current-voltage characterization curve for an illuminated solar cell.

Several important parameters can be extracted from the I-V curve to evaluate the performance of a solar cell:

- Open-circuit voltage (V_{oc}): the voltage of a solar cell when current $I = 0$. From Eq. (1.7), V_{oc} can be written as:

$$V_{oc} = A_0 \frac{kT}{e} \ln\left(\frac{I_{sc}}{I_s} + 1\right). \tag{1.10}$$

  The smaller the saturation current I_s, the greater the V_{oc}. From Eq. (1.8), I_s can be seen in connection with minority carrier recombination lifetimes, τ_p and τ_n. The greater the τ_p and τ_n, the smaller the I_s; and thus, the greater the V_{oc}.

- Short circuit current (I_{sc}): the current in a solar cell when applied voltage $V = 0$. From Eq. (1.7), I_{sc} is equal to light generated current, I_L, since I_L depends on the diffusion lengths of minority carriers. A longer lifetime material offers a greater I_L.

- Fill factor (FF): the ratio of the maximum power output at (V_{mp}, I_{mp}) to the product of V_{oc} and I_{sc}. Mathematically, it is defined as

$$FF = \frac{V_{mp} I_{mp}}{V_{oc} I_{sc}}. \tag{1.11}$$

  FF is a strong function of V_{oc} [8]. Recombination in depletion region and bulk can reduce FF [9].

- Energy-conversion efficiency (η) is given by

$$\eta = \frac{V_{mp} I_{mp}}{P_{in}} = \frac{V_{oc} I_{sc} FF}{P_{in}}. \tag{1.12}$$

  For a given total power input, the efficiency, η, depends on how large V_{oc}, I_{sc} or I_L, and FF one may get.

- Other parameters include series resistance, R_s, and shunt resistance, R_{sh}.

In order to improve the efficiency of a solar cell, all the above relations favor a reduced recombination or a long minority carrier recombination lifetime of the material. Swanson [10] used an integral method to relate the recombination activities to the terminal current, I, of a generalized two-terminal device shown in Figure 1.5. He proved that I could be written in the form

$$I = I_L - \left(I_{b,rec} + I_{s,rec} + I_{cont,rec}\right) \tag{1.13}$$

where photocurrent $I_L = e\int_V g dv$, bulk recombination current $I_{b,rec} = e\int_V r dv$, surface recombination current $I_s = \int_S \vec{j}_p \cdot \hat{n} dS$, and contact recombination current $I_{cont,rec} = \int_{S_2} \vec{j}_p \cdot \hat{n} dS - \int_{S_1} \vec{j}_n \cdot \hat{n} dS$.

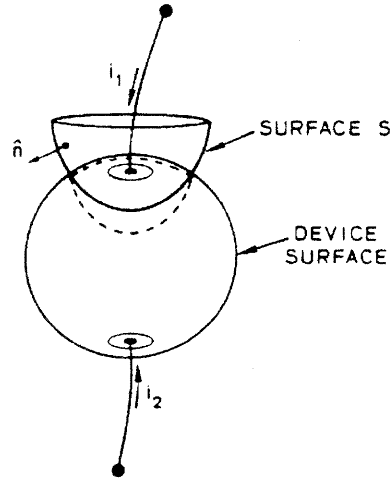

Figure 1.5 A generalized two-terminal semiconductor device.

Since all the negative terms in Eq. (1.13) are caused by recombination, abating recombination losses at surface and bulk is the key to improve the cell efficiency.

Whereas light generation can enhance the output voltage, the various sources of recombination prevent the voltage from reaching its ideal level.

One approach to obtain higher cell efficiency is to seek a higher level of light generation by using back reflector, light trapping and concentrator. Another approach is to improve the quality of material itself, because the minority carrier recombination at bulk, surface and the contact decreases the cell efficiency. For a given cell design, material quality is the limiting factor of cell performance.

1.3 Role of Defects and Hydrogenation in PV Materials

The quality of starting materials is an important topic in PV manufacturing industry. If the cost is not an issue, such as in the solar plane and space applications, high quality float-zone (FZ) silicon material can be used to fabricate solar cells. Laboratory cell efficiency as high as 24% under one-sun illumination has been achieved [11], [12]. FZ silicon based 21.9% bifacial cell [13] was installed on NASA funded aircraft "Helios" [14] that recently set a new altitude record. However, the market in terrestrial applications is more attractive to PV community because of its large scale. It is surprising that the demand in PV has a rapid annual growth rate of 25% [15] while the cost of production is expected to reduce towards 1 $/Wp in coming years [16]. Inevitably, low cost materials such as poly-crystalline silicon were adopted. Efficiency between 13% and 15% is now achievable in the production line. However, those materials usually contain a large amount of impurities and defects that adversely affect the minority carrier lifetime and thus the cell efficiencies.

Defects can be categorized in many ways. By using dimensionality as a criterion, defects may be grouped into point, line, area and volume type defects. By judging their interaction with growth environment, defects can be intrinsic as well as extrinsic. Intrinsic point defects include vacancies, interstitials and vacancy-interstitial pairs, which can be easily introduced during crystal growth. The most important factor controlling the grown-in point defect and micro-defect is the ratio v/G [17], [18], where v is the pulling rate and G is the near-surface axial temperature gradient. On further cooling, supersaturated vacancies (interstitials) may agglomerate into D-void-defects (A/B-swirl-defects), which are micro-volume defects. Growth of PV multicrystalline (mc) Si materials usually uses a high pulling rate, so they contain a higher level of vacancies than interstitials [19].

Unlike the intentional doping of shallow level impurities, metallic impurities may be incorporated without being noticed due to their high solubilities in silicon. Transition atoms, such as Fe, Co, Cr, Ni, Cu, in the silicon lattice are believed to introduce energy levels in the bandgap [20]. The carrier capture cross section was measured in Fe [21], [22] $\sim 4 \times 10^{-14}$ cm^2, in Ni [23] in a range from 2.7×10^{-15} to 10^{-20} cm^2, and in Cu [24] $\sim 10^{-17}$ cm^2. Problems arise when the isolated metallic impurities precipitate to form volume defects. Such precipitates enhance the minority carrier recombination and lead to junction shunting.

An important line defect is dislocation. Dislocations represent boundaries between slipped and unslipped regions of a crystal. The formation of dislocation lowers the total free energy to relieve the stress caused by temperature gradient in crystal growth. Dislocations in silicon may be dissociated into glide and be involved in the

deformation behavior of silicon [25]. As a result of elastic distortions associated with a dislocation, band bending occurs in its vicinity. Dangling bonds are also created along the core of the dislocation and introduce energy levels in the bandgap.

Grain boundaries are area-defects formed during crystal growth. In poly-crystalline silicon material grown by casting process, a large amount of grain boundaries can be seen. Grain boundaries may be treated as an assemblage of dislocations whose properties depend on the crystallography of the boundary. Their electrical activities are connected with the set of dislocations that constitute a boundary. In general, local stress field and dangling bonds are present at the kinks along a grain boundary [26]. The field and dangling bonds along the grain boundaries cause a distribution of energy levels in the bandgap and act as recombination centers. If the grain boundaries are decorated with metallic precipitates, they become electrically more active and can be detected with a strong contrast in electron beam induced current (EBIC) test. It has been shown that such precipitation occurs primarily at dislocation clusters and limits the efficiency of current mc-Si solar cells [27].

Electrically active defects and impurities pin discrete mid-gap energy and sometimes give rise to a continuous distribution of energy states in the bandgap. These mid-gap energy states can serve as traps for carriers. The successive capture of an electron and hole at a localized site creates a recombination event [28]. A material containing many recombination centers reduces minority carrier lifetime. For low-cost starting materials used in the production of inexpensive terrestrial cells, the detrimental energy levels need to be reduced. There are two practical approaches to arrive at this goal: “gettering” and “passivation”.

Gettering is a means of "physically" removing unwanted defects and impurities by applying the principle of segregation. Stress, intrinsic defects such as dislocations, and even surface damage can be introduced to create the gettering sites. These gettering sites act as sinks for unwanted defects and impurities due to their high solubilities at the sites. Phosphorus diffusion typically used for a solar cell fabrication is a well-established gettering process [29]. Likewise, Al alloying used for a back contact formation can also getter impurities.

Passivation is another effective way to reduce the number of recombination centers. In passivation, the defect states are effectively removed from the bandgap by neutralizing them with a suitable impurity. Hydrogen is one of the candidates for passivation and has been extensively used in device processing. For example, the post metallization anneal (PMA) routinely implemented in MOS device fabrication was found to greatly reduce the interfacial states and leakage current. The passivation of PV silicon by hydrogenation has been studied extensively in the past [30], [31]. Hydrogen can passivate dangling bonds, which was first observed in amorphous silicon (a-Si) by Pankove et al [32]. Hydrogenation provides excellent passivation of defects and impurities that have later been observed by many researchers, [33], [34], [35], [36].

Since hydrogen can favorably affect material properties, processes involving hydrogen passivation are being developed to improve starting material quality as well as the final device performance. At present, hydrogen is introduced during the anti-reflection (AR) coating deposition of a solar cell [37], [38]. An AR coating layer is used in a PV device to reduce the reflection losses which otherwise would occur due to the high reflectivity of air-silicon interface. Solar companies, specifically ASE Americas,

use a plasma enhanced chemical vapor deposition (PECVD) nitride anti-reflection coating (SiN) [3]. Figure 1.6 shows a difference of cell performance with such an AR coating process on polycrystalline material [39], [40]. This exemplifies a significant increase in efficiency. However, the reasons are not well understood.

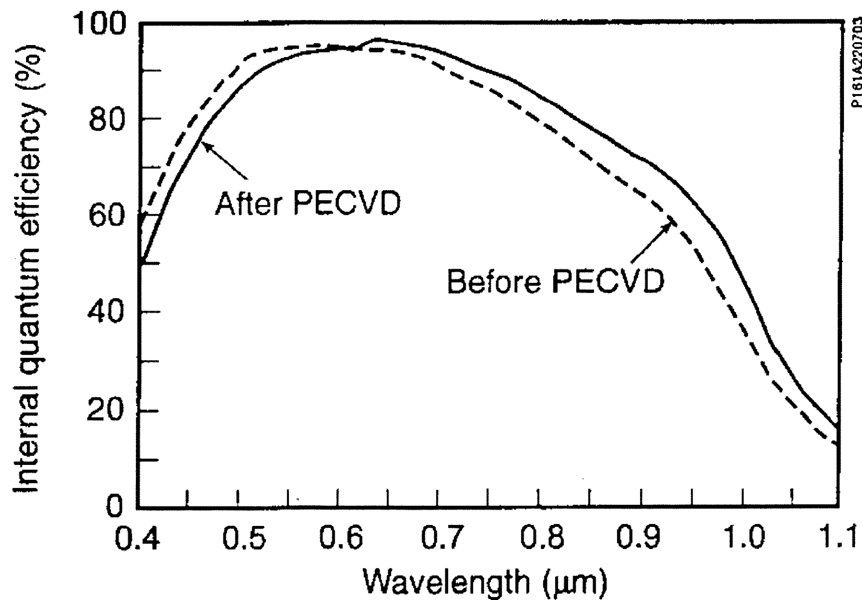

Figure 1.6 Percentage increase in cell efficiency with PECVD nitride AR coating compared to no coating [40].

Other studies have shown that a 400°C forming gas anneal (FGA) in the presence of Al increases the double-layer AR-coated EFG silicon cell efficiency from 7.8% to 14.1% [41] (in Figure 1.7). Although Al alloying plays a role of gettering impurities out of the active area, the benefit of hydrogen FGA remains a possibility. Ammor et al. [42] have done extensive studies on the role of FGA treatment on as-grown substrates. Previous studies of this group have shown that H can readily diffuse into a Si wafer if the sample has surface damage [43]. However, more investigations are still needed.

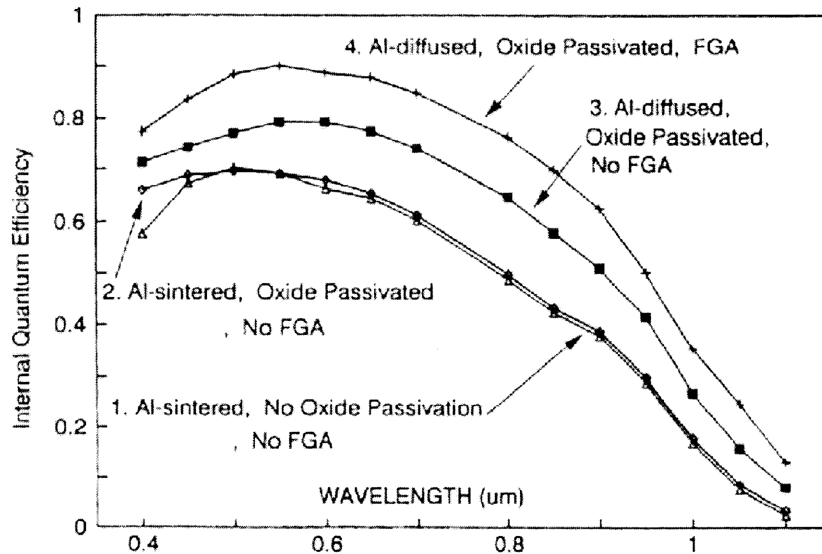

Figure 1.7 The effect of Al and FGA treatment on efficiency and IQE of EFG cells [41].

1.4 Dissertation Outline

Hydrogen diffusion and passivation is a pivotal topic in the PV community [44]. Reduction of defect levels is crucial for improving the cell efficiencies. Defects and impurity concentrations in silicon material vary from vendor to vendor. It has been observed that the actual hydrogen diffusion also depends on the specific material being used.

Hydrogen is a very active element; it readily interacts with the defects and impurities. However, before hydrogen can passivate the material at the desired depth, it has to reach there. The diffusion mechanism of hydrogen is very complicated. It not only depends on the processing time and temperature, but is also controlled by the amount and the type of traps it interacts with during the diffusion process. Under certain conditions, the charge state conversion and field effect also have an influence on the diffusion process. Much work needs to be done to understand the role of hydrogen in

silicon. The diffusion theory of hydrogen and several modeling efforts will be described in great detail.

In PV mc-Si materials, point defects are assumed to couple with the diffusing species. Vacancy related mechanisms will be discussed and experiments will be designed to investigate this possibility. Tasks of this research work are:

- Develop a "complete" diffusion model of hydrogen in silicon.
- Seek a numerical solution of the diffusion model.
- Model trap-limited hydrogen diffusion.
- Model and discuss the role of charge state conversion and field in hydrogen diffusion.
- Experiments designed to confirm the existence of mobile traps in samples processed using ion beams.
- Understand various hydrogenation techniques currently in use.

The dissertation will be organized in the following manner: the second chapter will present a review of hydrogen in silicon. The third chapter will focus on modeling of hydrogen diffusion in crystalline silicon. The discussion of various hydrogenation techniques by means of simulation and experimental observation will be presented in the fourth chapter. Conclusions and future direction will be given in the last chapter.

CHAPTER 2

HYDROGEN IN SILICON: A REVIEW

2.1 Introduction to Hydrogen in Semiconductors

Hydrogen atom is light, mobile and very active. In semiconductors, it diffuses fast and readily attaches to broken chemical bonds (or so-called "dangling bonds") at crystalline defect sites. Hydrogen also reacts with impurities in the semiconductors, such as shallow level dopants and metallic impurities. The complexes hydrogen forms are usually electrically neutral. Thus, deep levels associated with the material imperfection are effectively removed from the bandgap and minority carrier lifetime of the material can be greatly increased.

Research has shown that hydrogen plays an important role in improving Si devices whose performance is limited by the minority carrier lifetime of the material. For example, when an oxide-passivated diode was hydrogenated, a ~10-fold drop in leakage current was observed [45]. Post metallization anneal (PMA) in hydrogen forming gas, an integral step in MOS device fabrication, is known to passivate the dangling bonds at the Si-SiO_2 interfaces. Hydrogen can passivate the grain boundaries of polycrystalline silicon (poly-Si) and was adopted in poly-Si based TFT applications [46], [47]. Hydrogen has been used extensively in the PV industry. For example, H-dilution of Si-bearing gas is required to deposit electronically high quality amorphous silicon (a-Si) [48] for high-efficiency solar cells. Poly-Si based solar cells typically see a higher efficiency after the hydrogenation [49], [50]. For many PV vendors, the use of hydrogenation has become mandatory.

The hydrogen diffusion mechanisms are quite complex. The surface and bulk quality can affect the diffusion process. There are questions as to how various interactions of hydrogen affect the diffusion profiles, such as trapping at impurity sites and carrier exchange with the Fermi level. This chapter will first review various hydrogenation techniques. Then, the states of isolated hydrogen and its interaction with lattice and impurities will be reviewed. Finally, relevant information from literature will be presented concerning charge state equilibrium and kinetics of diffusion and complex formation. Some previous studies of this research group will also be reviewed.

2.2 Hydrogenation Techniques

2.2.1 Introduction

Many methods can be used to introduce hydrogen into a semiconductor specimen, however not all are beneficial. The types of techniques to be discussed in this section are ion implantation, electrochemical, and forming gas anneal (FGA).

2.2.2 Ion Beam Hydrogenation

Hydrogen can be introduced by ion implantation technique. The ion source in an implantation apparatus is a region of gas ionization that is physically separate from the target. High voltage extraction grids are used to extract the ionized species from a plasma source and direct them towards a target substrate. In the past 15 years, the ion source has seen a significant development. Many flexible and efficient designs are available now, among which there are two principal configurations for hydrogen implantation application, the Kaufman [51] and the electron cyclotron resonance (ECR)

[52] designs. In the former, a magnetic field is utilized to increase the electron path lengths and to enhance ionization efficiency. In the latter, a microwave source is added to induce a cyclotron resonance condition in the microwave cavity.

Studies [53] showed that hydrogen beams produced by Kaufman source are typically composed of mixtures of H^+ and H_2^+ ions and roughly equal mixture of energetic neutrals. The energy spectrum of such source is sharply peaked at low acceleration voltages (150-500 eV) but spreads out considerably at voltages above 1000-V. Many studies have been done with Kaufman ion source on PV silicon materials grown by web [54], ribbon [33], and EFG [55] techniques. It was shown that only a few minutes exposure to a Kaufman ion source beam results in passivation of a substantial fraction of the active recombination sites to depths of 10-50 μm. It seems both diffusion in the bulk and the diffusion along grain boundaries are important.

ECR ion source is a good alternative to Kaufman-type ion source. A plasma is sustained in a coaxial waveguide by evanescent wave coupling of microwave energy at ~ 2.45-GHz. The plasma is further enhanced by the ECR action of a quadruple magnetic field producing an extensive surface in the plasma on which electron cyclotron resonance at the given microwave frequency takes place. The major advantage of an ECR source is being filamentless and permitting use with reactive gases. This technique does not need the addition of foreign element and a large amount of atomic hydrogen can be produced. The ion energy can be precisely controlled and surface damage due to ion bombardment is negligible.

Although ion beam hydrogenation has been used extensively in research, it has several drawbacks to be deployed in a production line. Firstly, the cost of system using

either ion source can be substantial, typically, $70-120K. Secondly, the exposure to Kaufman ion beam can cause surface damage and erosion in the typical energy range of 150-1200 eV [56]. The irradiation caused by the high acceleration voltage can induce carrier traps and be detrimental to the cell being processed [57].

2.2.3 Plasma Methods

Hydrogen can also be introduced from hydrogen plasma ambient. A plasma can be supplied by either dc or ac electric field. Under suitable conditions, once the energy transferred from an accelerated electron to a gas atom is greater than the ionization potential, a second free electron will be generated. When sufficient number of electrons is available to maintain the discharge, the discharge is said to be self-sustained. If the reactant is H_2, the discharge will produce a large amount of atomic hydrogen. In typical plasma systems, rf diode configurations with frequency in the range of 100-KHz to greater than 100-MHz are primarily used. Figure 2.1 shows a plasma hydrogenation apparatus using the glow-discharge method.

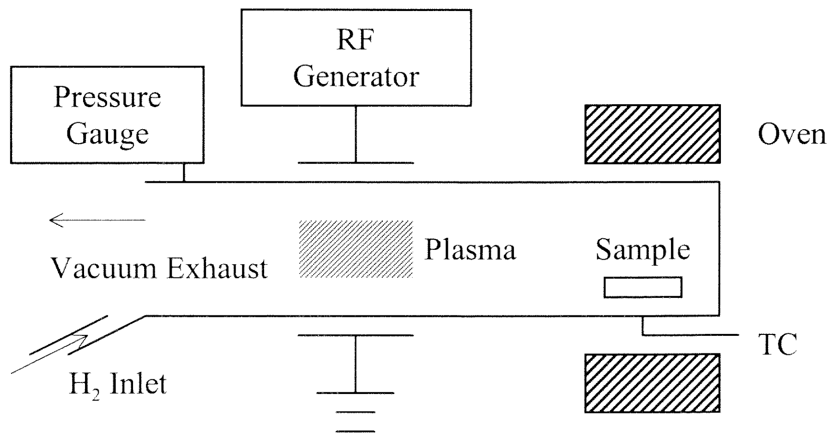

Figure 2.1 Schematic of a typical plasma hydrogenation system.

Currently, many solar companies use plasma reactors to deposit AR-coating layer such as Si_3N_4 onto a solar cell. Typically, the deposition uses a mixture of silane (SiH_4) and ammonia (NH_3) / nitrogen (N_2) in a plasma at 200 ~ 400ºC. Infrared spectroscopy found an appreciable amount of hydrogen in the form of Si-H and N-H in PECVD silicon nitride films. The total amount of hydrogen can reach up to 18-22 at% in film deposited from SiH_4-NH_3 near 300ºC [58], [59]. This indicates that a large amount of atomic hydrogen radicals is present in the plasma discharge. However, it is noted that a further rapid thermal process (RTP) treatment is required to have a deep diffusion.

The problem with direct plasma method is surface damage caused by ion bombardment. It was observed that the potential of the plasma in an rf glow discharge is positive relative to that of the grounded electrode and to that of the powered electrode. If a wafer is placed on grounded electrode of such a system, the negative voltage bias will accelerate the positively charged species such as H^+ towards the wafer surface and cause energetic ion bombardment. A modified version of plasma hydrogenation is to direct the desired component (free radicals) out of the plasma region. In some cases, the downstream products flow through a separate chamber where the specimen is located. The specimen is thus physically and optically isolated from the plasma source. This technique is sometimes called "remote plasma". The ion bombardment and UV radiation damage [60] can be greatly reduced.

Remote plasma hydrogenation has been the mainstream of hydrogen diffusion research recently. In practice, oxygen is added to hydrogen plasma, which has long been known to increase the dissociation yield of monatomic hydrogen, presumably due to the

suppression of hydrogen recombination on the walls of the chamber [61]. However, hydrogen plasma in contact with quartz tube wall degrades the latter with the release of oxygen. This effect can be controlled by changing the quartz tube frequently, but it affects its deployment in commercial lines.

2.2.4 Electrochemical Techniques

Electrochemical techniques appear to be attractive alternatives to the gas phase methods. They are able to maintain higher hydrogen densities at the solution/wafer interface. Since there is no kinetic energy associated with the ionized hydrogen species in electrochemical methods, damage-free surfaces can be produced.

Exposure to acidic environments, such as hydrofluoric acid (HF) or its mixture with nitric acid (HNO_3), can be used to introduce atomic hydrogen. For example, at 300K, the HF mixture is such an active agent that it produced almost complete boron-hydrogen pairing at ~10^{15} cm^{-3} level as deep as 3 micron into the silicon bulk in just 30 seconds [62]. A good surface passivation was observed on silicon with HF [63]. Even immersion in boiling wafer was found to offer hydrogen penetration, though a long processing time is needed to see any eminent passivation, typically several hours [64].

Temperature is a limiting factor of this method. Although it is possible to maintain a high concentration of hydrogen at the surface, the intrinsic diffusivity corresponding to the typical processing temperatures (~300K) is very low. The solution may be heated but the temperature cannot exceed the boiling limit.

2.2.5 Forming Gas Anneal

Forming gas anneal (FGA) was known to passivate the dangling bonds at Si-SiO_2 interfaces [67] and has been successfully applied in standard MOS process as post metal annealing (PMA). Interface traps are defects at Si-SiO_2 interface and can capture (emit) carriers from the conduction (valence) band. An increase of interface traps causes the shift of threshold voltage, V_T, and the characteristics of drain current, I_D, vs. gate voltage, V_G. PMA was found to remove both characteristic interface states and interfacial paramagnetic defect centers in the MOS structure [65], [66]. A typical 10-min, 450°C anneal in 10% hydrogen-nitrogen forming gas reduces the midgap D_{it} to an acceptable 10^{10} $cm^{-2}eV^{-1}$ level. Catalytic reduction of H_2 and the release of atomic H were believed to play a key role [67]. One possible place for such reaction to occur is in the vicinity of metal, such as Pd [68]; however, sometimes passivation can be seen when the metal gate is absent [69]. The dissociation of H_2 at silicon dangling bonds in the dielectric SiO_2 and at the Si/SiO_2 interface has been proposed [70], [71].

Detailed FGA study was performed on passivation of crystalline defects in poly-silicon used for solar cells [42]. Laser beam induced current (LBIC) indicated that interfacial recombination velocities of grain boundaries are reduced to ~50%. FGA treatment of a solar cell leads to an additional ~ 3% efficiency increase [41]. However, passivation was found to be less marked than that of plasma technique and is limited to 10 –15 μm below the surface. Recent studies have shown that FGA in hydrogen ambient produces an enhanced passivation effect when combined with aluminum (Al) diffusion [39]. Some evidence showed that the diffusion depth of FGA is also related to the extent of surface damage [72].

Table 2.1 Values of the energy (per H atom) of H configuration in Si [137].

Configuration	E (eV)
H^0 in free space	0
H at BC	-1.05
H_2 in Si	-1.92
H_2	-2.31

There are some theories available to support the postulation that surface damage dissociates H_2. *Ab initio* tight-binding MD simulations showed that the potential energy between V infinitely far from H_2 and {V, H, H} is 4.0 eV [133]. Before molecular H_2 is dissociated, it has to overcome a 0.8-eV surface barrier, according to energy levels shown in Table 2.1. By splitting H_2, there is actually an energy gain of 3.2 eV. As a result, H_2 molecule may be spontaneously dissociated with the presence of vacancies near the damaged surface.

2.3 Ion Beam Depth Profiling Techniques

Hydrogen (H) or its isotope deuterium (D) can be profiled by using various ion beam techniques. Most of these allow an absolute measurement of the H (D) concentration. An overview can be found in [73] and [74]. Table 2.2 summarizes four popular ion beam profiling methods, their detection limits and depth resolutions. For a non-layered specimen, secondary ion mass spectrometry (SIMS) usually generates satisfactory results with a deeper resolution in comparison with other methods. In many cases, D is used to improve the detection limit of SIMS.

Table 2.2 Ion beam depth profiling techniques, their detection limits and depth resolutions.

Ion Beam Technique	Detection Limit	Depth Resolution
Secondary ion mass spectrometry (SIMS)	10^{14} cm^{-3} for D 10^{18} cm^{-3} for H	Deep as sputtering goes
Nuclear reaction that emits charged particles (ECP)	10^{12} cm^{-3} for D	~ 1 μm
Nuclear reaction that emits Gamma rays (EGR)	20 appm	~ 600 A
Nuclear reaction leads to elastic recoil detection (ERD)	10^{15} cm^{-3} for H	500 – 800 A

2.4 Isolated Hydrogen in Silicon

The interaction of hydrogen with silicon lattice leads to the understanding of the location of hydrogen and the migration pathway of hydrogen in silicon. In the early days, H_2 was routinely used as the ambient for crystal growth and anneals, because it was believed that H_2 is inert like a noble gas. It appears now that hydrogen can interact and sometimes passivate a semiconductor, but the studies of hydrogen in silicon did not draw much attention until 1983, when Sah et al. [75] reported hydrogen passivation of boron shallow acceptor. In fact, the states and migration of hydrogen in silicon is still an intricate topic and many questions remain unanswered. It would be helpful to give a brief review of the current understanding of isolated hydrogen in silicon, because the migrating hydrogen species is believed to be mostly in atomic form.

The structure of H in Si lattice has been investigated experimentally and theoretically in detail. The experimental data is very difficult to obtain because hydrogen's intrinsic solubility in silicon is very low. Some early experiments used channeling and IR spectroscopy to analyze H- or D-implanted high-resistivity Si samples. Measurements indicated that hydrogen may reside in stable state on various interstitial sites of high symmetry in a silicon lattice. Figure 2.2 shows a portion of silicon lattice, which shows interstitial sites tetrahedral (T), hexagonal (H), C, and M [76]. The C-site is at the center of the rhombus formed by three adjacent substitutional sites and the nearest T-site. M-site is the midpoint between two adjacent C-sites. An important site is BC-site, which is the bond center of two adjacent silicon atoms.

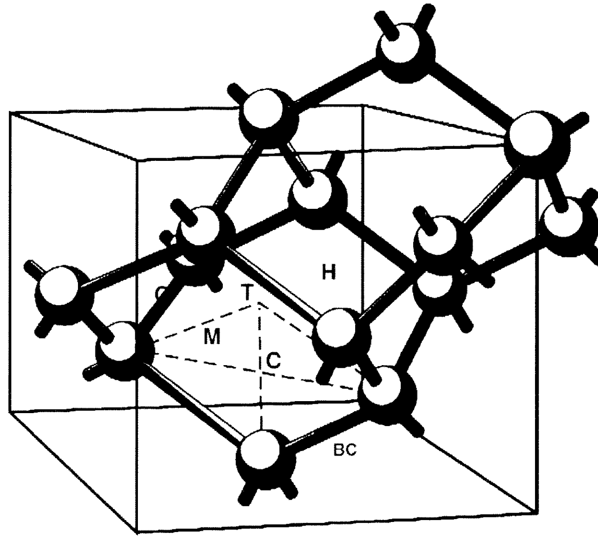

Figure 2.2 A sketch of the Si lattice showing important interstitial sites, after Ref. [76].

Initial experimental investigations yielded ambiguous results. For example, early channeling measurement [77] showed that in hydrogen-implanted samples, the hydrogen site was located at an antibonding position, 1.6 Å from a silicon lattice site. This conclusion influenced other workers over a period of ten years. Later it was found that the influence of damage and annealing caused by the analyzing beam was not taken into account. In the theory part, early calculations neglected the relaxation of the host crystal network around the hydrogen impurity, which caused the neglect of BC-site. An overview of the literature and problems was included in a review by Patterson [78]. Another class of calculation utilized cluster model, i.e., a method taken from quantum chemistry. This involves partial retention of diatomic differential overlap (PRDDO) and *ab initio* minimal-basis-set Hartree-Fock (HF) calculation by Estreicher [79], and MINDO/3 (modified intermediate neglect of differential overlap) method by Deak and co-workers [80]. The application of cluster model to solid-state problem is usually not

justified and very few cluster calculations test for convergence as a function of cluster size. The results obtained by early analyses led to erroneous conclusions and did not agree with many experimental observations. Recent theoretical results from a variety of calculations based on MINDO, *ab initio* HF molecular dynamic (MD) calculations, considering relaxation of the host crystal, seem to yield better solutions that match the experimental results. A successful theoretical calculation usually contains information about the global minimum energy sites of hydrogen atom of different charge states and the migration path of the species. Some important results are summarized below.

Isolated interstitial H can exist in three charge states—H^+, H^0, and H^-. The positive ion is at a relaxed BC-site (associated with high charge density), H_{BC}^+, which is a preferred state of hydrogen in p-type Si. The donor level was found about 0.2 eV below the conduction band edge [81], [82]. The migration of H_{BC}^+, occurring by jumping from one BC site to the adjacent one has an activation energy of 0.48 eV shown by high-temperature *ab initio* MD simulation [83] and low-temperature reorientation kinetics after stress-alignment [84].

Neutral hydrogen is metastable. Its lowest-energy state has trigonal symmetry at a relaxed BC site, H_{BC}^0, and at the T site as H_T^0. The energy difference between the two states is about a few tenths of an eV. The low charge density of neutral H at T site suggests that H_T^0 is not a stable state [85]; however, once H_T^0 is formed, it diffuses extremely fast [86] by taking a migration path of T→H→T. The activation energy of H_{BC}^0 is the same as that of H_{BC}^+. Most of this charge state in the bond region is related to H-induced levels buried in the valence band [85].

Negative ion of hydrogen is a dominant state in n-type Si, which is stable at the T site, H_T^-. H^- has a larger ion size than H^+ and its diffusion activation energy is at least 0.8 eV. The location of the acceptor level associated with this state is still under debate [82], [87], [88]. H is probably a "negative-U" impurity in Si, meaning that the donor level is above the acceptor level. The two levels may be only 0.1 or 0.2 eV apart and both of them may appear in the upper half of the bandgap. Above room temperature, different charge states may coexist. Hydrogen behaves as an amphoteric impurity: its preferred charge states, H^+ in p-type and H^- in n-type, lead to passivation of shallow-level dopants at low temperatures.

Hydrogen can form two kinds of dimers in the silicon lattice: an interstitial H_2 as molecules and an H_2^* complex. H_2^* was believed to consist of two Si-H bonds replacing a single Si-Si bond: one H is near the BC site and the other is in an antibonding position, with the two Hs on the same trigonal axis. This complex anneals out at about 200°C. Molecular H is generally seen in Si material grown in an H-containing ambient, exposed to H_2 gas at high temperatures or to H plasma.

The structure of H in the Si lattice is important to understand the microscopic diffusion in silicon samples of different resistivities. For example, because the preferred charge state of H_{BC}^+ in p-type silicon has a lower migration activation energy (0.48 eV) than H_T^- (> 0.8 eV) in n-type silicon, a higher diffusivity of hydrogen in p-type Si than in n-type Si can be expected.

2.5 Hydrogen Passivation of Crystalline Defects in Silicon

Hydrogen can attach itself to the dangling bonds at crystalline defects in silicon. The stronger bond strength of Si-H compared to that of Si-Si bond results in the complete passivation of the defect. It can also interact with weakly reconstructed bonds that are found at vacancies (Vs) or clusters of Vs. H rarely forms perfect Si-H bonds within the crystal because the Si bonds at the V and at clusters of Vs undergo some degree of reconstruction. Theoretical studies [89] showed that the most stable V aggregates have no deep levels in the gap, except the smallest one, the ring-hexavacancy complex (V_6), has a few empty shallow levels very near the conduction band.

Self-interstitial (I) and I-aggregates also trap H, but their thermal stability is low (maybe 200°C or less). Only one {I,H,H} complex has been identified by FTIR and *ab initio* theory [90]. Its vibrational modes are at 1987 and 1989 cm^{-1}, below those of {V_n,H} complexes. The binding energies are small, ranging from 2.6 eV for {I, H, H} down to 1.5 eV for {I, H}, and just a few tenths of an eV for {I, H, H, H}. The capability of H is to passivate point defects and point defect clusters effectively and remove the energy levels introduced by them from the bandgap and thus "passivate" the material.

Hydrogen can also passivate extended crystalline defects such as dislocations, stacking faults and grain boundaries. Dislocations are localized interruptions in a crystal's periodic network. Grain boundaries are the interfaces between adjacent crystallites. Such defects can be introduced as a result of large thermal gradient and stress during the growth of a crystal. There are a large number of dangling bonds at those crystalline defect sites, which introduce a band of energy states in the bandgap and virtually pin the Fermi level near midgap. The hydrogenation of grain boundaries of

polycrystalline silicon (poly-Si) [91], [36], has been applied on mc-Si solar cell [49], [50], and TFT devices [46], [47], to reduce the defect levels and to improve the lateral carrier transport.

Hydrogen diffuses rapidly and segregates at kink sites of dislocation networks or grain boundaries. However, sometimes the impurity precipitates can segregate at those defects too. It is not clear if H can passivate decorated extended defects.

2.6 Hydrogen Interactions with Shallow Level Dopants

The earliest evidence of acceptor neutralization was found in the work of Sah [75], which inspired succeeding research on passivation of shallow acceptors. The complex formed by hydrogenation of p-type Si is electrically neutral and effectively increases the resistivity of a sample. This complex has a threefold coordinated B with H tying up the fourth Si bond in a near-BC position. Figure 2.3 illustrates formation of such a complex. Here, B is a boron atom. From an Arrhenius analysis [92] of change in subsurface resistivity, the bond breaking that reactivates the acceptor has activation energy of 0.76 eV. The measurement by using multiple internal reflection infrared absorption [93] revealed a sharp absorption band at 1875 cm^{-1}, which is consistent with an isotopic shift to 1360 cm^{-1} detected by using deuterium [94]. Boron-hydrogen complex (BH) dissociates below temperature of 200ºC, with a dissociation rate satisfying the Arrhenius relation $\nu = \nu_0 \exp(-E_A / kT)$, where pre-exponential factor ν_0 = 2.8 × 10^{14} s^{-1} and activation E_A = (1.28 ± 0.03) eV [95]. The dissociation energies of other acceptors were reported in the same reference as (1.44 ± 0.02) eV, (1.40 ± 0.03) eV, (1.42 ± 0.05) eV for AlH, GaH, and InH complexes, respectively.

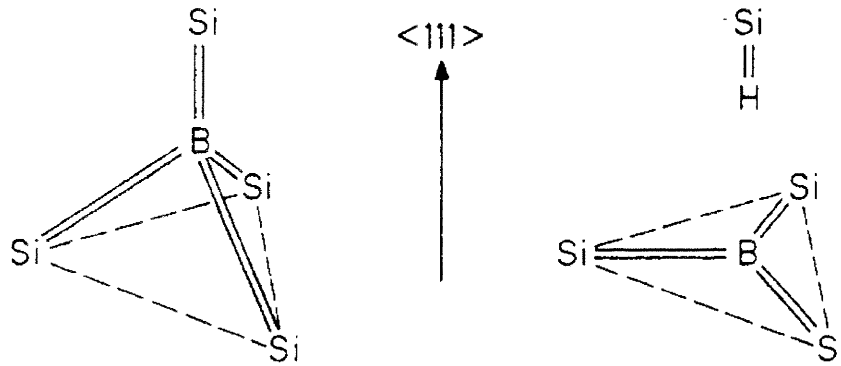

Figure 2.3 Illustration of H bonding with an acceptor in Si.

The effect of hydrogen on the electric properties of n-type silicon is subtler than that of p-type silicon. The less efficient formation is because hydrogen primarily exists in p-type silicon as H_T^-, which has a low mobility, and as H_{BC}^0, which has a small capture cross section by P^+ ion. The first report that hydrogen can neutralize shallow-donor impurities in silicon was experimentally based on Hall-effect data in 1986 by Johnson [96]. Experimental evidence was obtained later from vibrational spectroscopy [97], showing that absorption bands appeared at 1555, 1561, and 1562 cm^{-1} for implanted P, As, and Sb, respectively. An additional band observed at ~ 810 cm^{-1} for each dopant species was assigned to the wagging mode of the donor-hydrogen complex. Uniaxial stress studies [98] of those absorption bands established the trigonal symmetry of the complex and confirmed the identification of the stretching and wagging modes. Electronic structure calculations [99] yielded a model in Figure 2.4 that the hydrogen atom resides near the Si antibonding T_d site with the Si-P bond broken and strong Si-H bond formed in its place. This arrangement accounts for the electrical neutralization, the weak dependence of the vibrational frequencies on donor species, and the trigonal symmetry of the complex. Biased vacuum anneal experiment [100] of a hydrogenated

Schottky-barrier diode on n-type silicon established the existence of H^- species and dissociation reaction for the PH complex is PH → P^+ +H^-. The dissociation rate of PH complex satisfies the Arrhenius relation $\nu = \nu_0 \exp(-E_A / kT)$, where pre-exponential factor $\nu_0 = 8.4 \times 10^{13}$ s^{-1} and activation energy $E_A = (1.18 \pm 0.01)$ eV. Low temperature infrared studies [97] reported the same dissociation energy of 1.43 eV for AsH and SbH complexes. The PH pair breaks up below 100ºC in the dark and at room temperature under illumination.

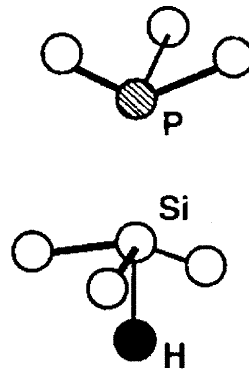

Figure 2.4 The broken-bond T_d site model of donor-hydrogen complex in silicon [99].

The higher IR-active stretch mode indicates B-H bond is thermally more stable than P-H bond. Hydrogen neutralization of shallow-level dopants has important technological implications, because hydrogen can modify the resistivity of the substrate and is easily introduced unintentionally, such as in dry etching system that uses H-containing gases. For example, hydrogen was found to migrate though the oxide and pile-up at the SiO_2/Si interface of a metal-oxide-semiconductor (MOS) structure and decreases capacitance [101] on B-doped silicon due to the resistivity change.

2.7 Hydrogen Interactions with Other Impurities in Silicon

Atomic H was found to interact with metallic impurities such as Fe [102], Cr [103], Ni [104], Cu, and Au [105] to reduce their carrier recombination in Si. Some transition metal (TM)-H complexes with Ti, Co, Ag, Pt, and Pd have been detected primarily by DLTS analyses [106], [107], [108]. Various equilibrium structures for TM-H complexes have been calculated [109]. Interestingly, the DLTS data do not verify that all the complexes are electrically inactive. For some TM, it appears that H only shifts the position of the energy levels within the gap. So far, there is no experimental or theoretical information on the passivation of TM precipitates. These are the important issues for fabrication of high-efficiency solar cells on low-cost Si substrates. If hydrogen can hardly passivate TM precipitates, they should be dissolved before gettering or passivation process.

Interactions of H with C and O are significant because these impurities are present in high concentrations in most Si devices. Recently, there has been a flurry of results on interactions between H and interstitial oxygen (O_i). It has been reported that the growth of O-related thermal donors in CZ-Si is greatly enhanced if the material is grown in an H_2 ambient. This mechanism appears to be caused by the tendency of O_i to attract isolated H and H_2. On the other hand, in the temperature range of 300° – 450°C, H acts as a catalyst to enhance the diffusion of O. In oxygen-rich Si samples, three lines associated with H_2 are seen by FTIR [110], two of which are associated with H_2 trapped near interstitial oxygen (O_i). The binding energy of H_2 to O_i is 0.26 ± 0.02eV, and the activation energy for diffusion of H_2 is 0.78 ± 0.05 eV. Isolated H_2 has been seen [111] following anneals

of Si up to 350°C. This is of particular importance because H behaves differently in CZ than in FZ silicon.

Two models have emerged to explain the enhancement of O diffusivity by H. In the first, H lowers the activation energy for O diffusion by tying up a Si dangling bond at the transition point. In the second, obtained from MD simulations, a covalent H-O pair forms, which transforms the stiff Si-O-Si bridged bond into a H-O-Si bond, with the {H,O} pair now able to rotate around the fixed Si atom, allowing it to visit the adjacent BC site. This problem is not completely understood.

2.8 Hydrogen Diffusion in Silicon

2.8.1 Diffusivity and Solubility of Hydrogen in Silicon

The early study of diffusivity and solubility of hydrogen in crystalline Si was made by Van Wieringen and Warmholtz (VWW) [112]. These authors made a hollow tube of single-crystalline silicon, with one end closed. The tube was surrounded with H_2 gas at one atmospheric pressure from 1090° to 1200°C and the rate of permeation of the hydrogen into the evacuated bore was measured with a mass spectrometer. The diffusivity and solubility derived fell nicely on the Arrhenius lines:

$$D = 9.67\times 10^{-3}\exp\left(-\frac{0.48eV}{kT}\right)\ (\text{cm}^2/\text{sec}), \tag{2.1}$$

and,

$$s = 4.96\times 10^{21}\exp\left(-\frac{1.86eV}{kT}\right)\ (\text{atom/cm}^3)\text{ at 1-atm.} \tag{2.2}$$

The dissolved hydrogen was believed to exist in monatomic forms, presumably H^+ or H^0 due to the fact that the permeation coefficient varies as $p^{0.50}$ at 1050°C over the range of

H_2 pressure from 83 to 606 mmHg. The diffusion activation energy, 0.48 eV, in the Eq. (2.1), also agrees with the MD calculation [83] of H_{BC}^+ and H_{BC}^0. Compared to atomic hydrogen, the molecular species, H_2, is believed to have a higher diffusion barrier, i.e., 0.78 eV. VWW Arrhenius line of solubility indicates a very low value at low temperatures, e.g., 5.52×10^7 cm^{-3} at 400 °C, and 3.15×10^{-1} cm^{-3} at 150 °C.

Low temperature diffusion studies have been conducted using various methods such as radioactivity decay with tritium [113], C-V measurement [114], and current density measurement during electrolysis hydrogenation [115]. Figure 2.5 shows hydrogen diffusivity data from various sources. The solid curve represents the VWW extrapolation. The salient feature is that there is a large spread of diffusivity data and all of them are several orders of magnitude below the VWW extrapolation. It seems that the high temperature Arrhenius line (the solid curve) somehow serves as an "upper limit". The "intrinsic" diffusivity at room temperature is 8.3×10^{-11} cm^2/s.

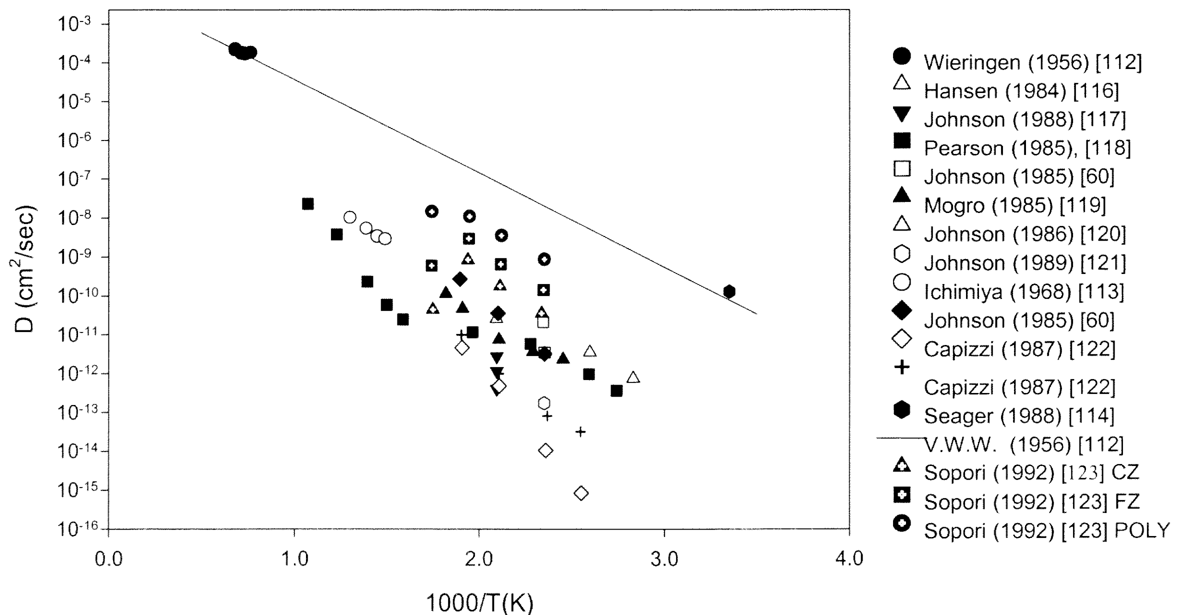

Figure 2.5 Diffusivity of H reported by various researchers.

It appears that the fitted low temperature diffusivities in Figure 2.5 are not "intrinsic" but "effective" diffusivities. The large variation in D_H indicates that more than one mechanism is involved in the diffusion under different experimental conditions. The diffusion characteristics can be strongly influenced by the material quality and defect density. As reviewed in the previous sections, hydrogen diffusion is indeed accompanied by the interaction with the lattice imperfection. H can form complexes with impurities and defects that are stable at low temperatures. This mechanism can cause trapping of H and reduce the "effective" diffusivity. In Chapter 3, low temperature diffusion profiles will be explained by using simultaneous trapping and detrapping mechanism.

2.8.2 Theoretical Framework

2.8.2.1 Equilibria Charge States and Carriers. With the presence of impurities and defects in the semiconductor lattice, hydrogen can react with them and form a variety of complexes, which in turn can dissociate and release their atomic constituents. It has been a consensus that atomic hydrogen exists and migrates in the silicon lattice in different charge states, i.e., H^+, H^0, and H^-. Those charged species can occupy different interstitial sites and migrate along different paths. In a doped semiconductor, different charge states can interconvert by emission or absorption of electrons or holes. In effect, carrier transport is a "fast" process compared to the balancing process of local charge states of hydrogen via carrier exchange. The reason is that the diffusivity of atomic hydrogen is much smaller (~10^{-10} cm2/s) than that of the carriers (D_e = 35 cm^2/s, D_h = 13 cm^2/s) at room temperature (300K). At high temperatures, this is still true, because diffusivity of

hydrogen is merely ~10^{-4} cm^2/s, whereas D_e and D_h are much higher. It is imaginable that before a slightest spatial change of total dopant distribution is felt due to hydrogen migration, the carriers have readily been redistributed. Even if hydrogen is being trapped in the meantime by the dopant impurities or defects, the local reduction rate of available atomic hydrogen is still limited by its diffusivity. Carriers are replenished fast enough to keep Poisson equation satisfied. As a result, a spatially uniform Fermi level (or quasi-Fermi level in biased cases) can be always assumed.

In different charge states, hydrogen can be either fermion or boson, which should follow the corresponding statistics:

$$\overline{n}_k = \frac{\lambda e^{-\beta E_k}}{1 \pm \lambda e^{-\beta E_k}} = \frac{1}{e^{\beta(E_k-\mu)} \pm 1}, \tag{2.3}$$

where "+" represents Fermi-Dirac (F.D.) statistics and "-" represents Bose-Einstein (B.E.) statistics. $\beta \equiv 1/kT$, where k is Boltzmann constant, 1.38×10^{-23} J/K. $\lambda \equiv e^{\beta\mu}$, where μ is the chemical potential.

For a system with low density of available particles, most energy states remain unfilled. In this case, $\lambda \to 0$, and F.D. or B.E. statistics will turn close to Boltzmann distribution,

$$\overline{n}_k = \lambda e^{-\beta E_k} = e^{\beta(\mu-E_k)}. \tag{2.4}$$

The total number of particles is thus

$$\overline{N} = \sum_k n_k = \sum_k e^{\beta(\mu-E_k)} = Z(T) e^{\beta(\mu-E_0)}, \tag{2.5}$$

where $Z(T)$, the partition function is defined by

$$Z(T) \equiv \sum_k e^{-\beta(E_k-E_0)}. \tag{2.6}$$

Figure 2.6 illustrates a transition diagram of capture / emission of electron by hydrogen atoms. It is perceivable that by contributing an electron from donor level to the Fermi level, a neutral hydrogen species, H^0, loses energy of $(E_d - E_f)$. By capturing an electron from the Fermi level to the acceptor level, H^0 loses energy of $(E_f - E_a)$, or gained energy of $(E_a - E_f)$. The Fermi level position with respective to both defect levels can change the ratio of concentrations of hydrogen species of different charge states.

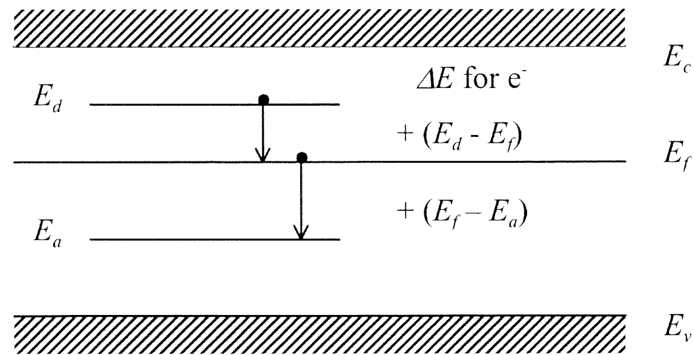

Figure 2.6 Transition diagram of different charge states of an impurity in semiconductor, given the co-existence of both donor and acceptor levels.

If hydrogen exists in either of the three charge states, i (i = +, 0, or -), which have v_i possible positions in each unit cell of volume Ω_0, it is possible to write down the following number of hydrogen in different charge states as

$$\overline{N}_0 = Z_0 e^{\beta(\mu - E_0)}, \tag{2.7}$$

$$\overline{N}_+ = Z_+ e^{\beta(\mu-(E_0-(E_d-E_f)))} = \frac{Z_+}{Z_0}\overline{N}_0 e^{\beta(E_d-E_f)}, \tag{2.8}$$

$$\overline{N}_- = Z_- e^{\beta(\mu-(E_0+(E_a-E_f)))} = \frac{Z_-}{Z_0}\overline{N}_0 e^{\beta(E_f-E_a)}, \tag{2.9}$$

where E_f is the Fermi level, E_d the donor level, and E_a the acceptor level. We use the energy of neutral hydrogen as the reference for all charged states. The μ in all three expressions corresponds to the electrochemical potential of neutral hydrogen.

Given $[H_i] = \nu_i \dfrac{\overline{N}_i}{\Omega_0}$,

$$\frac{[H^+]}{[H^0]} = \frac{\nu_+ Z_+}{\nu_0 Z_0} e^{\beta(E_d - E_f)}, \tag{2.10}$$

$$\frac{[H^-]}{[H^0]} = \frac{\nu_- Z_-}{\nu_0 Z_0} e^{\beta(E_f - E_a)}. \tag{2.11}$$

In the first order approximation, the number of possible positions in a unit cell is assumed to be the same for all charge states, i.e., $\nu_+ = \nu_0 = \nu_-$, and the partition functions differ little from its $T = 0$ value, i.e., $Z_+ = Z_0 = Z_-$. The following simplified equations are obtained:

$$\frac{[H^+]}{[H^0]} = e^{\beta(E_d - E_f)}, \tag{2.12}$$

$$\frac{[H^-]}{[H^0]} = e^{\beta(E_F - E_A)}. \tag{2.13}$$

Those two equations show that the population of hydrogen in different charge states depends on the Fermi level position with respective to the donor or acceptor level. Atomic hydrogen was assumed a "negative U center" after Ref. [124].

For a particular distribution of total hydrogen and shallow donor and acceptor impurities, Eqs. (2.12) and (2.13) need to be solved together with the Poisson equation,

$$\nabla^2 \phi = -\frac{\rho(\bar{x})}{\varepsilon_s} = -\frac{e}{\varepsilon_s}\left[(p - n) + \left([H^+] - [H^-]\right) + \left(n_D^+ - p_A^-\right)\right], \tag{2.14}$$

where n_D^+ is ionized donor concentration and p_A^- is ionized acceptor concentration. At room temperature, shallow donor and acceptor dopants are fully ionized, so $n_D^+ \approx N_D$ and $p_A^- \approx N_A$. The electrical potential, ϕ, as a function of position can be defined as the mid-gap energy level, E_m, of the corresponding position divided by electron charge (- e). At room temperature or above, Fermi level of intrinsic silicon is almost at mid-energy level, i.e., $E_m \approx E_i$. In thermal equilibrium, semiconductor has a uniform Fermi level. As a result, the electrical potential, ϕ, can be redefined as

$$\phi \equiv \frac{1}{(-e)}\left(E_i - E_f\right) = \frac{1}{e}\left(E_f - E_i\right). \tag{2.15}$$

The electron and hole densities are

$$n = n_i e^{\beta\left(E_f - E_i\right)} = n_i e^{\frac{\phi}{V_T}}, \tag{2.16}$$

$$p = n_i e^{-\beta\left(E_f - E_i\right)} = n_i e^{-\frac{\phi}{V_T}}, \tag{2.17}$$

where the thermal voltage $V_T \equiv \frac{kT}{e} = \frac{1}{e\beta}$. From Eqs. (2.12) through (2.17), together with the constraint that

$$[H^+] + [H^0] + [H^-] = [H], \tag{2.18}$$

electric potential, carrier distribution, and the density of individual charged hydrogen species can be solved.

2.8.2.2 Local Kinetics of Complex Formation. As atomic hydrogen diffuses through the semiconductor lattice, it varies its charge state by exchanging carriers with the Fermi level. At moderate temperatures, neutral complexes can be formed and the corresponding

energy levels are removed from the bandgap. Opposite to the capture of charged hydrogen species, the thermal dissociation process takes place simultaneously. At elevated temperatures, the dissociation can be dominant such that complex formation appears negligible.

In the case of a simple combination-dissociation process of ionized acceptor A^- with positively charged hydrogen H^+ forming a complex AH, the following reaction is taking place,

$$A^- + H^+ \overset{k_{AH}}{\underset{k'_{AH}}{\leftrightarrow}} AH \,. \tag{2.19}$$

Due to the Coulombic attraction, the formation of complex will occur when the random motion of diffusing H^+ put it within some capture radius R_c of A^-. According to the diffusion theory of reactions [125] and [126], the rate of rightward reaction in (2.19), per unit volume is set equal to the product of the density $[A^-]$ of A^- ions by the steady-state diffusive flux of H^+ across the surface of a capturing sphere of radius R_c, given a concentration $[H^+]$ at infinity. The expression is

$$\left(\frac{d[AH]}{dt}\right)_{capt} = 4\pi D_+ R_c [A^-][H^+] \tag{2.20}$$

where D^+ is the diffusivity of H^+.

A critical parameter in Eq. (2.20) is the capture radius, R_c. For a large capture radius, the formation rate of the complex is higher. For Coulombic capture, the capture cross section, $\sigma_c \equiv 4\pi R_c^2$, is calculated to vary at T^n, with n being as large as 2 or 4 [127], [128]. For a simple case that R_c is roughly the distance where the Coulombic energy drops to the thermal energy, i.e. $k_B T = \frac{1}{4\pi\varepsilon}\frac{e^2}{R_c}$, R_c can be written as

$$R_c = \frac{e^2}{4\pi\varepsilon}\frac{1}{k_B T}. \quad (2.21)$$

This corresponds to a capture radius of about 30 A at 150°C, 22 A at 300°C, or 12 A at 800°C. For problems that are not Coulombic, R_c can be expected smaller than an interatomic spacing of the traps and has a modest dependence of the temperature. In such cases, R_c changes more gradual than that of the diffusivity.

The leftward reaction in Eq. (2.19) corresponds to the simultaneous dissociation of the complexes. This reversal process can be described by a dissociation frequency, k_{AH}', which has a unit of (s^{-1}). The dissociation rate of AH complex can be expressed as

$$\left(\frac{d[AH]}{dt}\right)_{dis} = k'_{AH}[AH]. \quad (2.22)$$

The dissociation frequency, k_{AH}', is related to a dissociation attempt frequent, ν_{AH}, a pre-exponential constant, and the dissociation energy, E_{AH}, of the complex AH:

$$k'_{AH} = \nu_{AH} e^{-\frac{1}{kT}E_{AH}}. \quad (2.23)$$

Here, the dissociation energy, E_{AH}, relates to other two fundamental quantities, the binding energy, ΔE_{AH}, of the complex and the diffusion activation energy, E_{act}, of the H^- species and may be expressed as follows [100],

$$E_{AH} = \Delta E_{AH} + E_{act}. \quad (2.24)$$

This shows that in order for a complex to split into its constituents in free forms, it needs to overcome the binding energy and at least one diffusion-barrier.

The combination and dissociation reactions take place simultaneously. In the cases that the densities of the reacting species' are not high enough to invoke many-body effect, these are two independent events and can be superimposed. Usually, at low

temperatures, combination and complex formation is dominant, whereas at high temperatures, since dissociation rate is much faster than combination rate, complex formation seems negligible.

2.8.2.3 Kinetics of Diffusion. As discussed in section 2.6.2.1, diffusion of atomic hydrogen is a slow process compared to the charge equilibration process among species of different charge states. If all H^+, H^0, and H^- are present, Poisson's equation (2.14) should be satisfied at any time instant in order to obtain the correct statistical ratios among all the charged species (including hydrogen species, $[H^+]$, $[H^0]$, and $[H^-]$, dopants, and carriers).

In order to make the formulation illustrative, the formation of H_2 molecule, mobile traps, and mobile trap-hydrogen complexes are neglected. The only species considered as a first order approximation are mobile species: H^+, H^0, and H^-, and immobile species: shallow donor, D, shallow acceptor, A, trap, T, donor-hydrogen complex, DH, acceptor-hydrogen complex, AH, and trap-hydrogen complex, TH. The corresponding concentrations of immobile species are represented by [D], [A], [T], [DH], [AH], and [TH].

An important equation the system has to satisfy is the continuity equation:

$$\frac{\partial [H]^{tot}}{\partial t} + \nabla \cdot \vec{J}_{tot} = 0. \tag{2.25}$$

In all the following discussions, capital J's represent particle fluxes and small j's stand for electric currents. For example, J_{tot} will mean the total current of hydrogen species. Eq. (2.25) is true even with the presence of complex formation and dissociation.

With the presence of shallow acceptors, the Coulombic attraction will drag positively charged hydrogen, H^+, towards ionized and negatively charged acceptor core, A^-, to form a neutral complex, AH, as expressed in Eq. (2.19). The net increase rate of AH complexes can be described by combining the capture rate equation (2.20) and dissociation rate equation (2.22) as the following:

$$\frac{\partial[AH]}{\partial t} = k_{AH}[A^-][H^+] - k'_{AH}[AH] \tag{2.26}$$

where, $k_{AH} \equiv 4\pi D_+ R_c^A$, and k_{AH}' follows Eq. (2.23). Similar to the interaction between A^- and H^+, negatively charged hydrogen, H^- interacts with positively charged donor core, D^+, as the following:

$$D^+ + H^- \underset{k'_{DH}}{\overset{k_{DH}}{\leftrightarrow}} DH\,, \tag{2.27}$$

and the net increase rate of DH complexes is

$$\frac{\partial[DH]}{\partial t} = k_{DH}[D^+][H^-] - k'_{DH}[DH]\,, \tag{2.28}$$

where, $k_{DH} \equiv 4\pi D_- R_c^D$, and k_{DH}' follows the Eq. (2.23):

$$k'_{DH} = \nu_{DH} e^{-\frac{1}{kT}E_{DH}}\,. \tag{2.29}$$

Traps can be crystalline defects (point defects, dislocation, and grain boundaries) or other impurities. The interaction between traps and hydrogen may not necessarily follow the relation (2.21), but phenomenological values of capture cross section, capture rate, and dissociation rate can still be used. Supposing trap, T, interacts with total atomic hydrogen, H, regardless charge states, the following interaction occurs:

$$T + H \underset{k'_{TH}}{\overset{k_{TH}}{\leftrightarrow}} TH\,, \tag{2.30}$$

and the net increase rate of TH complexes is

$$\frac{\partial[TH]}{\partial t} = k_{TH}[T][H] - k_{TH}^{'}[TH], \tag{2.31}$$

where $k_{TH} \equiv 4\pi D_0 R_c^T$, given the neutral hydrogen is a dominant species. k_{TH}' follows the similar equations as Eqs. (2.23) and (2.29):

$$k_{TH}^{'} = \nu_{TH} e^{-\frac{1}{kT}E_{TH}}. \tag{2.32}$$

The total flux of hydrogen, J_{tot}, consists of the contributions from all three charged hydrogen species. The flux of each of them can be expressed in a way similar to the electric current of carriers, i.e.,

$$\vec{J}_{+} = -D_{+}\nabla[H^{+}] + \mu_{+}[H^{+}]\vec{E} = -D_{+}\left(\nabla[H^{+}] + \frac{k_B T}{e}[H^{+}]\nabla\phi\right) \tag{2.33}$$

$$\vec{J}_{0} = -D_{0}\nabla[H^{0}] \tag{2.34}$$

$$\vec{J}_{-} = -D_{-}\nabla[H^{-}] - \mu_{-}[H^{-}]\vec{E} = -D_{-}\left(\nabla[H^{-}] - \frac{k_B T}{e}[H^{-}]\nabla\phi\right) \tag{2.35}$$

With some simple transformations, the drift terms in (2.33) – (2.35) may be expressed in terms of concentrations of charged species. It turns out that

$$\vec{J}_{+} = -D_{+}\frac{[H^{+}]}{[H^{0}]}\nabla[H^{0}], \tag{2.36}$$

$$\vec{J}_{0} = -D_{0}\nabla[H^{0}], \tag{2.37}$$

$$\vec{J}_{-} = -D_{-}\frac{[H^{-}]}{[H^{0}]}\nabla[H^{0}]. \tag{2.38}$$

Thus, the total hydrogen flux is

$$\vec{J}_{tot} = D(\vec{x})\nabla[H^0], \tag{2.39}$$

where

$$D(\vec{x}) = \frac{[H^+]}{[H^0]}D_+ + D_0 + \frac{[H^-]}{[H^0]}D_- . \tag{2.40}$$

These two equations show that the hydrogen flux may be viewed as caused only by the neutral species, of which the equivalent diffusivity is magnified and is related to the ratio among the charged species.

To construct a set of equations to describe the diffusion problem, various complex formation and interconversion mechanisms need to be identified and the corresponding rate equations and fluxes can be substituted in to Eq. (2.25) to finish the formulation. In reality, there could be more diffusion mechanisms than what are known. Sometimes mobile traps and mobile trap-hydrogen complexes are involved. As an example, vacancy and vacancy-hydrogen were postulated to transport hydrogen in some PV silicon materials at low temperatures.

In silicon, vacancy is known to have two acceptor levels, e_v^- and $e_v^=$ [129] and two donor levels e_v^+ and e_v^{++}. V^+ is only metastable because the positions of e_v^+ and e_v^{++} are inverted (so-called negative-U properties). There exist four stable charge state V^0, V^-, $V^=$, and V^{++}. As a result, vacancies can interact with charged hydrogen species. It is possible to write down the rate equations involving vacancies. However, related parameters are lacking and even the detection of monovacancies has technical problems. In the next section, past studies of this research group will be reviewed and vacancy-related diffusion mechanism previously proposed will be summarized.

2.8.3 Past Research on H diffusion in PV Silicon Materials

2.8.3.1 Experimental Observations. A few experimental observations were done by this group pertaining to the H diffusion profiles in different silicon materials supplied from various vendors by using different hydrogenation techniques. The diffusion behavior of H seems to have a strong dependence on the crystal growth parameters and residue impurity content [40], [72].

Hydrogen diffusion was conducted by ion beam hydrogenation technique on the silicon materials from different manufacturers. Samples that were compared for the diffusivity profiles were p-type FZ, CZ, cast polycrystalline material, edge defined film fed-growth (EFG from ASE Americas), and laser recrystallized ribbon (LRC). Samples selected had similar low doping level. They were cleaned and processed under Kaufman deuterium (D) ion beam source, with the energy of 1.5 KeV and current of 0.6 mA/cm^2, for the time duration of 30 min. The samples were heated to 250°C during the deuteration. Simultaneous diffusion was therefore expected. The profiles are shown in Figure 2.7 and apparent diffusivities fitted with complementary error function are shown in Figure 2.8.

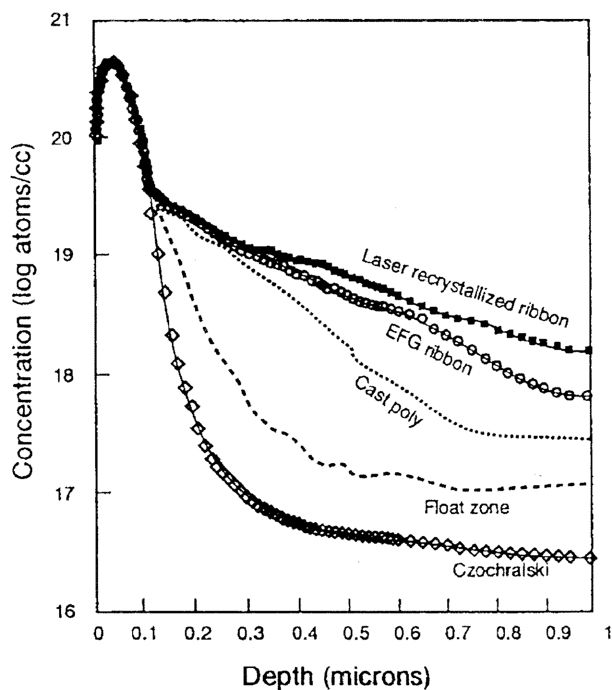

Figure 2.7 Hydrogen diffusion profiles for (a) LRC ribbon, (b) FZ, (c) CZ, and (d) EFG ribbon, by ion implantation.

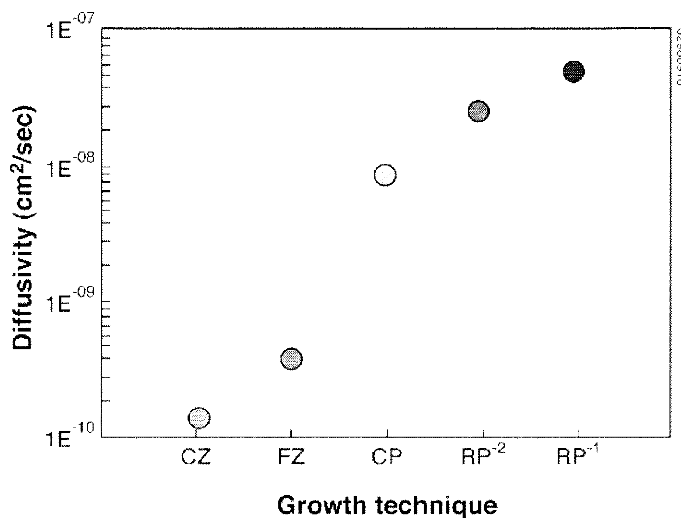

Figure 2.8 Apparent diffusivities fitted for materials grown with different methods.

It is interesting to relate the diffusivity to the crystal growth pulling speed and the residual impurity content of the material. These values are listed in Table 2.3.

Table 2.3 Oxygen and Carbon concentrations, and growth speeds for various types of silicon material that are used for solar cells.

Mark	Silicon Type	[O], [C] (atoms/cm^3)	Growth Rate (cm/min)
RP-1	LRC	$[O] < 10^{16}$	2.5
RP-2	EFG	$[O] < 10^{16}$, $[C] \sim 10^{18}$	1 ~ 2
CP	Cast-Poly	$[O] < 6\times10^{15}$, $[C] < 8\times10^{16}$	0.15~0.2
FZ	FZ	$[O] < 10^{16}$, $[C] < 10^{16}$.	0.3 ~ 0.5
CZ	CZ	$[O] > 10^{18}$, $[C] > 10^{17}$.	0.1 ~ 0.2

It was seen that although the processing conditions were the same for all the samples, the fitted diffusivity values showed a great difference of up to 3 orders of magnitude. There seems to have two regions controlled by different factors. CZ and FZ silicon samples usually have low crystal growth rate between 0.1 ~ 0.5 cm/min. The controlling factor is the oxygen concentration. It is known that FZ growth technique involves very low impurity level of oxygen, < 10^{16} cm^{-3}, whereas CZ growth technique causes a high oxygen level, typically > 10^{18} cm^{-3}. It seems that a lower oxygen level is associated with a higher apparent diffusivity of H or D. The second regime is where the crystal growth rate plays a critical role. For samples CP, RP-1, RP-2, the oxygen level is low (<10^{16} cm^{-3}), but they had a large difference in diffusivity mainly caused by the different pulling rates during crystal growth. In order to lower the cost, EFG ribbon growth usually seeks the maximum pulling rate that a ribbon sheet may endure. It seems that the diffusivity is higher for a higher pulling rate, which was presumably related to the concentration of intrinsic crystal defect involved during the crystal growth.

2.8.3.2 Explanations Proposed. A few explanations were proposed based on Figure 2.8 and Table 2.3. The reason for the effect of the growth rates on the diffusivity is that rapidly grown material can have a high number of vacancy formations that may be "frozen" in the material when the sample is quenched after crystal growth. The presence of O in the growth reduces the inclination for vacancy formation in the silicon [130] and large amounts of carbon influence the diffusivity, such as in EFG material.

Theoretical calculations [131] revealed a possible diffusion mechanism that involves vacancy-hydrogen (H-V) complex. A series of configuration change is shown in Figure 2.9 that illustrates the migration of H-V complex in the silicon lattice. Beginning at Figure 2.9 (a), the thick (thin, dashed) lines indicate qualitatively the stronger (weaker, weakest) covalent bonds formed at the various stages of diffusion. Only one hydrogen or Si atoms is shown to move. Figure 2.9 (b) shows calculated barrier comparison for diffusion: solid line: neutral vacancy; dashed line: neutral vacancy-hydrogen; dotted line: +1 charge state. The horizontal axis roughly scales with the vertical coordinate of the Si atom that moves toward the vacancy during the reconfigurations.

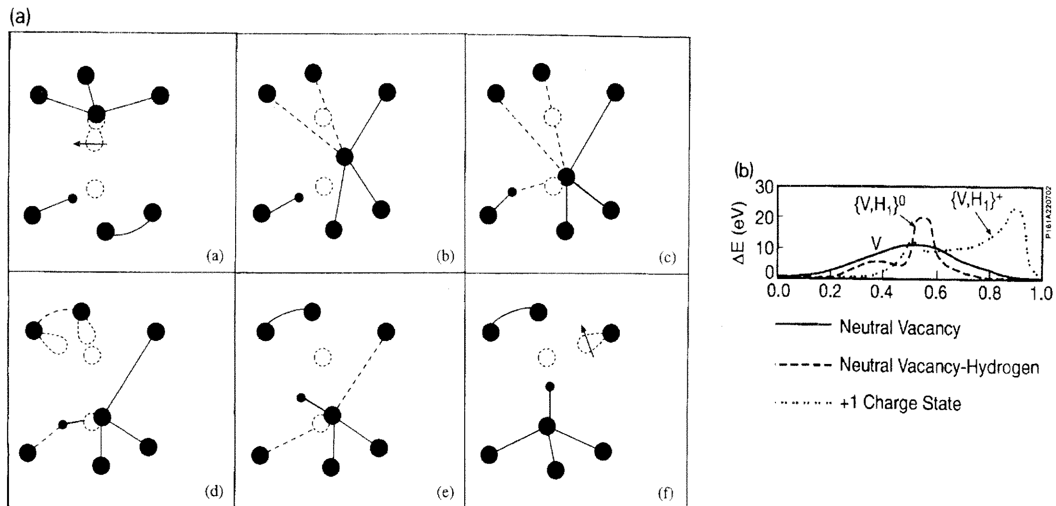

Figure 2.9 Schematic representation of the diffusion mechanism for the (V, H) pair in Si.

In previous studies, H was seen to diffuse into a Si wafer with a damaged surface in a forming gas ambient at low temperatures (200 - 400°C) [43]. One possible explanation is that hydrogen is split from its molecular form into the atomic form at damaged surface by the vacancies. Pankove et al. [32] first proposed that the surface damage created from the high acceleration voltage V_a of the plasma process can dissociate the molecular hydrogen. The bonding energy of the molecule H_2 in vacuum is 4.62 eV, while in the crystal it is 3.84 eV and the bonding energy of the atomic state is 3.43 eV; so it is feasible that a surface damage as a stressed lattice with very few energy states, could initially break this bond [132]. In effect, H_2 in Si and its interaction with intrinsic defects using *ab initio* tight-binding MD simulations showed that the potential energy between V infinitely far from H_2 and {V, H, H} is 4.0 eV [133].

In conclusion, previous studies on deuterium diffusion based on ion bean techniques on silicon materials prepared from different crystal growth method showed a strong dependence of apparent diffusivity on oxygen level and crystal growth pulling

rate. The underlying facilitating factor was proposed to be the participation of vacancy point defect. Direct evidence is required to elucidate the idea.

2.8.3.3 Vacancy and Hydrogen-vacancy Complex Facts. The simplest imperfections in silicon is a vacancy, or a missing atom. Vacancies are present in a crystal for a number of reasons as illustrated in the previous sections. These are the growth speed, the concentration of O that predominates the number of vacancies, surface treatments such as hydrogen plasma, and etching or deposition of Al contacts. Prevention of vacancies would be an ideal option however most processing steps involve an existing product that contains vacancies.

Mono-vacancy is very mobile, which the activation energies for migration of V^0, V^{++} and $V^{=}$ are 0.45, 0.32 and 0.18 eV, respectively [134]. The divancy V_2 is more stable than two isolated mono-vacancies by 1.5 – 1.6 eV [135]. Vacancies are more abundant in p-type material than n-type, because self-interstitials easily trap at group III dopants such as boron (substitutional acceptor), which forms vacancies [136]. Vacancies react amiably with hydrogen as well as with defects and impurities including dopants.

Theoretical calculations have predicted that a vacancy can trap up to four hydrogen atoms [137]. Vacancies are one of the strongest traps for hydrogen. It is recognized that hydrogen ties up dangling bonds at vacancies, vacancy aggregates, surfaces and extended defects such as dislocations, grain boundaries, and interfaces.

It is difficult to directly identify the diffusion process mechanism by a {H-V} complex. Infrared (IR) spectroscopy is a common technique used to identify the species by the stretch and bending and wagging modes of the Si-H, however because the

absorption coefficients of hydrogen are very small it is a difficult technique to use. The bond character for vacancy related defects and interstitial-related defects are thought to be very similar, thus making it hard to distinguish with IR. There were theoretical advances in this study by Mukashev et al. [138] who indicated a difference between the bands by the temperature subservience and the H-D isotope dependence. It is known that the hydrogen peaks by IR spectroscopy range from 2300 cm^{-1} to 1800 cm^{-1}. The peaks below 2000 cm^{-1} are thought to be related to interstitials and the peaks above 2000 cm^{-1} are vacancy related. There is no direct experimental evidence verifying this notion. Vibrational spectra of the H-V complexes have been obtained theoretically by Park et al. [132] by using the pseudo-atomic-orbital MD method.

The peaks of the calculations were found to be at 2168 cm^{-1}, 2268 cm^{-1}, 2301 $^{-1}$, and 2334 cm^{-1} at room temperature vibrational frequencies. The vibrational frequencies for H in the $\{V,H_n\}$, are with n=1, 2, 3, and 4, respectively. These values have been found to be high compared to experimental results that give vibrational modes at 2060 cm^{-1}, 2120 cm^{-1}, 2160 cm^{-1}, and 2220 cm^{-1}. The experimental results from Nielson et al [139] indicate the vibrational mode at 2220 cm^{-1} identified as the VH_4 2160 cm^{-1} and 2120 cm^{-1} relating to the VH_3 and VH_2 vibrational modes respectively. Another mode at 2060 cm^{-1} is tentatively assigned to the VH_0. It is agreed that the H-stretching frequency of $\{V,H_n\}$ increases with n, which results from a population effect of an increasing number of H squeezing into a vacancy.

CHAPTER 3

MODELING OF HYDROGEN DIFFUSION IN CRYSTALLINE SILICON

3.1 Introduction to Modeling of Hydrogen Diffusion in Silicon

In an ideal case, based on one simple diffusive mechanism and constant surface boundary condition, an impurity diffusion profile should be a complementary error function (erfc) distribution. Experimentally measured diffusion profiles of H/D are known to differ significantly from ideal erfc profiles. As summarized in the previous chapter, the spread of diffusivity value fitted from low temperature data possesses a much greater value than the experimental uncertainty. These values cannot be fitted by an exponential law $D = D_0 \, exp \, (-E_A \, / \, kT)$, with a consistent value for the activation energy E_A and for pre-exponential factor D_0 over the complete temperature range. The "apparent" diffusion coefficients at low temperatures are usually several orders of magnitude lower than the extrapolated values from the high temperature diffusivity relation [112]. Corbett et al. [140] showed a set of comprehensive experimental diffusion profiles in FZ n- and p-type vs. temperature and vs. resistivity, which illustrated a great variation among the samples processed under different conditions. This has been the case in other reported deuterium profiles, such as reported in [141] and [142].

Several diffusion models have been proposed to describe the hydrogen profiles. Inspired by the self-regulated drift of donor Li^+ ions in p-type Si or Ge [143], the hydrogen was postulated to have a donor level in p-type Si [122], [144]. H as a donor can contribute to the electrical deactivation through acceptor compensation. H gradient across the doping level forms an n-p junction. Consequently, H^+ would drift in the junction field. The result is an H concentration pinned at doping level, forming a plateau.

Attempt was then made to include boron impurities trapping-detrapping and H_2 formation [144] in highly doped p-Si (~10^{18} cm^{-3}). However, the simulation failed to account for the profile and either one of the mechanisms had to be neglected. D. Mathiot proposed a model [145] that hydrogen can exist in 3 charge states H^0, H^+ and H^- due to acceptor and/or donor in the band gap. Different charge state species drift in the built-in field and pairs with ionized dopant are formed through Coulombic attraction leading to neutral complexes. A constant surface concentration (C_s) and a time-independent surface trap density were included in the model. H_2 formation was allowed, but was later excluded in an improved version of the model [141]. The simulation turned out to agree well with some of the experimental curves. For doping concentration greater than 10^{16} cm^{-3}, H_2 formation seems negligible. However, there was flexibility of adjusting various parameters in such a model. The surface concentration was assumed to be ~10^{18} cm^{-3}, which was too large, and diffusivities of atomic hydrogen was 10^{-14} ~ 10^{-13} cm^2s^{-1}, which was too small. Other trapping mechanisms were not considered, except a very shallow surface trap density was nominally assumed. Moreover, the acceptor and donor levels of hydrogen used in the model turned out to be incorrect and do not have a "negative-U" property.

A large set of parameters may fit a curve well, but that may not be a unique solution. Simplified models were developed to focus on fewer physical origins of the diffusion problem. Kalejs et al. proposed a model [146] that involves a constant immobile bulk trap density to describe hydrogen diffusion in B-doped Si at 150 °C. Although the surface traps are neglected, the propagation rate of the diffusion front was obtained and matched with actual data. The surface hydrogen concentration C_s was

assumed to be a constant. The early model proposed by Borenstein et al. [147] incorporated H_2 formation and a bulk trapping mechanism with a constant C_s but failed to describe the shoulder region of moderately doped FZ-Si profile. In order to describe the exponential depth profiles observed, a multiple trapping of hydrogen at impurity sites, was modeled by Tchlchinsky et al [148] and various possible configurations were investigated by Korpas et al [149] by using the *ab initio* method. However, applying multiple trapping to both surface and bulk region could not fit the experimental curves very well [150].

Throughout the modeling efforts, a high concentration of near-surface layer and the shoulder region has been observed, where hydrogen concentration far exceeds the doping level. High-concentration region is believed due to trapping at process-induced defects. Some data clearly showed that plasma exposure can cause such a layer, and it extends deeper into the bulk for a longer exposure time. In previous experiments of low-energy (~ 1.5 KeV) hydrogen implantation under a controlled temperature (~250 °C), it was observed that the damage layer did propagate into the bulk. The damage layer was seen from the large amount of trapped hydrogen near the surface. The extracted diffusivity data indicated a retarded diffusion process: if fitted with a single complimentary error function, the effective diffusion time is a fraction of the actual diffusion time for the 2-hour diffusion process. For those hydrogenation processes that introduce surface damage, it is important to include such an effect in the diffusion model.

As reviewed in chapter 2, in some cases, enhanced hydrogen diffusion can be observed in PV silicon materials with ion beam hydrogenation techniques. It is likely in

an ion implantation process that some type of mobile traps may be involved and this effect also needs to be included in the diffusion model.

Since hydrogenation is a very attractive passivation technique for PV cell processing, modeling hydrogen diffusion and passivation with the existence of a p-n junction is an important topic. There is some introduction and qualitative interpretation in the literature, such as [151], but a direct simulation and/or a method is lacking to give a more insight to the problem. In this chapter, a "complete" diffusion model will be developed, which takes into account charge state conversion, combination and dissociation at dopant and trap sites, mobile traps, and junction field. Numerical implementation and limiting cases will be discussed. Of course, there is no such model that is "complete", because in reality unexpected mechanisms may be involved.

3.2 Formulation of the "Complete" Diffusion Model

To consider a diffusion model that has various mechanisms described in the previous section, some of the fundamental equations reviewed in chapter 2 are used here. The equations are grouped as:

- Relative density of $[H]$ among the three charge states of hydrogen in silicon, (H^+, H^0, H^-): the first order approximation of Eqs. (2.12) and (2.13) yields the relations among populations of species H^+, H^0, and H^- in terms of total atomic hydrogen [H],

$$[H^0] = \left(\delta^+ e^{-\frac{\phi}{V_T}} + 1 + \delta^- e^{\frac{\phi}{V_T}} \right)^{-1} [H] . \tag{3.1}$$

$$[H^+] = [H^0] \delta^+ e^{-\frac{\phi}{V_T}} , \tag{3.2}$$

$$[H^-] = [H^0]\delta^- e^{\frac{\phi}{V_T}}, \tag{3.3}$$

where $\delta^+ \equiv e^{\beta(E_d - E_i)}$, and $\delta^- \equiv e^{\beta(E_i - E_a)}$.

- Electron and hole density as a function of Fermi level:

$$n = n_i e^{\beta(E_f - E_i)} = n_i e^{\frac{\phi}{V_T}}, \tag{3.4}$$

$$p = n_i e^{-\beta(E_f - E_i)} = n_i e^{-\frac{\phi}{V_T}}. \tag{3.5}$$

- Poisson's equation:

$$\nabla^2 \phi = -\frac{\rho(\vec{x})}{\varepsilon_s} = -\frac{e}{\varepsilon_s}\left[(p-n) + ([H^+] - [H^-]) + (n_D^+ - p_A^-)\right]. \tag{3.6}$$

- Rate equations for concentrations of donor-hydrogen complex, [*DH*], and acceptor-hydrogen complex, [*AH*] – interaction with shallow level dopants.

$$\frac{\partial[DH]}{\partial t} = k_{DH}[D^+][H^-] - k'_{DH}[DH], \tag{3.7}$$

$$\frac{\partial[AH]}{\partial t} = k_{AH}[A^-][H^+] - k'_{AH}[AH]. \tag{3.8}$$

Rate equations for concentrations of trap-hydrogen complex, [*TH*], and mobile-trap-hydrogen complex, [*VH*].

Here, two types of traps are included: fixed traps, which may be a function of time and position but are immobile, and mobile traps, which are mainly induced by the hydrogenation process:

$$\frac{\partial[TH]}{\partial t} = k_{TH}[T][H] - k'_{TH}[TH], \tag{3.9}$$

$$\left(\frac{\partial[VH]}{\partial t}\right)^* = k_{VH}[V][H] - k'_{VH}[VH]. \tag{3.10}$$

- Flux of hydrogen species with different charge states and mobile-trap-hydrogen complex:

$$\vec{J}_+ = -D_+\nabla[H^+] + \mu_+[H^+]\vec{E} = -D_+\left(\nabla[H^+] + \frac{k_B T}{e}[H^+]\nabla\phi\right), \tag{3.11}$$

$$\vec{J}_0 = -D_0\nabla[H^0], \tag{3.12}$$

$$\vec{J}_- = -D_-\nabla[H^-] - \mu_-[H^-]\vec{E} = -D_-\left(\nabla[H^-] - \frac{k_B T}{e}[H^-]\nabla\phi\right), \tag{3.13}$$

$$\vec{J}_H = \vec{J}_+ + \vec{J}_0 + \vec{J}_-, \tag{3.14}$$

$$\vec{J}_{VH} = -D_{VH}\nabla[VH]. \tag{3.15}$$

- Continuity equations for mobile species': total atomic hydrogen, mobile-trap-hydrogen complex, and mobile traps:

$$\frac{\partial[H]}{\partial t} = -\nabla\cdot\vec{J}_H - \frac{\partial[DH]}{\partial t} - \frac{\partial[AH]}{\partial t} - \frac{\partial[TH]}{\partial t} - \left(\frac{\partial[VH]}{\partial t}\right)^*, \tag{3.16}$$

$$\frac{\partial[VH]}{\partial t} = -\nabla\cdot\vec{J}_{VH} + \left(\frac{\partial[VH]}{\partial t}\right)^*, \tag{3.17}$$

$$\frac{\partial[V]}{\partial t} = -D_V\nabla^2[V] - \left(\frac{\partial[VH]}{\partial t}\right)^*, \tag{3.18}$$

where,

$$[H^+] + [H^0] + [H^-] = [H]. \tag{3.19}$$

It should be noted that $\frac{\partial[VH]}{\partial t}$ differs from $\left(\frac{\partial[VH]}{\partial t}\right)^*$ in that $\left(\frac{\partial[VH]}{\partial t}\right)^*$ is the local change rate of [VH] whereas $\frac{\partial[VH]}{\partial t}$ also include the additional accumulation / depletion of the species due to diffusion flow into / out of a coordinate point.

There are constraints associated with the above equations, i.e.,

$$[T]+[HT]=[T]_{tot},\ [H]\geq 0,\ [VH]\geq 0,\ [V]\geq 0,$$

$$[DH]\leq [D]_{tot},\ [AH]\leq [A]_{tot},\ [TH]\leq [T]_{tot}. \tag{3.20}$$

To verify the conservation of continuity equation of total hydrogen concentration, Eqs. (3.16) and (3.17) are added, and the following relation is obtained:

$$\frac{\partial}{\partial t}([H]+[DH]+[AH]+[TH]+[VH])=-\nabla\cdot\left(\vec{J}_H+\vec{J}_{VH}\right), \tag{3.21}$$

which is actually $\frac{\partial [H]_{tot}}{\partial t}+\nabla\cdot\vec{J}_{tot}=0$, and hence the general continuity equation of total hydrogen species is conserved.

3.2.1. Solving Poisson's Equation with Dual-level "Negative-U" Impurity

Modeling of a general diffusion problem that involves charge and carrier exchange requires simultaneous solution of several coupled differential equations including Poisson equation for electric potential, continuity equations for diffusing species, rate equations for local kinetics. To model a semiconductor device, the Poisson's equation needs to be solved together with continuity equations for electron and hole currents. As a result of the coupling, carrier densities are nonlinear functions of the electric potential, which leads to the nonlinear Poisson equation. If, besides shallow donor / acceptor dopants, another impurity is involved, which possesses extra energy levels in the bandgap, the nonlinear Poisson equation will have more nonlinear terms and become more complicated. An example is hydrogen. As reviewed in chapter 2, evidence showed that hydrogen has a donor level about 0.2 eV below the conduction band and an acceptor level

about 0.1 or 0.2 eV below the donor level. Both the donor and the acceptor levels appear in the upper half of the bandgap. Above room temperature, several charge states may coexist. If the concentration of total atomic hydrogen is high, the contribution of nonlinear terms due to hydrogen charge states cannot be neglected.

The conventional approach to solve nonlinear Poisson's equation that coupled with continuity equations which involve one shallow donor and one acceptor, is based on the application of Newton's method. Gummel's algorithm [152] (or its modified version [153]) is the most commonly used algorithm. This method is based on block-Successive Over-Relaxation (SOR)-Newton method, which was first suggested by Gummel. It solves for the electric potential, $\phi^{(k+1)}$, of next iterative step by using the current step ($\phi^{(k)}$, $n^{(k)}$, $p^{(k)}$) except the carrier concentrations are re-substituted by terms that are related to the difference of potentials of next iterative step and current step. Following the treatment by Mock [154], Gummel's method can be classified as iterating a mapping of the following type:

$$\frac{\varepsilon}{e}\nabla^2\phi^{(k+1)} - r\left(\phi^{(k+1)} - \phi^{(k)}\right) - \left(n^{(k)} - p^{(k)} - N_{DA}\right) = 0, \tag{3.22}$$

where $N_{DA} = n_D^+ - p_A^-$ and at room temperature, $N_{DA} = N_D - N_A$. The damping function for the method $r = \frac{1}{V_T}\left(n^{(k)} + p^{(k)}\right)$, where the thermal voltage $V_T \equiv \frac{kT}{e}$. There are other alternate choices for r. Gummel's method has been used extensively in device modeling. For example, Stanford's PISCES-II [155] uses Gummel method and the direct Newton method. Gummel method has proven to be extraordinarily valuable in practice. Convergence can be observed in many applications. However, difficulties have been observed when the generation/recombination rate is high or injection is high, which can

be actual cases in PV materials. A general proof of convergence of the method has not been established [156]. This difficulty is because the Newton's method has a local convergence. Mayergoyz [157] published a new iterative method and proved its global convergence, but the method only consider a general problem of one shallow donor dopant and one shallow acceptor dopant.

This section will extend Mayergoyz's method to a more general case that can be applicable to solve hydrogen charge state equilibrium problem. Besides one shallow donor and one shallow acceptor dopant, an additional impurity is added to the system that possesses both deep donor and acceptor levels. A new procedure will be developed and its global convergence will be proved.

As derived in the previous section, the concentrations of hydrogen of charge state, H^+, H^0, and H^- are given in Eqs. (3.1), (3.2), and (3.3), in terms of total atomic hydrogen species, H. By substituting expressions of $[H^+]$, $[H^0]$, $[H^-]$, electron and hole densities, (3.4) and (3.5) into the Poisson's Eq. (3.8), the following expression is obtained:

$$-\nabla^2\phi + \frac{e}{\varepsilon}n_i\left(e^{\frac{\phi}{V_T}} - e^{-\frac{\phi}{V_T}}\right) + \frac{e}{\varepsilon_s}[H]\frac{\delta^- e^{\frac{\phi}{V_T}} - \delta^+ e^{-\frac{\phi}{V_T}}}{\delta^- e^{\frac{\phi}{V_T}} + 1 + \delta^+ e^{-\frac{\phi}{V_T}}} = \frac{e}{\varepsilon_s}N_{DA}. \quad (3.23)$$

For an unbiased sample, the boundary condition for ϕ can be determined by assuming charge neutrality at the sample surface, i.e.,

$$\nabla^2\phi\big|_S = 0. \quad (3.24)$$

Eqs. (3.23) and (3.24) constitute a boundary value problem that needs to be solved.

A solution of analytical form is obviously not possible. In order to solve Eq. (3.23) numerically, a finite difference discretization scheme is adopted. In a 2-dimension case, a set of meshlines are constructed parallel to coordinate axes. Indices i and j are

used to number the meshlines which intersect x and y axes, respectively. The mesh points are the intersecting points of the meshlines. Each (i,j) pair indicates such a mesh point.

Eq. (3.23) can be discretized following a five-point finite difference approximation to the following form

$$\frac{2}{h_i+h_{i-1}}\left(\frac{\phi_{i+1,j}-\phi_{i,j}}{h_i}+\frac{\phi_{i-1,j}-\phi_{i,j}}{h_{i-1}}\right)+\frac{2}{k_j+k_{j-1}}\left(\frac{\phi_{i,j+1}-\phi_{i,j}}{k_j}+\frac{\phi_{i,j-1}-\phi_{i,j}}{k_{j-1}}\right)+$$

$$+\frac{e}{\varepsilon}n_i\left(e^{\frac{\phi_{i,j}}{V_T}}-e^{-\frac{\phi_{i,j}}{V_T}}\right)+\frac{e}{\varepsilon_s}[H]_{i,j}\frac{\delta^- e^{\frac{\phi_{i,j}}{V_T}}-\delta^+ e^{-\frac{\phi_{i,j}}{V_T}}}{\delta^- e^{\frac{\phi_{i,j}}{V_T}}+1+\delta^+ e^{-\frac{\phi_{i,j}}{V_T}}}=\frac{e}{\varepsilon_s}N_{DA}^{i,j}, \tag{3.25}$$

which can be rewritten as

$$\alpha_{i,j}^{+0}u_{i+1,j}+\alpha_{i,j}^{-0}u_{i-1,j}+\alpha_{i,j}^{0+}u_{i,j+1}+\alpha_{i,j}^{0-}u_{i,j-1}-\alpha_{i,j}^{00}u_{i,j}+$$

$$+\beta_{i,j}\left(e^{u_{i,j}}-e^{-u_{i,j}}\right)+\gamma_{i,j}\frac{\delta^- e^{u_{i,j}}-\delta^+ e^{-u_{i,j}}}{\delta^- e^{u_{i,j}}+1+\delta^+ e^{-u_{i,j}}}=f_{i,j}, \tag{3.26}$$

where $u_{i,j}=\frac{\phi_{i,j}}{V_T}$, and

$$\alpha_{i,j}^{+0}=\frac{2}{h_i+h_{i-1}}\frac{1}{h_i}(h_ik_j),\ \alpha_{i,j}^{-0}=\frac{2}{h_i+h_{i-1}}\frac{1}{h_{i-1}}(h_ik_j),$$

$$\alpha_{i,j}^{0+}=\frac{2}{k_j+k_{j-1}}\frac{1}{k_j}(h_ik_j),\ \alpha_{i,j}^{0-}=\frac{2}{k_j+k_{j-1}}\frac{1}{k_{j-1}}(h_ik_j),$$

$$\alpha_{i,j}^{00}=\frac{2}{h_i+h_{i-1}}\left(\frac{1}{h_i}+\frac{1}{h_{i-1}}\right)(h_ik_j)+\frac{2}{k_j+k_{j-1}}\left(\frac{1}{k_j}+\frac{1}{k_{j-1}}\right)(h_ik_j), \tag{3.27}$$

$$\beta_{i,j}=\frac{en_i}{\varepsilon_s}\frac{h_ik_j}{V_T}, \tag{3.28}$$

$$\gamma_{i,j} = \frac{e[H]_{i,j}}{\varepsilon_s} \frac{h_i k_j}{V_T}, \tag{3.29}$$

$$f_{i,j} = \frac{eN_{DA}^{i,j}}{\varepsilon_s} \frac{h_i k_j}{V_T}. \tag{3.30}$$

There are some important properties of the coefficient α's at mesh point (i, j) as follows:

$$\alpha_{i,j}^{+0} \geq 0, \ \alpha_{i,j}^{-0} \geq 0, \ \alpha_{i,j}^{0+} \geq 0, \ \alpha_{i,j}^{0-} \geq 0,$$

$$\alpha_{i,j}^{00} \geq \alpha_{i,j}^{+0} + \alpha_{i,j}^{-0} + \alpha_{i,j}^{0+} + \alpha_{i,j}^{0-}. \tag{3.31}$$

The numerical scheme of solving Eq. (3.26) is to split the equation into two parts. The method consists of two loops of iterations. In order to obtain quantities, $F_{i,j}^{(k+1)}$, for the next iteration in the outer loop of nonlinear equations,

$$\alpha_{i,j}^{00} u_{i,j}^{(k+1)} + \beta_{i,j}\left(e^{u_{i,j}^{(k+1)}} - e^{-u_{i,j}^{(k+1)}}\right) + \gamma_{i,j} \frac{\delta^- e^{u_{i,j}^{(k+1)}} - \delta^+ e^{-u_{i,j}^{(k+1)}}}{\delta^- e^{u_{i,j}^{(k+1)}} + 1 + \delta^+ e^{-u_{i,j}^{(k+1)}}} - F_{i,j}^{(k+1)} = 0, \tag{3.32}$$

$$F_{i,j}^{(k+1)} = \alpha_{i,j}^{+0} u_{i+1,j}^{(k)} + \alpha_{i,j}^{-0} u_{i-1,j}^{(k)} + \alpha_{i,j}^{0+} u_{i,j+1}^{(k)} + \alpha_{i,j}^{0-} u_{i,j-1}^{(k)} - f_{i,j}^{(k)}, \tag{3.33}$$

need to be calculated at each mesh points. Eq. (3.32) can be solved by Newton's method, which constitute an inner loop with a function defined as

$$\Psi\left(u_{i,j}^{(k+1)}\right) = \alpha_{i,j}^{00} u_{i,j}^{(k+1)} + \beta_{i,j}\left(e^{u_{i,j}^{(k+1)}} - e^{-u_{i,j}^{(k+1)}}\right) + \gamma_{i,j} \frac{\delta^- e^{u_{i,j}^{(k+1)}} - \delta^+ e^{-u_{i,j}^{(k+1)}}}{\delta^- e^{u_{i,j}^{(k+1)}} + 1 + \delta^+ e^{-u_{i,j}^{(k+1)}}} - F_{i,j}^{(k+1)}, \tag{3.34}$$

of which the derivative is

$$\Psi'\left(u_{i,j}^{(k+1)}\right) = \alpha_{i,j}^{00} + \beta_{i,j}\left(e^{u_{i,j}^{(k+1)}} + e^{-u_{i,j}^{(k+1)}}\right) + \gamma_{i,j} \frac{4\delta^-\delta^+ + \delta^- e^{u_{i,j}^{(k+1)}} + \delta^+ e^{-u_{i,j}^{(k+1)}}}{\left(\delta^- e^{u_{i,j}^{(k+1)}} + 1 + \delta^+ e^{-u_{i,j}^{(k+1)}}\right)^2}. \tag{3.35}$$

The Newton's method here is to calculate

$$u_{i,j}^{(k+1),(\nu+1)} = u_{i,j}^{(k+1),(\nu)} + \Delta u_{i,j}^{(\nu)}, \tag{3.36}$$

$$\Delta u_{i,j}^{(\nu)} = -\frac{\Psi\left(u_{i,j}^{(k+1),(\nu)}\right)}{\Psi'\left(u_{i,j}^{(k+1),(\nu)}\right)}. \tag{3.37}$$

It is obvious that

$$4\delta^-\delta^+ + \delta^- e^{u_{i,j}^{(k+1)}} + \delta^+ e^{-u_{i,j}^{(k+1)}} \geq 4\delta^-\delta^+ + 2\sqrt{\delta^-\delta^+} = 4e^{\beta(E_d-E_a)} + 2e^{\frac{1}{2}\beta(E_d-E_a)} \geq 0 \tag{3.38}$$

under the circumstance of "negative U property" of an impurity, i.e., $E_d > E_a$. From Eq. (3.35), it can be seen that the derivative of function $\Psi(u)$ is always positive, which indicates that function $\Psi(u)$ is monotonically increasing. Also because $E_d > E_a$, the electric potential has a unique solution. In conclusion, Netwon's method of inner loop converges for "negative U" impurity, e.g. hydrogen.

3.2.2. Convergence of the Method

To prove the convergence of the outer loop of Eq. (3.32), the following notation is introduced:

$$\delta_{i,j}^{(k+1)} = u_{i,j}^{(k+1)} - u_{i,j}^{(k)}, \tag{3.39}$$

which represents the difference of solution between adjacent iteration steps. By subtracting the (3.32) of *(k+1)*th from the same equation of *(k)*th step, the following equation can be written:

$$\alpha_{i,j}^{00}\delta_{i,j}^{(k+1)} + \beta_{i,j}\left[\left(e^{u_{i,j}^{(k+1)}} - e^{-u_{i,j}^{(k+1)}}\right) - \left(e^{u_{i,j}^{(k)}} - e^{-u_{i,j}^{(k)}}\right)\right] + \gamma_{i,j}\left[\frac{\delta^- e^{u_{i,j}^{(k+1)}} - \delta^+ e^{-u_{i,j}^{(k+1)}}}{\delta^- e^{u_{i,j}^{(k+1)}} + 1 + \delta^+ e^{-u_{i,j}^{(k+1)}}} - \frac{\delta^- e^{u_{i,j}^{(k)}} - \delta^+ e^{-u_{i,j}^{(k)}}}{\delta^- e^{u_{i,j}^{(k)}} + 1 + \delta^+ e^{-u_{i,j}^{(k)}}}\right]$$

$$= \alpha_{i,j}^{+0}\delta_{i+1,j}^{(k)} + \alpha_{i,j}^{-0}\delta_{i-1,j}^{(k)} + \alpha_{i,j}^{0+}\delta_{i,j+1}^{(k)} + \alpha_{i,j}^{0-}\delta_{i,j-1}^{(k)}. \tag{3.40}$$

We introduce auxiliary variables

$$u_{i,j}(\lambda) = u_{i,j}^{(k)} + \lambda u_{i,j}^{(k+1)} \quad (0 \leq \lambda \leq 1). \tag{3.41}$$

Using this set of variables, we can transform the exponential terms in the brackets of (3.40):

$$\left(e^{u_{i,j}^{(k+1)}} - e^{-u_{i,j}^{(k+1)}}\right) - \left(e^{u_{i,j}^{(k)}} - e^{-u_{i,j}^{(k)}}\right) = \int_0^1 \frac{d}{d\lambda}\left(e^{u_{i,j}(\lambda)} - e^{-u_{i,j}(\lambda)}\right) d\lambda$$

$$\left(\because e^{u_{i,j}(\lambda)} + e^{-u_{i,j}(\lambda)} \geq 2\right) = \delta_{i,j}^{(k+1)} \int_0^1 \left(e^{u_{i,j}(\lambda)} + e^{-u_{i,j}(\lambda)}\right) d\lambda \geq 2\delta_{i,j}^{(k+1)}, \tag{3.42}$$

and,

$$\frac{\delta^- e^{u_{i,j}^{(k+1)}} - \delta^+ e^{-u_{i,j}^{(k+1)}}}{\delta^- e^{u_{i,j}^{(k+1)}} + 1 + \delta^+ e^{-u_{i,j}^{(k+1)}}} - \frac{\delta^- e^{u_{i,j}^{(k)}} - \delta^+ e^{-u_{i,j}^{(k)}}}{\delta^- e^{u_{i,j}^{(k)}} + 1 + \delta^+ e^{-u_{i,j}^{(k)}}}$$

$$= \int_0^1 \frac{d}{d\lambda}\left(\frac{\delta^- e^{u_{i,j}(\lambda)} - \delta^+ e^{-u_{i,j}(\lambda)}}{\delta^- e^{u_{i,j}(\lambda)} + 1 + \delta^+ e^{-u_{i,j}(\lambda)}}\right) d\lambda = \delta_{i,j}^{(k+1)} \int_0^1 \left[\frac{4\delta^-\delta^+ + \delta^- e^{u_{i,j}(\lambda)} + \delta^+ e^{-u_{i,j}(\lambda)}}{\left(\delta^- e^{u_{i,j}(\lambda)} + 1 + \delta^+ e^{-u_{i,j}(\lambda)}\right)^2}\right] d\lambda$$

$$\left(\because \frac{4\delta^-\delta^+ + \delta^- e^{u_{i,j}(\lambda)} + \delta^+ e^{-u_{i,j}(\lambda)}}{\left(\delta^- e^{u_{i,j}(\lambda)} + 1 + \delta^+ e^{-u_{i,j}(\lambda)}\right)^2} \geq 0\right)$$

$$= \eta\delta_{i,j}^{(k+1)}, \text{ where } \eta>0. \tag{3.43}$$

From Eq. (3.40), together with property (3.31) and Eqs. (3.42) and (3.43), the following estimate can be derived:

$$\delta_{i,j}^{(k+1)} \leq \frac{\alpha_{i,j}^{00}}{\alpha_{i,j}^{00} + (2+\eta)\beta_{i,j}} \delta_{i,j}^{(k)}, \tag{3.44}$$

or,

$$\max_{i,j}\left|\phi_{i,j}^{(k+1)} - \phi_{i,j}^{(k)}\right| \leq q \cdot \max_{i,j}\left|\phi_{i,j}^{(k)} - \phi_{i,j}^{(k-1)}\right|, \tag{3.45}$$

$$\text{where } 0 < q = \max_{i,j} \frac{\alpha_{i,j}^{00}}{\alpha_{i,j}^{00} + (2+\eta)\beta_{i,j}} < 1. \tag{3.46}$$

According to Eqs. (3.45) and (3.46), the iteration of the outer loop, defined by Eqs. (3.32) and (3.33), forms a contracting sequence and converges with a geometric rate.

Since both inner and outer loops show convergence, this method guarantees a global convergence, and thus, in principle, any initial guess can be used. It may be noted that the boundary condition used here is charge neutrality at surface in Eq. (3.24). It is possible to expand the charge neutrality to the bulk and to use such a solution as initial guess. In this case, Eq. (3.24) is used both at the surface and in the bulk. Expanding the expression, it results in

$$\frac{e}{\varepsilon}n_i\left(e^{\frac{\phi^0}{V_T}}-e^{-\frac{\phi^0}{V_T}}\right)+\frac{e}{\varepsilon_s}[H]\frac{\delta^- e^{\frac{\phi^0}{V_T}}-\delta^+ e^{-\frac{\phi^0}{V_T}}}{\delta^- e^{\frac{\phi^0}{V_T}}+1+\delta^+ e^{-\frac{\phi^0}{V_T}}}-\frac{e}{\varepsilon_s}N_{DA}=0 \tag{3.47}$$

where ϕ^0 stands for the initial guess of the electric potential. ϕ^0 is bounded between –0.56 to 0.56 eV for silicon, and is known to have a unique solution. Several algorithms can be used to find the root of the nonlinear Eq. (3.47). An excellent algorithm is the Brent's method, which was developed in 1960s by van Wijngaarden, Dekker, and others, and later improved by Brent [158]. The reason why the charge neutrality condition can give a good initial guess can be seen from the scaled Poisson's equation in the following form [159]:

$$\lambda^2\nabla^2\phi = n - p - N_{DA}, \tag{3.48}$$

where λ is a very small parameter. As a first order approximation, the left-hand side of Eq. (3.48) can be neglected and the charge neutrality condition is obtained.

In this section, an iterative method based on finite difference discretization is discussed for solving nonlinear Poisson's equation that involves "negative U" impurity. The global convergence was proved. The charge neutrality solution can serve as a good initial input for the iteration. In next section, fully coupled diffusion problem will be solved by coupling the Poisson's equation to the continuity equations.

3.2.3 Solving Hydrogen Diffusion Problem

This section will introduce a numerical algorithm to solve the fully coupled equations described in Section 3.2. The same finite difference method as in the previous section will be used to discretize other position-related equations. Concentration distributions of H, DH, AH, TH, VH, and V constitute a variable set that fully describes the state of the diffusion system. Let vector

$$[\vec{H}]^{(k)} \equiv \{[H]^{(k)},[DH]^{(k)},[AH]^{(k)},[TH]^{(k)},[VH]^{(k)},[V]^{(k)}\} \tag{3.49}$$

For the time-stepping, an implicit finite difference method can be employed such that

$$\frac{[\vec{H}]^{(k+1)} - [\vec{H}]^{k}}{\delta t} = \Phi\left([\vec{H}]^{(k+½)}\right), \tag{3.50}$$

where the function, Φ, is an abstract function of all related variables and formulation on the right hand side of the coupled equations. The notation, $(k+½)$, stands for mid-time step between (k)th and $(k+1)$th step. This class of method was first proposed by Crank and Nicolson [160]. An implicit method can greatly improve the stability of the calculation, because in calculation for each time step, part of the solution for next time step is taken into account. One may thus use larger and fewer time steps.

A critical parameter here is the finite time step, δt. Consider a simple diffusion equation with a constant diffusion coefficient D, for a plane sheet of thickness l,

$$\frac{\partial C}{\partial t} = D\frac{\partial^2 C}{\partial x^2}. \tag{3.51}$$

With convenient variables:

$$X = \frac{x}{l},\ T = \frac{Dt}{l^2},\ \text{and}\ c = \frac{C}{C_0}, \tag{3.52}$$

Eq. (3.51) results in the scaled form:

$$\frac{\partial c}{\partial T} = \frac{\partial^2 c}{\partial X^2}. \tag{3.53}$$

It is interesting that all the scaled variables are dimensionless. By introducing a ratio,

$$r = \frac{\delta T}{(\delta X)^2}, \tag{3.54}$$

of a value close to 1, the discretized explicit form of Eq. (3.53) becomes

$$c_{i,j+1} = c_{i,j} + r\left(c_{i-1,j} - 2c_{i,j} + c_{i+1,j}\right), \tag{3.55}$$

which is well conditioned in the numerical sense. With some rearrangement, the time step, δt, becomes

$$\delta t = r\frac{\left(\min_{i,j}\left(\delta x_{i,j}\right)\right)^2}{D}. \tag{3.56}$$

The detailed flowchart of the algorithm is shown in Figure 3.1.

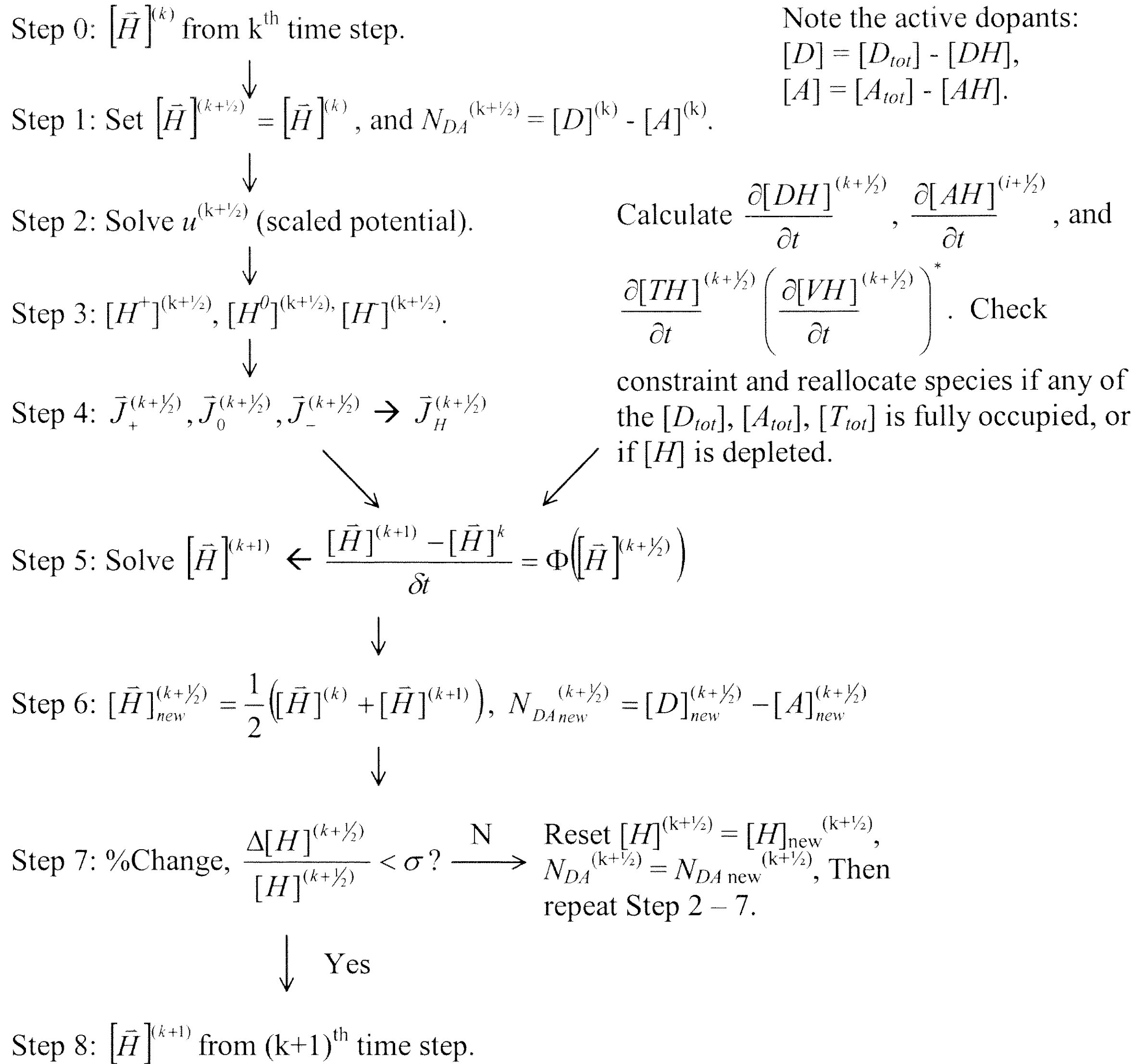

Figure 3.1 Flowchart diagram that illustrates the steps of solving fully coupled differential equations by numerical method.

At the beginning of the ($k+1$)th step calculation, mid-time step, ($k+½$), values in vector $\left[\vec{H}\right]^{(k+½)}$ are unknown. They are initially assigned with the results calculated from (k)th step. The electric potential and field distributions are then calculated by solving Poisson's equation using the method described in the previous section. Various charge state hydrogen species and hydrogen-containing complexes are then solved from the Boltzmann distribution and rate equations. Flows of mobile species are evaluated and substituted to the generalized time-stepping Eq. (3.51) to solve $\left[\vec{H}\right]^{(k+1)}$ for the ($k+1$)th step. Mid-time, ($k+½$), step values are then recalculated by averaging (k)th and ($k+1$)th step vectors for another iteration. Once convergence is detected for consecutive iterations, ($k+1$)th step is completed and the algorithm will proceed to the ($k+2$)th step .

In practice, at the beginning of the calculation when t is small, many iteration loops are usually required to achieve self-consistency of the solutions. As diffusion goes on and profiles of various species' get more evenly distributed, less number of iteration loops were needed for one time stepping. Since the time-step, dt, is many orders of magnitude smaller than the total time period, t, the electric potential and field distribution from one time step can be applied to the following time step as a good initial guess in solving the Poisson's equation.

3.2.4 1-D Mesh and 3-point Asymmetric Numerical Difference

In numerical calculation, the continuous space coordinate system needs to be approximated by a discrete space represented by a finite series of mesh points confined within certain boundaries. In solving a diffusion problem, because the concentration profiles usually consist of exponential components, it is sometimes a waste of

computation time to use a uniform mesh. Meshes used in many cases consist of non-uniform grid points. Two data arrays are used to keep track of the positions of individual grid points, x, and the spacing between adjacent mesh points, h, as illustrated in Figure 3.2.

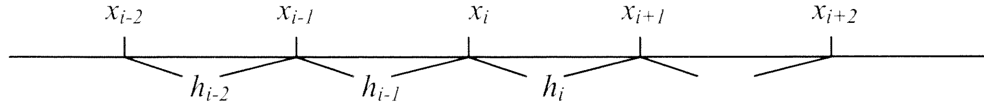

Figure 3.2 Illustration of structure and notations of a mesh.

Finite difference approximation of derivatives can be derived by comparing the combination coefficients with the Taylor's expansion coefficients. If the 3-point expression at mesh point, x_i, has the following forms for middle, forward, and backward difference, respectively, in the first column of the combination coefficients, a, b, c, will be listed in the second through fourth column in Table 3.1.

Table 3.1 Expressions of 3-point asymmetric middle, forward, and backward difference.

ϕ'	a	b	c
$ax_{i-1} + bx_i + cx_{i+1}$	$\frac{h_i}{h_{i-1}}\left(-\frac{1}{h_{i-1}+h_i}\right)$	$-(a+c)$	$\frac{h_{i-1}}{h_i}\left(-\frac{1}{h_{i-1}+h_i}\right)$
$ax_i + bx_{i+1} + cx_{i+2}$	$-(b+c)$	$\frac{h_i+h_{i+1}}{h_i}\frac{1}{h_{i+1}}$	$\frac{h_i}{h_i+h_{i+1}}\left(-\frac{1}{h_{i+1}}\right)$
$ax_{i-2} + bx_{i-1} + cx_i$	$\frac{h_{i-1}}{h_{i-2}+h_{i-1}}\frac{1}{h_{i-2}}$	$\frac{h_{i-2}+h_{i-1}}{h_{i-1}}\left(-\frac{1}{h_{i-2}}\right)$	$-(a+b)$

Second order derivatives can be derived by the similar method and are approximated by the following 3-point finite difference listed in Table 3.2.

Table 3.2 Expressions of 3-point asymmetric middle, forward, and backward difference.

φ''	a	b	c
$ax_{i-1} + bx_i + cx_{i+1}$	$\frac{2}{h_{i-1} + h_i}\frac{1}{h_{i-1}}$	$-(a+c)$	$\frac{2}{h_{i-1} + h_i}\frac{1}{h_i}$
$ax_i + bx_{i+1} + cx_{i+2}$	$-(b+c)$	$\frac{2}{h_{i+1}}\left(-\frac{1}{h_i}\right)$	$\frac{2}{h_{i+1}}\frac{1}{h_i + h_{i+1}}$
$ax_{i-2} + bx_{i-1} + cx_i$	$\frac{2}{h_{i-2}}\frac{1}{h_{i-2} + h_{i-1}}$	$\frac{2}{h_{i-2}}\left(-\frac{1}{h_{i-1}}\right)$	$-(a+b)$

3.3 Trap-limited Hydrogen Diffusion at Low Temperatures

3.3.1 Review and Introduction

Hydrogen (H) diffusion for impurity and defect passivation has been practically implemented at low temperatures, in the range of 250 – 400 °C, using plasma method or low-energy ion beam techniques. In photovoltaic (PV) applications, hydrogenation is routinely applied to PV cells to passivate the crystalline defects and impurities in the material. Deep bulk diffusion is desirable for PV compared to post metallization anneal (PMA) for MOS device fabrication, where only Si-SiO_2 interface passivation is of interest.

There have been many experimental profiles [60], [94], [140], [142] and diffusion models [122], [144], [141], [146], [147] published on H diffusion in silicon at low

temperatures. One of the challenges is to explain the H profiles that deviate from complementary error (erfc) functions due to the fact that hydrogen (H) spontaneously forms complex at defect and impurity sites and can get trapped. At present, the most cited diffusivity data is derived from the high temperature permeation VWW data as reviewed in Chapter 2. Several diffusion models [141], [144] took into account the charge state conversion as well as trapping at dopant sites of H and fitted profiles very well, but they could not justify the fitted parameters against VWW expressions. For example, surface concentration of mobile atomic H was assumed in Ref. [141] to be 10^{18} cm^{-3} and diffusivity of neutral H species 3.6×10^{-13} cm^2s^{-1} for diffusion in n-type silicon at 150ºC which is about 5 orders of magnitude lower than VWW diffusivity. It is possible to have low "effective" diffusivity values at low temperatures due to trapping effect, but it is questionable to use them directly as the intrinsic diffusivities in the diffusion equations.

As reviewed in Chapter 2, the migration of hydrogen species H_{BC}^{+}, by taking a pathway of BC $\rightarrow$ BC, has an activation energy of 0.48 eV even at low temperatures as shown by reorientation kinetics after stress-alignment [84], therefore, it can be assumed that the high temperature VWW expression is valid down to room temperatures. Indeed, the extrapolated diffusivities were used as given parameters and different trapping schemes were attempted in Ref. [146], [147], and [161]. The same approach will be used in the calculations thereafter.

Isothermal hydrogenation with atomic H at low temperature and short time (e.g. ~150°C, < 1h) in heavily doped silicon (e.g. $>10^{18}$ boron/cm^3) can be viewed as trap-limited diffusion. Experimental measurement revealed an $\sim t^{1/2}$ dependence of the

penetration depth [60], [162] for hydrogenation time below 30 min, which is coincident with the complementary error function. Ref. [146] used a constant bulk trap density and a lower constant surface concentration C_s as the boundary condition, i.e., $\sim 10^{14}$ cm^{-3}, but detrapping was disregarded in the model. Mathiot [145] proposed a time-independent empirical Gaussian shape trap profile ($[T]_{tot} = [T]_0 \times \exp[-x^2 / L^2]$) in his model. A good fit was obtained with $[T]_0 \approx 10^{19}$ cm^{-3}, $L \approx 0.06$ μm and a capture radius $R_c \approx 5$ A. However, for their particular profiles, the influence of the surface trapping was negligible. Remote plasma or etch-back of damaged surfaces can be used to single out the diffusion problem. Although that is a useful idea, plasma-induced trap (PIT) present in practical processes need to be considered. As illustrated under comparable conditions, experimental data [162] clearly showed that surface high concentration region propagated into the bulk as a function of time. This suggested a process induced trap generation, which could not be explained by surface contamination of H since deuterium was used. A constant bulk trap can generate only partial fitting to the profiles [146]. In some cases, multiple trapping of H at impurity sites was used to describe the diffusion profiles; however, it gave plausible fittings in Ref. [150].

In next section, a simplified model describing trap-limited diffusion will be derived. The formulation will include only combination and dissociation of H at trap sites, and charge state conversion will be excluded. Depth-dependent trap density distribution is necessary to describe diffusion profiles in plasma-related processes.

3.3.2 Formulation of Trap-Limited Diffusion

In low temperature hydrogenation, H was believed to interact with impurities and defects during the diffusion such as dopants, crystalline defects, and metallic impurities. The interaction forms a variety of complexes [75], [105], [163], many of which are immobile. Process also induces traps for H. A popular technique is to deposit a SiN/SiO layer using low-temperature plasma enhanced chemical vapor deposition (PECVD) process followed by a forming gas anneal at ~350°C [164] or a short time RTP anneal at ~800°C [165]. During a plasma process, surface damage is induced due to a "sheath" layer on a conductive specimen in plasma ambient [166], across which ions can be accelerated towards wafer surface. Surface H concentration measured in a plasma-treated sample sometimes reach $\sim 10^{21}$ cm^{-3}, which manifests generation of H traps during the process. Other hydrogenation methods such as ion beam techniques using Kaufman or ECR source can also introduce surface damage as well as inject mobile point defects into the bulk. PITs are not undesirable. They may serve as a source of H and may play a critical role in releasing atomic H in subsequent thermal steps.

During the diffusion at low temperatures, atomic H can get trapped and, given the temperature is moderate, can be detrapped from H-containing complexes. The probability of detrapping is strongly temperature-dependant. There are two diffusion-processes happening: one is the intrinsic diffusion in which H diffuses by "touching" interstitial sites. The second process can be H hopping from one trapped site to another. Both mechanisms seem to exist in low temperature diffusion. It is interesting to relate this trapping process to enhanced solubility of H in Si, because at any time instance, there can be an amount of quasi-free H atoms existing in the crystal lattice which contribute to

total diffusing species with a concentration that may exceed the intrinsic solubility. At a surface that has PITs, the measured H concentrations can be far greater than the intrinsic solubility, which sometimes is in the order of 10^{20} cm^{-3}. This indicates the existence of a large amount of traps.

At low temperatures, when the doping level and/or the trap density is high ($>10^{18}$ cm^{-3}), the diffusion of H in silicon is dominated by the interaction with traps. The charge state conversion becomes unimportant and the diffusion model can be greatly simplified. Similar equations have been partially proposed by other authors [146], [161], but a more complete view will be given in the following sections. The nature and distribution of PITs is a strong function of hydrogenation process itself and is, in general, time dependent.

Mathematically, the simplified diffusion equations can be written as:

$$\frac{\partial[H]}{\partial t} = D_H \frac{\partial^2[H]}{\partial x^2} - \frac{\partial[TH]}{\partial t} + G, \tag{3.57}$$

$$\frac{\partial[TH]}{\partial t} = k[H][T] - k'[TH], \tag{3.58}$$

where G is the generation function of free hydrogen in the bulk, applicable to the implantation cases. Also, the following constraining conditions have to be satisfied:

$$[H] + [TH] = [H]_{tot}, \tag{3.59}$$

$$[T] + [TH] = [T]_{tot}, \tag{3.60}$$

where $[H]$ and $[TH]$ are the concentrations of untrapped and trapped H, $[H]_{tot}$ is the total H concentration, and $[T]_{tot}$ is the total trap density. k' is the dissociation frequency and k is the association rate. The association rate can be expressed in terms of the effective capture cross radius, R_c, as:

$$k = 4\pi R_c D_H \,. \tag{3.61}$$

These equations need to solve under boundary conditions imposed by the hydrogenation process. The boundary conditions (B.C.) used for the simulation are depicted as follows:

$$[H]\Big|_{x=0} = C_s \tag{3.62}$$

for the plasma processes, and

$$-D_H \frac{\partial [H]}{\partial x}\Big|_{x=0} = J_s \tag{3.63}$$

for the implantation processes. Usually, the sample is thicker than the penetration depth of H. The following B.C. at $x = x_c$ was adopted, where x_c is the cutoff depth.

$$\frac{\partial [H]}{\partial x}\Big|_{x=x_c} = 0 \tag{3.64}$$

3.3.3 Numerical Solution – Finite Difference Scheme

Simpler numerical scheme can be applied to trap-limited diffusion model. By substituting rate Eq. (3.58) into diffusion Eq. (3.57), the following equation is obtained:

$$\frac{\partial [H]}{\partial t} = D_H \frac{\partial^2 [H]}{\partial x^2} - \{k[H]([T]_{tot} - [TH]) - k'[TH]\} + G \tag{3.65}$$

By using the convenient variables in Eq. (3.52), Eq. (3.65) becomes

$$\frac{\partial c}{\partial T} = \frac{\partial^2 c}{\partial X^2} - \kappa c + \left(r'_{HT} + g\right), \tag{3.66}$$

where

$$\kappa = \gamma\left(n_T - c_{TH}\right),\ r'_{TH} = \lambda c_{TH}\,,\ g = \frac{G}{C_0},$$

and

$$\gamma = 4\pi R_c l^2 C_0,\ \lambda = k_{TH}^{'} \frac{l^2}{D},\ X = \frac{x}{l},\ T = \frac{Dt}{l^2},\ c = \frac{C}{C_0},\ c_{TH} = \frac{C_{TH}}{C_0} \tag{3.67}$$

and Eq. (3.58) becomes

$$\frac{\partial c_{TH}}{\partial T} = \kappa c - \lambda c_{TH}. \tag{3.68}$$

Since there is only one coupling between Eqs. (3.66) and (3.68), they may be discretized in the implicit form and solved by direct method all at once for each time stepping. We can replace the term $\frac{\partial^2 c}{\partial X^2}$ by the mean of its finite-difference representation on the *j*th and (*j*+*1*)th time steps and approximate the Eq. (3.66) by

$$\frac{c_i^{(j+1)} - c_i^{(j)}}{\delta T} = \frac{1}{2h_{\min}^2}\left\{\left(\alpha_i^- c_{i-1}^{(j)} + \alpha_i^0 c_i^{(j)} + \alpha_i^+ c_{i-1}^{(j)}\right) + \left(\alpha_i^- c_{i-1}^{(j+1)} + \alpha_i^0 c_i^{(j)} + \alpha_i^+ c_{i-1}^{(j+1)}\right)\right\}$$

$$-\kappa\left(c_i^{(j)} + c_i^{(j+1)}\right) + \left(r_{TH,i}^{'(j)} + g_i^{(j+1/2)}\right), \tag{3.69}$$

where coefficients, α_i^-, α_i^0, and α_i^+ correspond to the coefficients, a, b, and c of the middle difference expression in Table 3.2, multiplied by $h_{\min}^2$. By adjusting terms, Eq. (3.69) reduces to

$$\varpi_i^- c_{i-1}^{(j+1)} + \varpi_i^0 c_i^{(j+1)} + \varpi_i^+ c_{i+1}^{(j+1)} = f_i^{(j)}, \tag{3.70}$$

where

$$\varpi_i^- = -r\alpha_i^-,\ \varpi_i^0 = -r\alpha_i^- + 2 + 2\kappa,\ \varpi_i^+ = -r\alpha_i^+,$$

$$f_i^{(j+1)} = r\alpha_i^- c_{i-1}^{(j)} + \left(r\alpha_i^0 + 2 - 2\kappa\right)c_i^{(j)} + r\alpha_i^+ c_{i+1}^{(j)} + 2r_{TH,i}^{'(j)} + 2g_i^{(j+1/2)}. \tag{3.71}$$

By using forward or backward difference, the boundary condition (3.62), (3.63), and (3.64) can be discretized. Together with Eq. (3.71), they form a complete set of linear

equations, which can be solved by Gaussian elimination method. After $c_i^{(j+1)}$'s are solved from (3.71), they are substituted into Eq. (3.68) and the $c_{TH,i}^{(j+1)}$'s are updated.

3.3.4 Simulation and Discussion

In this section, the above model is used in the simulations. Figure 3.3 shows deuterium profiles (dotted data) of plasma-processed, n-type, FZ silicon wafers of different dopant concentrations [167]. Deuteration was conducted at 200 °C. The dopant types are identified in the figure.

If this is an ideal case, the experimental data can be fitted into complementary error functions. The solid lines in Figure 3.3 show the results of the best fits. The extracted parameters are conveniently displayed in the figure for each dopant type. They, in common, indicate a very high surface concentration and a very low diffusivity.

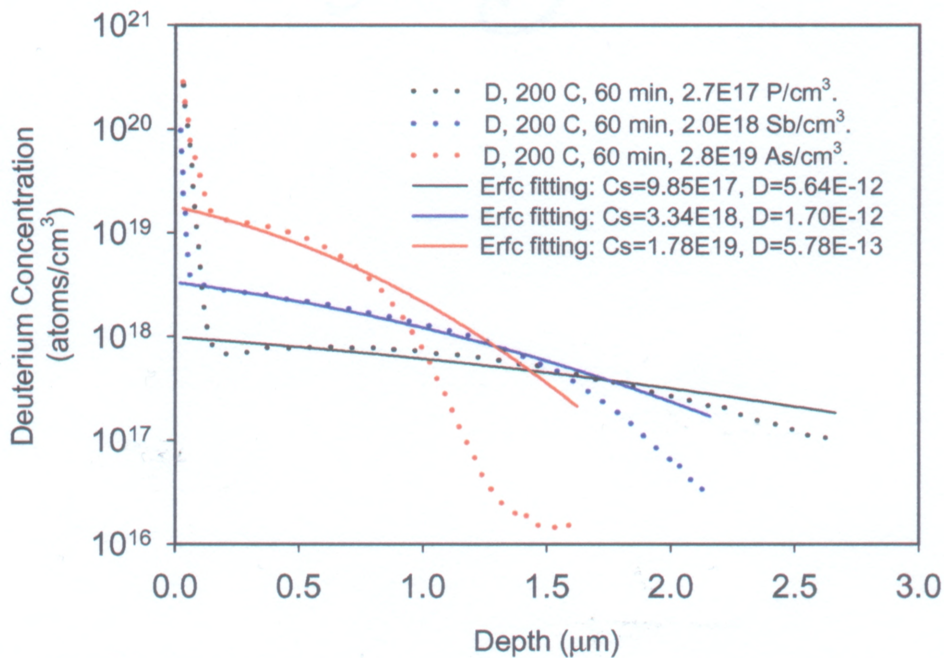

Figure 3.3 Experimental deuterium profiles (dotted lines) of a plasma-deuterated, n-type Si, at 200 °C, fitted with erfc.

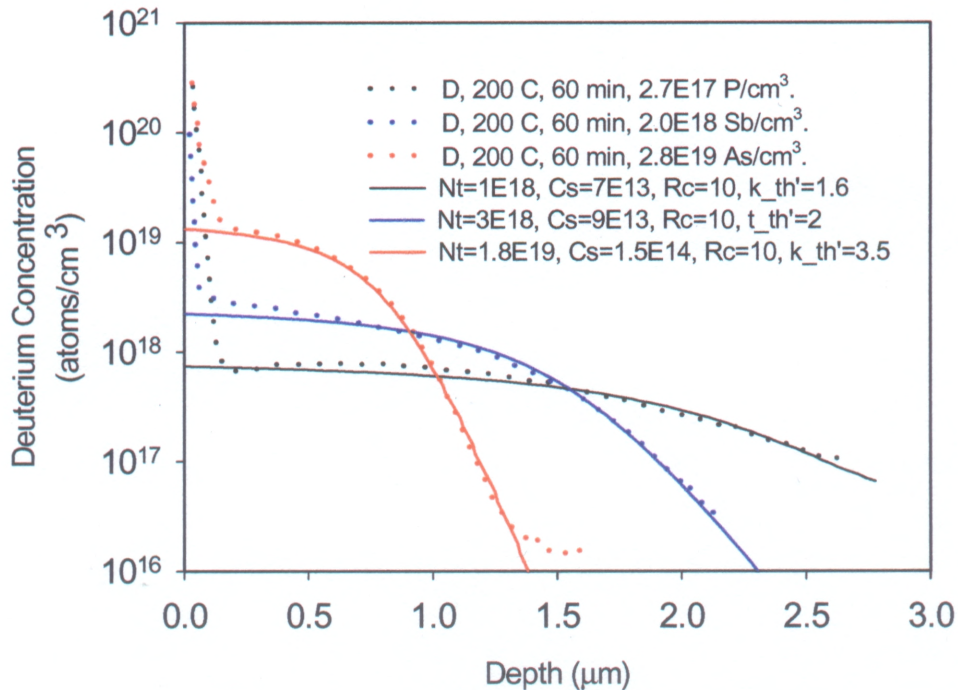

Figure 3.4 Experimental deuterium profiles (dotted lines) of a plasma-deuterated, n-type Si, at 200 °C, fitted with the current model.

Next, the same set of data is fitted by assuming a uniform bulk trap density. Solid lines in Figure 3.4 are the best-fit profiles. The corresponding parameters (R_c, k', and C_s) for the best-fits are also shown in the figure. By using uniform trap density distributions between $10^{13} - 10^{14}$ cm^{-3}, an excellent agreement is seen between theoretical calculations and the experimental profiles. The fitted surface concentration of untrapped hydrogen, C_s, is approximately four orders of magnitude lower than the previous result, while diffusivity used was extrapolated from high temperature VWW data. This clearly demonstrates that the presence of bulk traps can greatly reduce the effective diffusivity of H (or D). A uniform trap density distribution alone, however, cannot generate a fit to the near-surface profile.

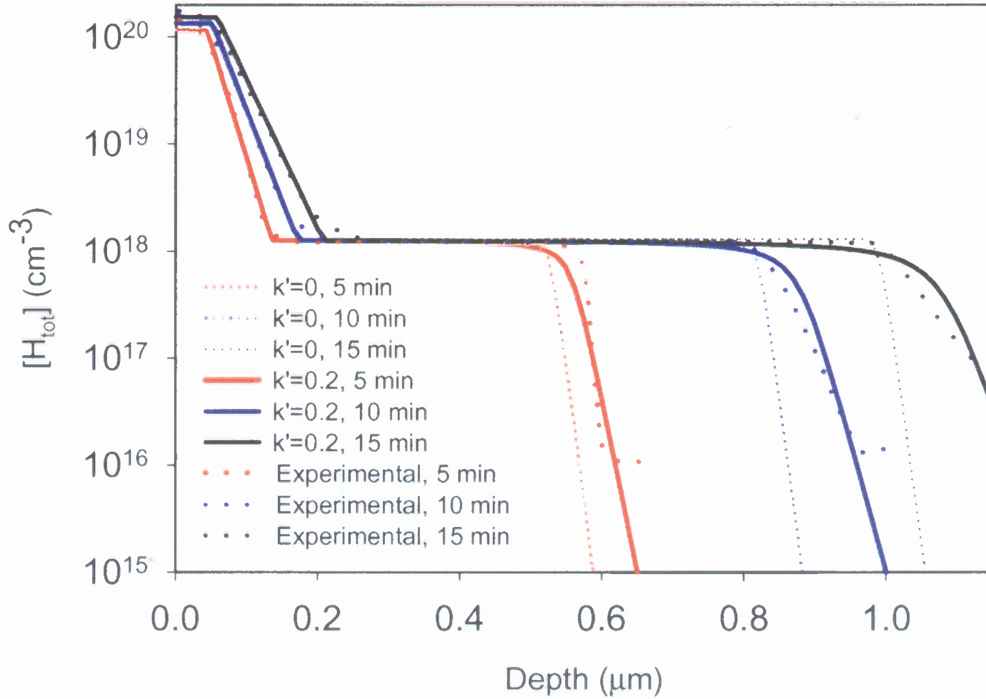

Figure 3.5 Experimental data of Ref. [162] (dotted lines) and fitted with $R_c = 10$ A, $C_s = 2.75 \times 10^{14}$ cm^{-3}, $T = 200°$C, 15 min, B doping = 1.3×10^{18} cm^{-3}.

In some hydrogenation processes, the influence of process-induced traps cannot be neglected, such as the experimental data taken from Ref. [162]. Kalejs et al used another set of data to examine the influence of bulk traps [146], which is dopant level dependent. Here, the time dependent set is used. Figure 3.5 shows the experimental deuterium profiles of a B-doped (1.3×10^{18} cm^{-3}) sample for plasma-processed at 200°C for three different times (5, 10, and 15 minutes). In this simulation, the trap density profile consists of a surface component and a constant bulk component. For the plasma hydrogenation, the process-induced trap distribution is expected to be exponential with a time-independent surface concentration. The total trap distribution can be expressed as:

$$[T_{tot}] = T_0 e^{-\frac{x}{a+bt}} + T_b, \tag{3.72}$$

where the first time-dependent term is due to process damage and T_b is a constant bulk trap level. The best fits are obtained with $T_0 = 10^{21}$ cm^{-3}, $a = 0.1$ μm, $b = 0.108$ μm, and $T_b = 1.3 \times 10^{18}$ cm^{-3}. The results are shown in Figure 3.5, where the solid lines are the fitted data. The best-fits are obtained by assuming the dissociation frequency, $k' = 0.2$. It should be noted that same parameters give excellent fit for experimental profiles for different time lengths.

In the next example, the SIMS profiles of low-energy implanted samples will be considered. Figure 3.6 shows a measured deuterium profile (thick, dotted line) of a FZ sample, implanted at 250°C at approximately 1.5 KeV, for 30 min. The data may be trial-fitted with various values of the flux density and a distribution function of:

$$[T_{tot}] = [T_0] \cdot \frac{t}{T} \cdot \exp\left(-\frac{(x - x_p)^2}{2\Delta x_p^2} \right) + [T_b]\,, \tag{3.73}$$

where $[T_0] = 4.454 \times 10^{20}$ cm^{-3}, $T = 1800$ s, $x_p = 0.0367$ μm, $\Delta x_p = 0.028$ μm, $[T_b] = 1.2 \times 10^{17}$ cm^{-3}.

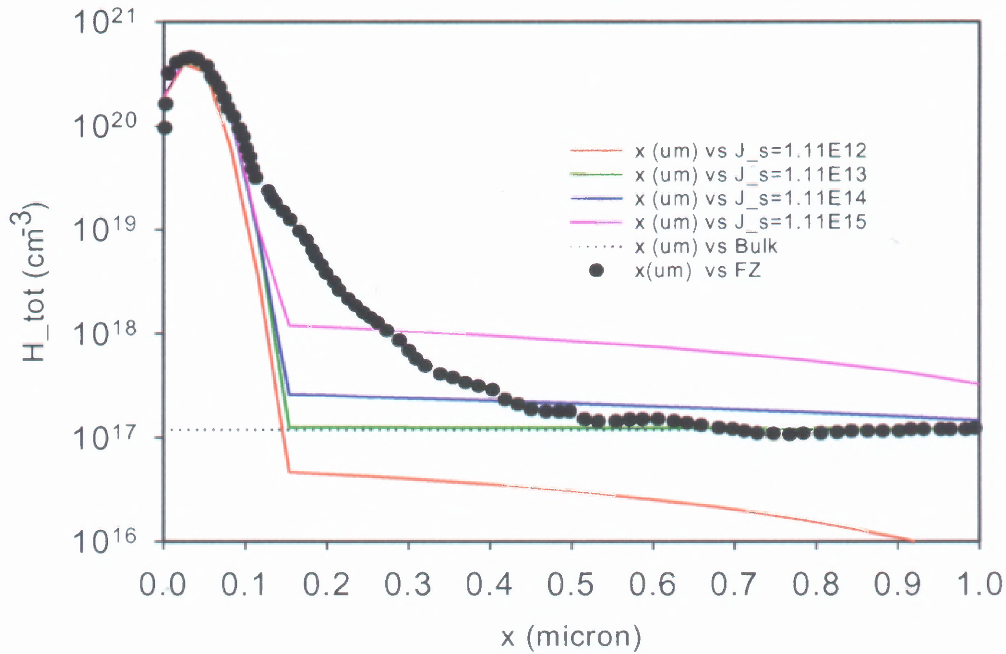

Figure 3.6 Experimental and calculated profiles: deuterium was implanted at 1.5 KeV, at 250°C for 30 min. Parameters used were $Nt_b = 1.2 \times 10^{17}$ cm^{-3}, $k_th' = 0.1$ s^{-1}.

These calculations are performed for different values of deuterium flux – ranging from 1.1×10^{12} to 1.1×10^{15} cm^{-2}/s. It is interesting to note that the near-surface distribution of D does not change with flux (as expected). However, there is a strong dependence of bulk distribution on the flux density, and it is difficult to fit the entire profile under the assumption of immobile traps.

In these three sections, a trap-limited hydrogen diffusion model is derived as a limiting version of the "complete" diffusion model. This model includes simultaneous trapping and detrapping mechanisms at both bulk and process-induced traps. Simulations yield excellent fits to the experimental profiles. In most cases, it is sufficient to assume immobile traps. Situations, however, are encountered where it is necessary to include mobile traps.

3.4 Mobile Traps in Hydrogen Diffusion

As mentioned in the previous section, immobile trap alone is not sufficient to explain the diffusion profiles and material dependent apparent diffusivities observed in ion beam hydrogenation experiments for PV silicon materials. This section will introduce a more complex model that takes into account the generation, diffusion of mobile traps and their interaction with free moving hydrogen species. Indeed, one candidate of such mobile traps is vacancy, as reviewed in the last section of Chapter 2. Point defect complex such as H-vacancies may also be mobile [40], [133] and may contribute to the H transport.

3.4.1 Formulation of the Limiting Case

Hydrogenation by ion beam techniques is usually performed at relatively low temperatures, i.e., 100 – 300°C, and the samples in research usually have bulk dopant / trap level of $>10^{17}$ cm^{-3}. As a result, the diffusion is in a regime controlled by traps. Charge states conversion does not seem important in such cases and can be neglected in the model.

There are possibly three types of diffuser here, free hydrogen species, H, mobile-trap-hydrogen complexes, VH, and mobile traps, V. The governing equations are

$$\frac{\partial[H]}{\partial t} = D_H \nabla^2 [H] - \frac{\partial[TH]}{\partial t} - \left(\frac{\partial[VH]}{\partial t}\right)^*, \tag{3.74}$$

$$\frac{\partial[VH]}{\partial t} = D_{VH} \nabla^2 [VH] + \left(\frac{\partial[VH]}{\partial t}\right)^*, \tag{3.75}$$

$$\frac{\partial[V]}{\partial t} = D_V \nabla^2 [V] - \left(\frac{\partial[VH]}{\partial t}\right)^* + G_v, \tag{3.76}$$

where G_v is the generation function of mobile traps. The related rate equations are shown as follows,

$$\frac{\partial[TH]}{\partial t} = k_{TH}[T][H] - k_{TH}^{'}[TH], \tag{3.77}$$

$$\left(\frac{\partial[VH]}{\partial t}\right)^* = k_{VH}[V][H] - k_{VH}^{'}[VH], \tag{3.78}$$

Similar constraining conditions must be satisfied:

$$[H] \geq 0,\ [TH] \leq [T]_{tot},\ [T]+[HT]=[T]_{tot},\ [VH] \geq 0,\ [V] \geq 0, \tag{3.79}$$

3.4.2 Experimental Observations

The experimental data of special interest are the diffusion profiles of deuterium previously obtained by using ion beam techniques, which were reviewed in Section 2.7.3.1. The vacancy and vacancy-related mechanism were proposed to explain the difference in profiles, and the vacancy concentration was thought to be higher at material grown with a high pulling rate. Lower oxygen level and/or higher carbon level may favor the vacancy formation.

In order to determine if vacancy really plays a role in the process, positron annihilation spectroscopy (PAS) analysis was performed on hydrogen implanted samples. The samples were prepared on EFG ribbon material. Deuterium implantation was conducted on Varian 350D, with ion beam with energy of 40 KeV and dose of 10^{15} cm^{-2}. The samples were kept at room temperature during the deuteration. The projected range of the implantation is about 500-nm deep in the bulk. The preliminary PAS data are

shown in Figure 3.7, where the positron beam was tuned to different implantation energy and gave a depth resolution. The qualitative open volume density was estimated from the S parameter. The lowest curve is the single crystal defect free silicon reference. The middle two curves are ribbon sample reference, which showed a similar shape as the FZ sample with a slight higher open volume density. For H-implanted ribbon sample, the vacancy-type defect has a high concentration and formed a peak about 250-nm deep.

In conclusion, PAS data does show vacancy level is higher in EFG ribbon samples than in the reference FZ samples. It is clear that deuterium implantation is inducing vacancy and vacancy clusters in the sample. However, the peak position of vacancy-related open volume density is shallower than the peak position of implanted deuterium profile.

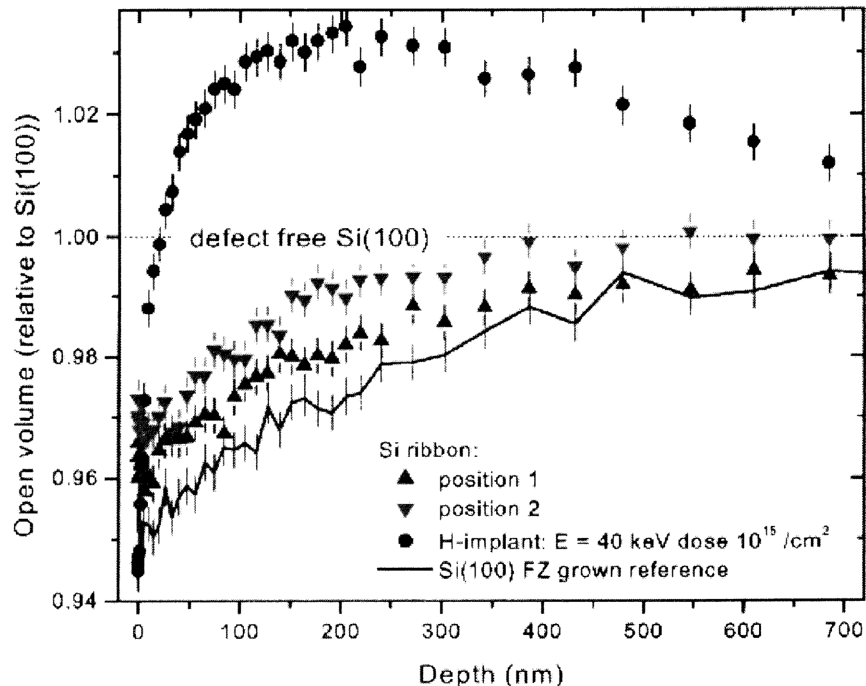

Figure 3.7 PAS depth profiles on Si-ribbon at two locations on the sample, a H-implanted Si ribbon and for comparison FZ grown defect free silicon with a native oxide on the surface.

3.4.3 Discussion

It would be instructive if profiles in Fig. 2.6 can be fitted, however, there are too many unknown parameters, such as diffusivity of mobile trap and mobile-trap-hydrogen complex. Furthermore, the nature of the mobile and its generation during the implantation process are not clear. Nevertheless, from several test runs, it is certain that the free hydrogen species level is lower than 10^{16} cm^{-3} by using ion flow at sample surface, J_s = 1.75 × 10^{12} cm^{-2}s^{-1}, derived from the ion current and the processing time. The atomic hydrogen at 250°C is very mobile, with a diffusivity about 2.3 × 10^{-7} cm^{2}s^{-1}. During the time period of 30 min, atomic hydrogen moves fast enough to migrate and tie up with any "forgotten" traps within 1-micron from the surface. The seemingly diffusion profile of "hydrogen" may actually be the diffusion profile of traps that are decorated by hydrogen.

From the observation, the total trap concentration can be described by the following expression:

$$[T]_{tot} = \frac{\Phi r_T}{\sqrt{2\pi}\Delta R_p} \exp\left(-\frac{(x - R_p)^2}{2\Delta R_p^2} \right) + \frac{\Phi r_V}{\sqrt{\pi(2\Delta R_p^2 + 4Dt)}} \exp\left(-\frac{(x - R_p)^2}{2\Delta R_p^2 + 4Dt} \right) + [T_b], \quad (3.80)$$

Where Φ is the total trap injection dose. r_T and r_V are the fraction of total dose for generating immobile traps and mobile traps, respectively. Rp is the projected range of the implantation peak, and ΔR_p is its standard deviation or projected straggle. The first term is to describe a fixed trap. The second term borrowed the expression that is normally used to describe the redistribution of an implanted Gaussian shape profile, where D is the diffusivity of the mobile implanted species. This term could be related to the mobile traps involved in enhanced hydrogen diffusion. $[T_b]$ is the background bulk trap density.

By fitting the main portion of the curves, the best fitted dose of total trap generation, Φ, and diffusivity of mobile traps, D_V, are summarized in Table 3.3. All the curves share the same Rp and ΔR_p, i.e., Rp = 0.0367 μm, and ΔR_p = 0.0282 μm. Surprisingly, from the curve fitting, the dose fraction of fixed and mobile traps, r_T and r_V, were the same for all curves, i.e., $r_T = 0.69$ and $r_V = 0.31$. This indicates something is in common in trap generation process regardless of material type.

Table 3.3 Dose of total trap injection and diffusivity of mobile traps.

Type	LCR	EFG	CAST	FZ	CZ
Φ (cm^{-2})	4.54×10^{15}	4.38×10^{15}	4.19×10^{15}	3.75×10^{15}	3.53×10^{15}
D_V (cm^{2}s^{-1})	1.1×10^{-13}	1.1×10^{-13}	8.3×10^{-14}	1.4×10^{-14}	2.8×10^{-15}

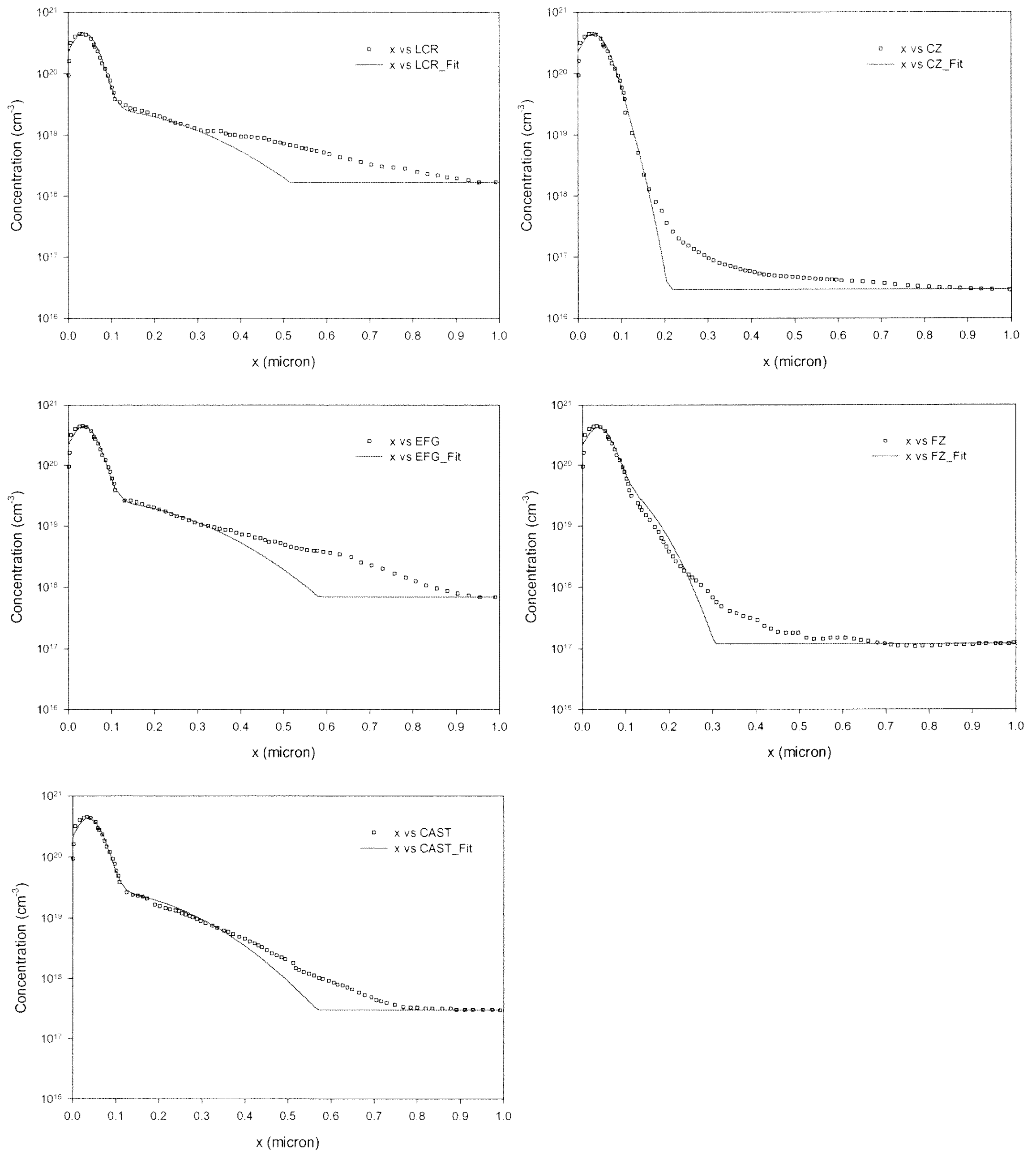

Figure 3.8 Hydrogen diffusion profiles fitted with fixed + mobile trap distribution.

It is not clear why the diffusivities fitted for mobile traps are small and are different for different materials. Perhaps there is an unknown type of interaction between the mobile traps, V, and "traps" for mobile traps, X, in the background. The trapping and detrapping behavior is in the sense of immobilizing and re-mobilizing the V's. The trapping coefficient is k_{XV} and detrapping rate is k'_{XV} for the reaction:

$$V + X \underset{k'_{XV}}{\overset{k_{XV}}{\leftrightarrow}} XV \tag{3.81}$$

If there is a large concentration of X and equilibrium among V, X, and XV is reached, there will be a relation:

$$k_{XV}[X][V] = k'_{XV}[XV]. \tag{3.82}$$

Since $[V]+[XV]=[V]_{tot}$, $[V]$ is related to $[V]_{tot}$ by the relation

$$[V] = (1+\eta)[V]_{tot}, \tag{3.83}$$

where $\eta = \frac{k_{XV}}{k'_{XV}}[X]$. Eq. (3.83) can be differentiated, yielding with the diffusion equation

of V's, $\frac{\partial [V]_{tot}}{\partial t} = D_V \nabla^2 [V]$, a diffusion equation in terms of [V],

$$\frac{\partial [V]}{\partial t} = D_{V,eff} \nabla^2 [V], \tag{3.84}$$

but with an effective diffusivity

$$D_{V,eff} = \frac{1}{1+\eta} D_V \approx \frac{k'_{XV}}{k_{XV}} \frac{D_V}{[X]}. \tag{3.85}$$

From Eq. (3.85), it may be postulated that LCR material may have less such immobilization mechanism for mobile traps than CZ material, meaning a smaller $[X]$, k_{XV}, and/or a larger k'_{XV}.

3.5 Hydrogen Diffusion in p-n Junction

The building blocks of solar cell structures are p-n junctions. By attaching metal electrodes grids on both sides of a junction, a one-junction solar cell is formed. Modern solar cells employ a host of enhancement features for excessive carrier generation and retention. Multiple-junction cells take advantage of absorption and light generation at multiple spectrum ranges in order to increase the open circuit voltage and energy conversion efficiency. As mentioned in Chapter 1, gettering and hydrogen passivation are two important approaches to reduce the bulk recombination. For example, hydrogenation during PECVD nitride deposition was shown [37] to increase the lifetime on this by 20% and Cai et al. [39] illustrated that indeed hydrogen was responsible for the passivation in such process. In contrast with MOS devices that require interface passivation only, the hydrogenation in solar cells requires passivation within the entire thickness of the device and the surface. Such a process leads to a reduction in the dark current and an increase in the photocurrent and internal spectral response, especially at long wavelength region, which corresponds to an improved bulk minority recombination lifetime. Hydrogenation has become a very important process step. Various hydrogenation processes are being used in nearly all-commercial Si solar cells fabrication lines, but knowledge is lacking regarding how hydrogen diffuses in a junction.

Some experimental data is available but majority of the parameter space is not yet explored. The penetration of hydrogen from a plasma source into a substrate of p-type silicon is greatly reduced if the substrate is covered by a thin layer of strongly n - type material [168]. Given a high concentration of donors at n^+ side of the material, it may be qualitatively explained that the initial diffusion is limited by trapping of hydrogen at

dopant sites at n^+-type side. Thus the penetration of hydrogen into p-type side becomes prominent only when most traps at n^+-type side are filled by free moving hydrogen. Subsequent studies have shown that hydrogen diffusion across p-n junction depends on many parameters – temperature, doping profile, processing time, etc. A quantitative analysis is difficult and tedious due to the uncertainty of various parameters and the fact that the population of charged hydrogen species needs to be solved together with self-regulated junction field and traps if any. This section will briefly show some typical diffusion profiles at junctions and then discuss some important parameters. Subsequently, a simulation of diffusion at junction will be given by using the method and algorithm described early in this chapter.

Figure 3.9 shows profiles [169] of total deuterium concentration after deuteration of samples prepared by implanting a high concentration of phosphorus into moderately doped p-type silicon substrate, with a subsequent high-temperature anneal to remove implantation damage. Deuteration was from downstream gases from a plasma discharge. The different curves correspond to different times of deuteration at 150 °C. Figure 3.10 shows hydrogen diffusion for 2 hours across n-atop-p junctions at 300 °C. The substrates were heavily doped and then epitaxial layers with different doping concentration were grown.

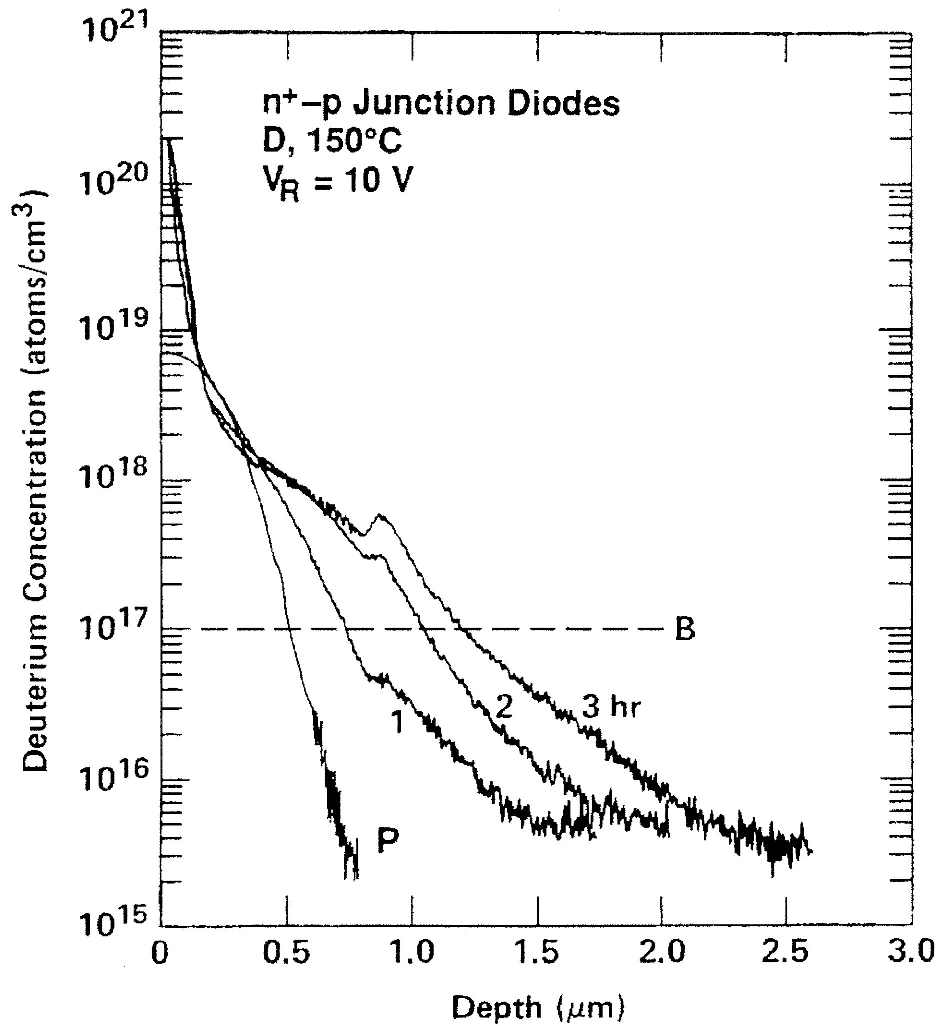

Figure 3.9 SIMS profile of total deuterium density across p-n junctions formed by implanting phosphorus into a (100) silicon wafer uniformly doped with 10^{17} boron per cm^3 for various times of deuteration at 150 °C. Deuteration was from downstream gases from a plasma discharge.

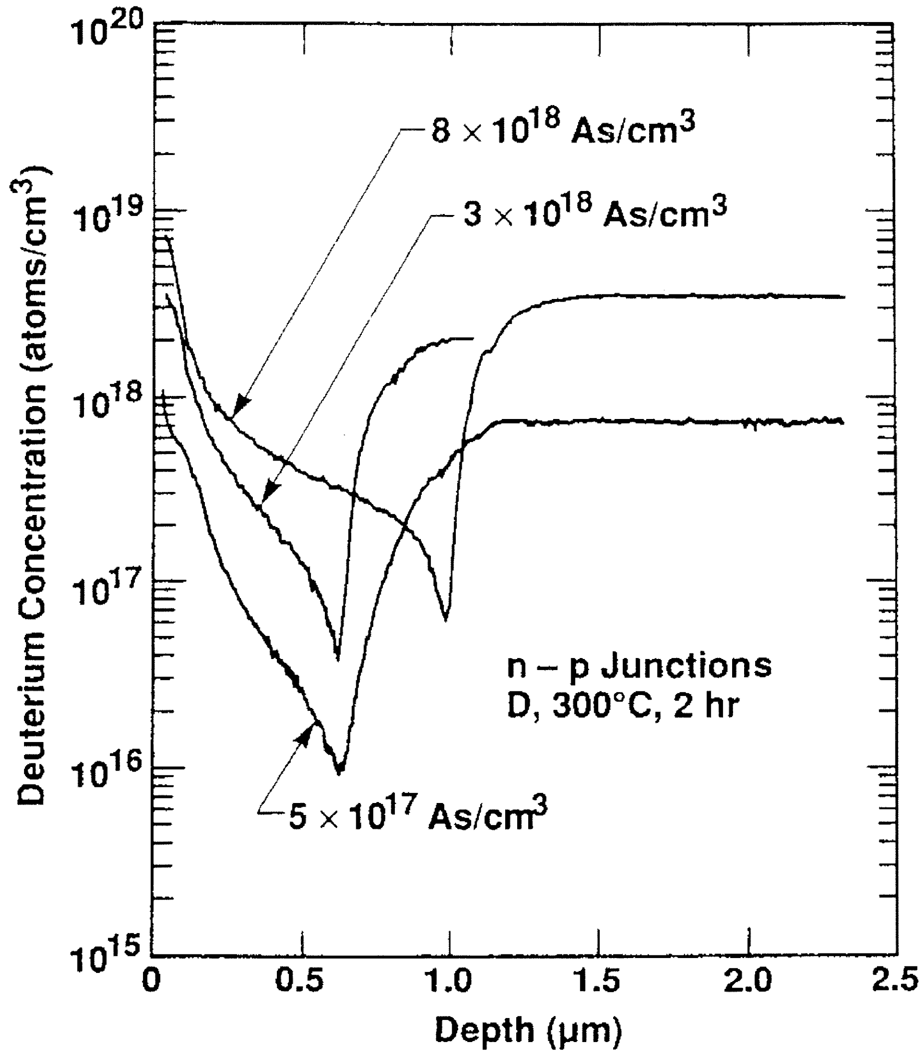

Figure 3.10 SIMS profile of total deuterium density in three composite samples subjected to 2-hour deuteration in the downstream product from a hydrogen plasma discharge at 300 °C. All samples had a substrate containing 8×10^{18} B/cm^3, which was covered with epitaxial layers containing 8×10^{18}, 3×10^{18}, 5×10^{17} As/cm^3, respectively, to form n-p junctions.

Figure 3.9 and Figure 3.10 show the features of 150°C diffusion and 300°C diffusion respectively. From Figure 3.9, it is obvious that the diffusion of hydrogen in the n^+-p junction region is very slow, mostly due to the addition of heavily doped n^+ region. At this temperature, the recombination rate of positively-charged donors and negative-charged hydrogen species is large due to heavy doping. As obtained from solving Poisson's equation of the doping profiles, the depletion region of an unprocessed junction is located between 0.44 and 0.70-μm, with a maximum field peak located at 0.54-μm. From the total hydrogen concentration profile, there seems to have a consistent accumulation of hydrogen at about 0.90-μm. If the built-in field is inducing the drift of charged species and causing this accumulation, the depletion region edge corresponding to processed junction is located roughly between 0.80.to 1.00-μm. It appears that the trapping of hydrogen at the junction widens the depletion region and shifts its edge into the bulk.

In the previous discussion of trap-limited diffusion, the surface concentration of atomic hydrogen was fitted with $\sim 2.75 \times 10^{14}$ cm^{-3}. It is necessary to verify the order of magnitude of this value and see if it is a typical boundary condition for other plasma processes. In Figure 3.10, 300°C hydrogenation for 2 hours seems to reach a point of steady state. The total concentration of hydrogen in p-substrate beyond 1.0-μm is flat. Since doping concentration of the substrate is also high, i.e., 8×10^{18} B/cm^3, there should be an equilibrium of combination and thermal dissociation among charged hydrogen species, available acceptor sites, and acceptor-hydrogen complexes. The detailed-balance equation can be written as follows:

$$k_{BH}\left([B]_{tot}-[BH]\right)[H]=k'_{BH}[BH]. \tag{3.86}$$

Then, the free hydrogen concentration is

$$[H]=\frac{k'_{BH}}{k_{BH}}\frac{1}{\left(\frac{[B]_{tot}}{[BH]}-1\right)}. \tag{3.87}$$

Total boron concentration was known, and the level of flat region in the bulk corresponds to the concentration of boron-hydrogen complex pairs. We can substitute into equation (3.87) the Coulombic capture radius at 300°C, ~ 25 A, and dissociation rate, k'_{BH}, ~ 1.56 × 10^{18} s^{-1}, which is derived from the Arrhenius relation of B-H complex previously reviewed in Chapter 2. The concentration levels of atomic hydrogen in the flat region were calculated to be 5.2 × 10^{14}, 2.9 × 10^{14}, and 0.8 × 10^{14} cm^{-3}, for the junctions covered with epitaxial layers of doping concentration 8 × 10^{18}, 3 × 10^{18}, and 5 × 10^{17} cm^{-3}, respectively. The order of magnitude of those values matches the surface atomic hydrogen concentration, C_s, extracted from curve fitting in the previous sections.

Next, a simulation at n^+-p and p^+-n junction with a similar doping profile as in Figure 3.9 is discussed. Traps other than dopants are excluded so that the simulation addresses the main issues. The full code was run on the Sun Ultra80 workstation at NREL, which supports 4 UltraSPARC-II microprocessors working at 450 MHz with 4MB cache memory each. Due to the computation resource available, the simulation was done for an early stage of the diffusion. However, some important features were observed.

Figure 3.11 shows the simulation result of hydrogen diffusion at n^+-p junction for the time duration of 0.04-s. The doping profiles are combined in the figure and hydrogen species of different charge states and complexes are illustrated with distinctive colors.

Figure 3.12, Figure 3.13, and Figure 3.14 show the diffusion at n^+-p junction for 0.4-s, at p+-n junction for 0.04-s, and at p+-n junction for 0.4-s, respectively. Initially, a constant level (2.9×10^{14} cm^{-3}) of atomic hydrogen is assumed for surface as well as for bulk As the diffusion proceeds, the diffusion and redistribution of various species were seen.

Shortly after the process is initiated, P-H and B-H complexes started to form at both n and p side. However, B-H pair formation at n-type or n^+-type region is negligible because most hydrogen atoms there are of negative charge. They are repulsive to the negative charged boron cores. The dominant atomic hydrogen species at n or n^+ region of a junction is negatively charged, whereas p^- or p^+ region is dominated by position charged ions. In the depletion region, the built-in electric field, ~ 10^4 V/cm, causes the accumulation of H^- (H^+) ion at the n^+ (p^+) region of an n^+-p (p^+-n) junction, which can retard the diffusion. Neutral atomic hydrogen has a low concentration at either side of the junction compared to charged hydrogen ions. The concentrations of both B-H and P-H are maintaining a very high level compared to atomic hydrogen species, and the diffusion is in the trap-limited diffusion regime due to sizable level of doping in both sides of the junction.

It is usually assumed that dopant-hydrogen complex formation is negligible above 200°C and the field structure of a junction does not change much. From the above simulation, however, it was observed that the electric field actually changes from the surface. It is perceivable that this change will extend to the bulk as the diffusion time goes longer. This change will modify the electrical potential throughout the junction, which in turn will be affecting the diffusion process itself.

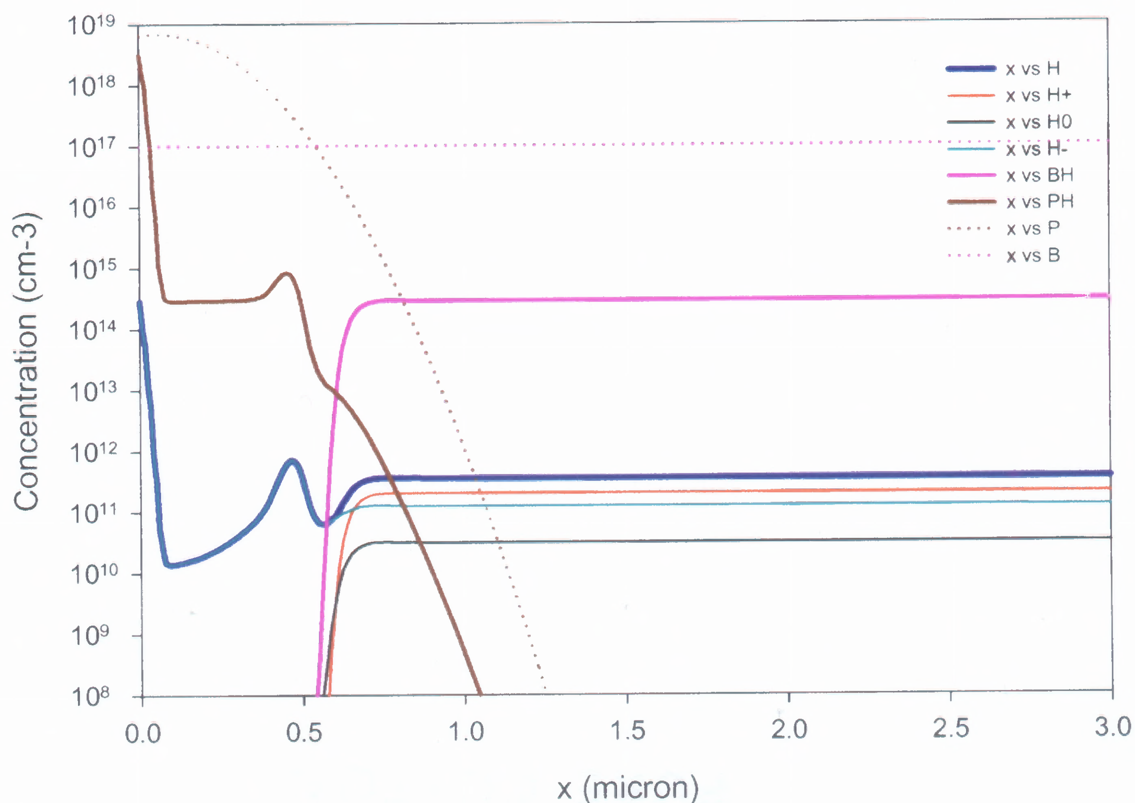

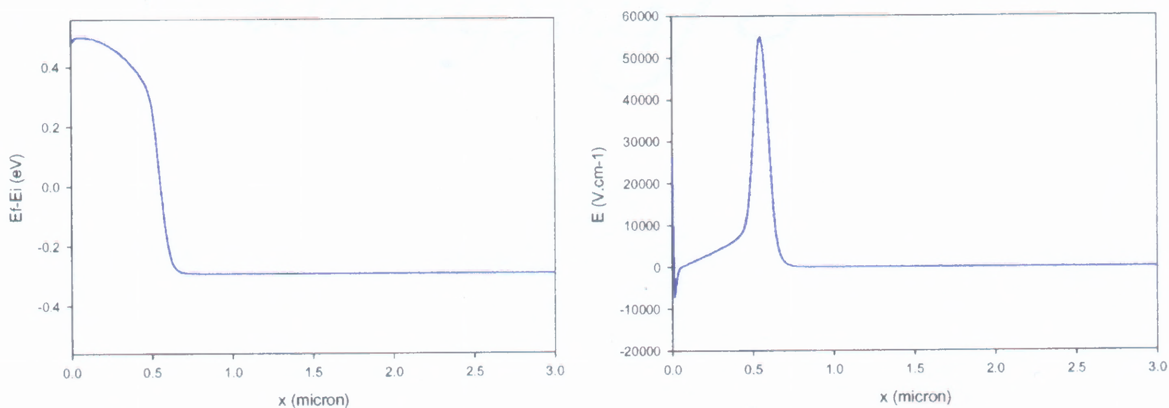

Figure 3.11 Simulation of H diffusion in an n^+-p junction with the parameters: T = 300°C, $(E_d - E_i) = 0.36$ eV, $(E_i - E_a) = -0.20$ eV, $D_0 = 5.82 \times 10^{-7}$, $D_+ = 5.82 \times 10^{-7}$, $D_- = 2.91 \times 10^{-7}$, cm^2s^{-1}, $k_{DH}' = 3.54 \times 10^3\ s^{-1}$, $k_{AH}' = 1.56 \times 10^3\ s^{-1}$, **t = 0.04 s**. Dotted curves are the dopant profiles.

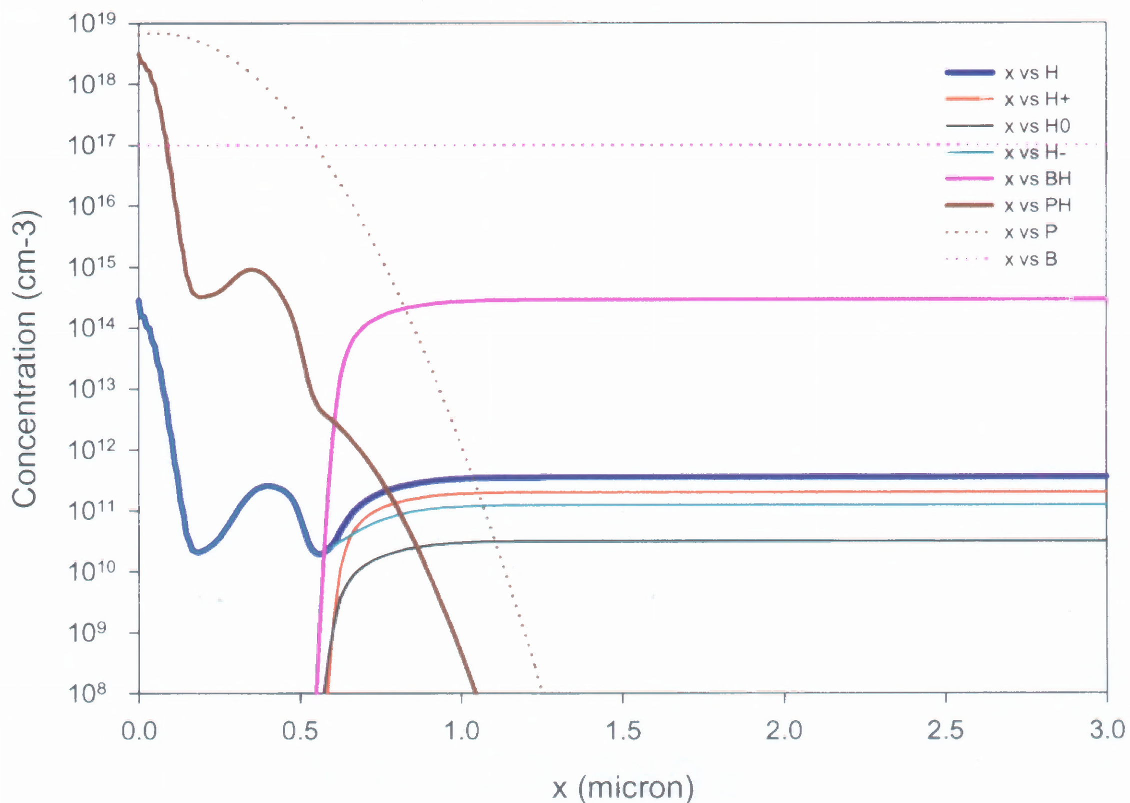

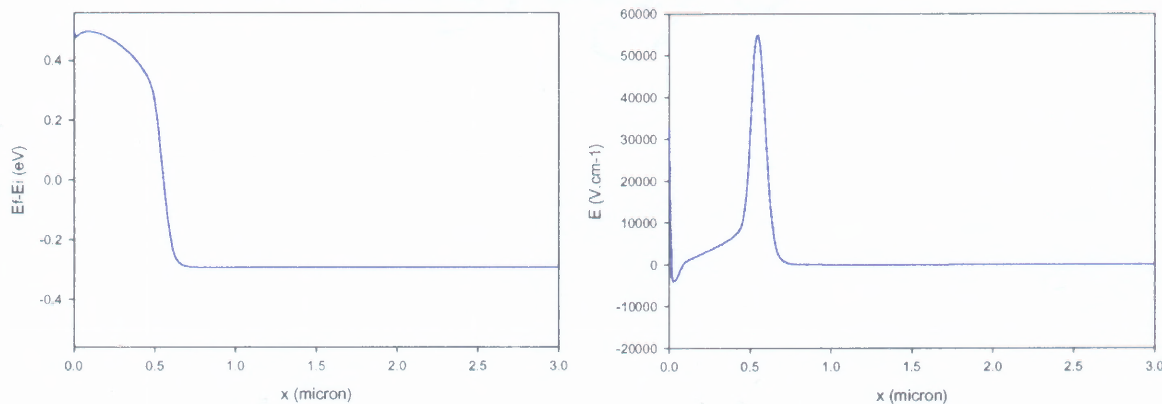

Figure 3.12 Simulation of H diffusion in an n^+-p junction with the parameters: T = 300°C, $(E_d - E_i) = 0.36$ eV, $(E_i - E_a) = -0.20$ eV, $D_0 = 5.82 \times 10^{-7}$, $D_+ = 5.82 \times 10^{-7}$, $D_- = 2.91 \times 10^{-7}$, cm^2s^{-1}, $k_{DH}' = 3.54 \times 10^3\ s^{-1}$, $k_{AH}' = 1.56 \times 10^3\ s^{-1}$, **t = 0.4 s**. Dotted curves are the dopant profiles.

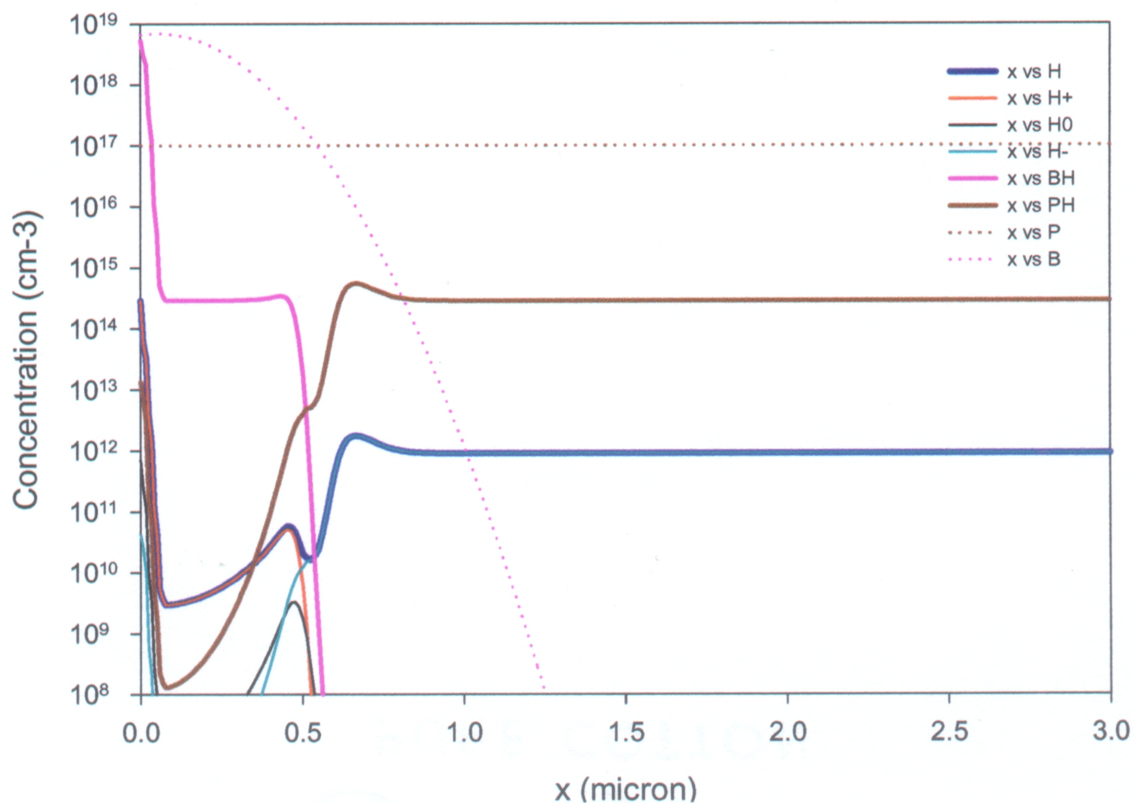

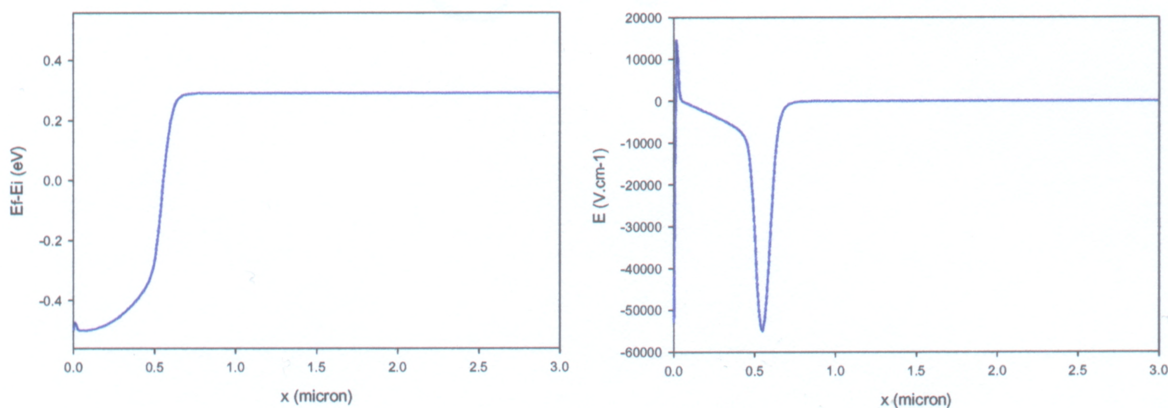

Figure 3.13 Simulation of H diffusion in a p+-n junction with the parameters: T = 300°C, $(E_d - E_i) = 0.36$ eV, $(E_i - E_a) = -0.20$ eV, $D_0 = 5.82 \times 10^{-7}$, $D_+ = 5.82 \times 10^{-7}$, $D_- = 2.91 \times 10^{-7}$, cm^2s^{-1}, $k_{DH}' = 3.54 \times 10^3\ s^{-1}$, $k_{AH}' = 1.56 \times 10^3\ s^{-1}$, **t = 0.04 s**. Dotted curves are the dopant profiles.

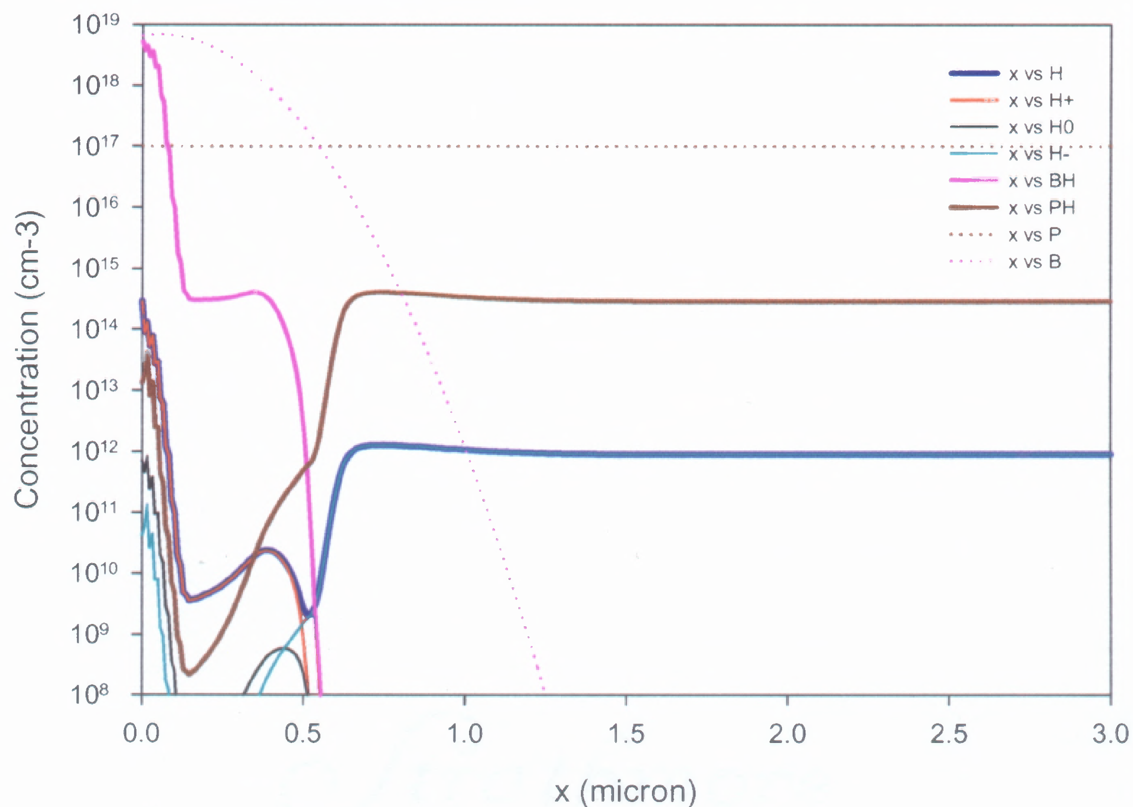

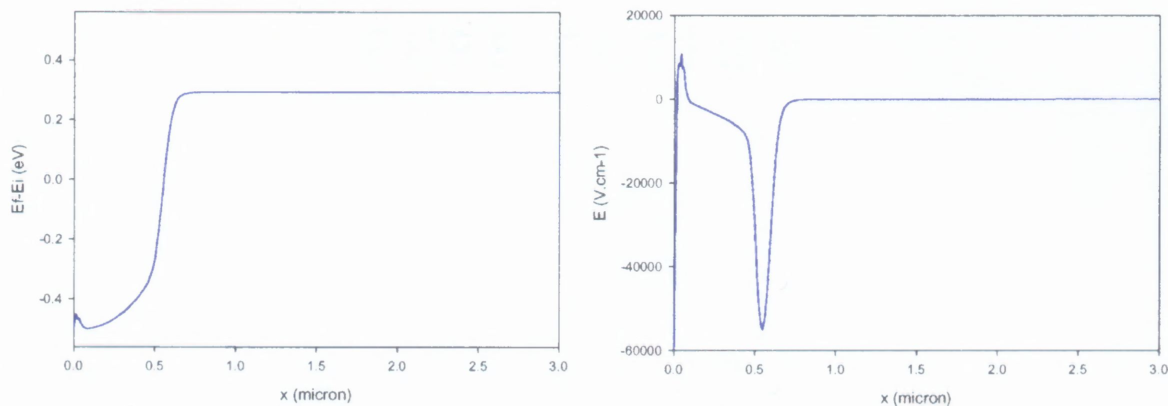

Figure 3.14 Simulation of H diffusion in a p+-n junction with the parameters: T = 300°C, $(E_d - E_i) = 0.36$ eV, $(E_i - E_a) = -0.20$ eV, $D_0 = 5.82 \times 10^{-7}$, $D_+ = 5.82 \times 10^{-7}$, $D_- = 2.91 \times 10^{-7}$, cm^2s^{-1}, $k_{DH}' = 3.54 \times 10^3\ s^{-1}$, $k_{AH}' = 1.56 \times 10^3\ s^{-1}$, **t = 0.4 s**. Dotted curves are the dopant profiles.

CHAPTER 4

UNDERSTANDING HYDROGENATION PROCESSES

4.1 Forming Gas Anneal Passivation

Hydrogen passivation by forming gas anneal (FGA) was briefly introduced in Section 2.2.5. In this section, some previous observations will be interpreted by using the modeling results discussed in Chapter 3.

This group did extensive studies in the past [170] and showed that surface damage is strongly correlated with the dissociation H_2. Figure 4.1 shows how the degree of surface damage can influence the hydrogen diffusion profile after FGA treatment. The material used was as-grown laser recrystallized ribbon (LRC) samples damaged with grit sizes of 0.2, 0.1, 0.05, and 0.01 μm respectively. After the respective mechanical grit polish was applied for 20 minutes, the samples were treated with D_2 FGA at 400°C for 1-hour.

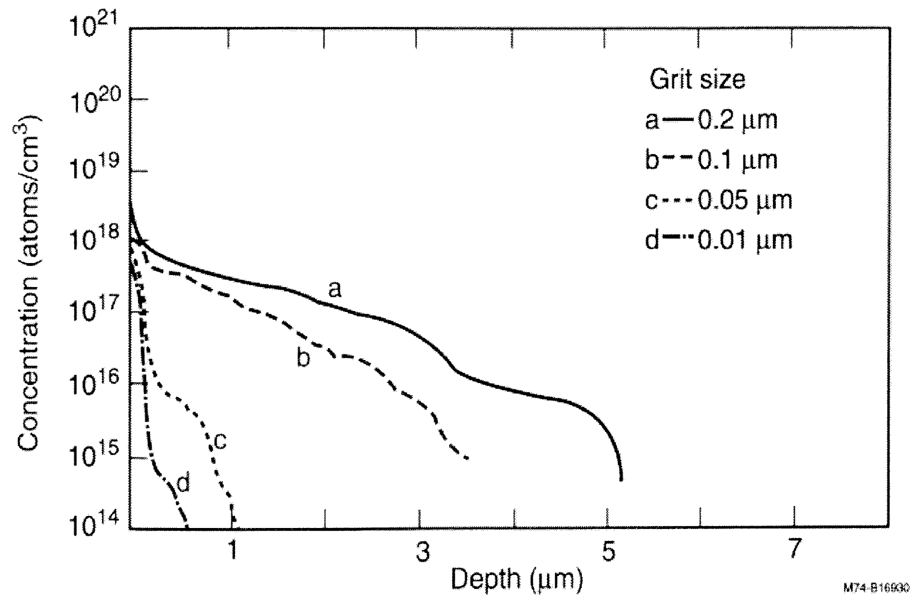

Figure 4.1 SIMS deuterium profiles of an LRC ribbon treated with a forming gas anneal. Surface damage was created by a grit size of 0.2, 0.1, 0.05, and 0.01 μm, respectively.

Obviously, hydrogen diffuses deeper in the samples with damage produced by larger size grits. Damage-induced stress at surface was characterized by both XTEM and XRD analysis. Local contrast at damage sites was observed in XTEM picture.

To investigate the effect of surface damage caused by heavy doping on the hydrogen diffusion, several n^+-p junctions prepared by ASE Americas were applied with D_2 FGA at 400°C for 1 hour and then analyzed with SIMS spectroscopy [170]. The SMIS D profiles are shown in Figure 4.2. D was seen confined at the surface without diffusing into the bulk. Similar surface damage-induced stress, however, was detected by XRD analysis at n^+ side of the n^+-p junctions.

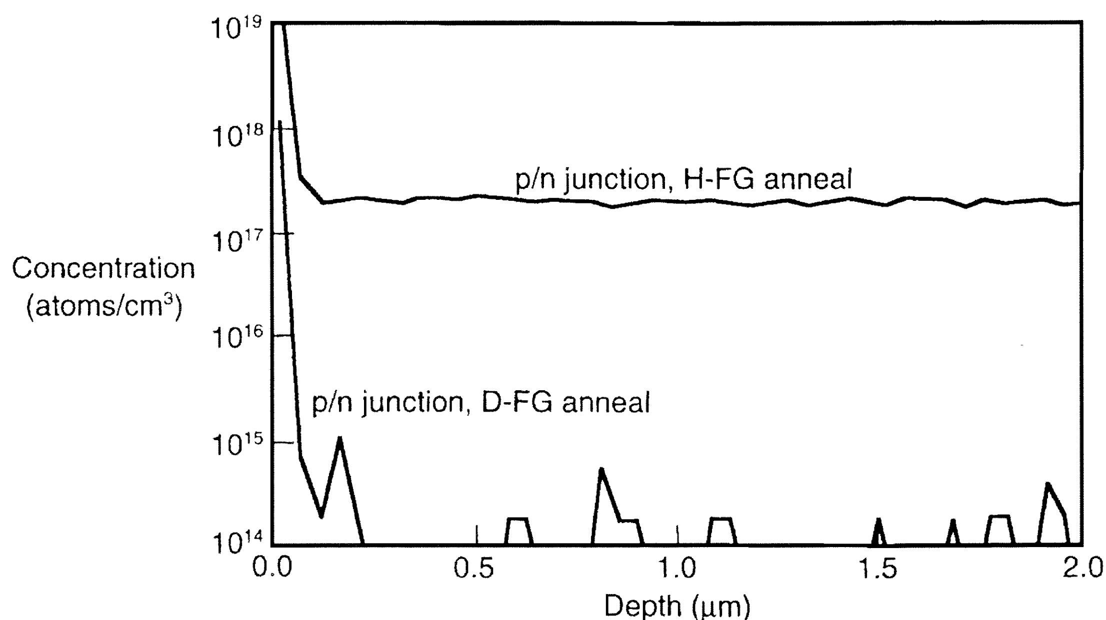

Figure 4.2 SIMS H/D profiles of an n^+-p junction treated in FGA at 400°C for 1 hour.

This led to the study of an n^+-p junction sample from ASE Americas with a 0.03 μm grit polish applied to the n^+-side with a cotton swab followed by FGA at 400°C for 1

hour. A minimal amount of grit and pressure were applied for 3 minutes, because the n^+ layer is only 0.3 – 0.4 μm in depth. Interestingly, SIMS D profiles showed a deep D diffusion in a damaged junction (Figure 4.3). No diffusion was observed on the unpolished junction sample.

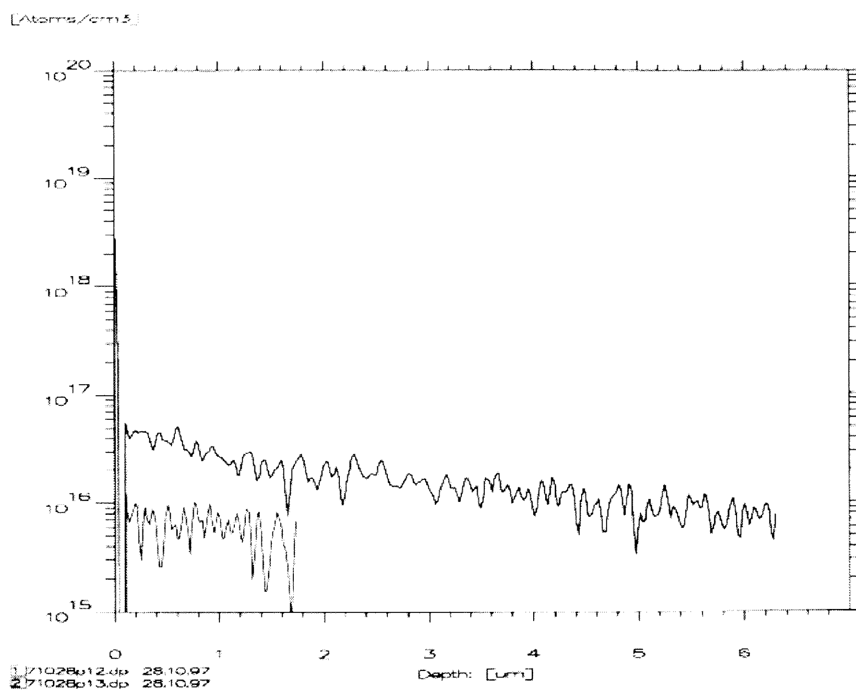

Figure 4.3 ASE Americas substrate of p/n junction with 0.03-μm grit followed by a D_2 FGA at 400°C for 1 hour.

A model was proposed to explain the hydrogen diffusion in FGA by H_2 dissociation and the participation of mobile products, H^+ and {H-V} [170]. No attempt, however, was made to explain why H is not observed in as-made n^+-p junction in FGA process. It should be pointed out that passivation may be observed in solar cells after FGA treatment [171] even though H was not detected by SIMS due to its limitations.

Following the discussion in Section 3.5, hydrogen diffusion in p-n junction at low temperatures, e.g., 300 ~ 400°C on a heavily doped n^+ region is actually trap-limited. Even though atomic hydrogen can be generated at surface by H_2 reduction reaction with vacancies, its concentration, C_s, can be one or two orders of magnitude lower than that of plasma process. Furthermore, at n^+ region, the dominant atomic hydrogen species is H^-, which has a smaller mobility than that of H^+ species due to its larger ion radius. As a result, the hydrogen diffusion from FGA ambient in n^+-p junction is very limited. The same argument can be applied to the case of the surface of n^+-p which was polished for 3 minutes. Since the n^+ region is very thin, i.e., only 0.3 – 0.4 μm in depth, polishing the sample surface may actually remove a portion of n^+ layer. Therefore, thickness of n^+ layer and the total amount of surface traps were reduced. Atomic hydrogen species was then able to contribute more to the diffusion in the base region.

The disadvantage of FGA for solar cell passivation is that the amount of atomic hydrogen is small compared to the plasma or ion beam method. FGA relies on the availability of vacancy-type point defects at the surface to dissociate H_2 into atomic hydrogen. As point defects convert to hydrogen-containing complexes, they need to be "regenerated" at the damaged surface. Low process temperature in FGA method favors complex formation and thus limits the in-diffusion of hydrogen species. A typical minority carrier diffusion length is about 50 μm in base region, so hydrogen diffusion as deep as 50-μm is needed to prominently improve the cell efficiency.

4.2 Ion Beam Passivation by Kaufman Source

Compared to forming gas anneal passivation, ion beam sources readily provide a large amount of free hydrogen atoms at the sample surface. Kaufman ion source beam has been practically used to in solar cell passivation studies. Hydrogen from Kaufman ion source was reported to passivate both shallow impurities [172] and deep level defects [55]. The effect of hydrogen in those reports was monitored by spreading resistance and capacitance techniques. Improvement of photoresponse of Si-based solar cells was measured using electron-beam-induced-current (EBIC) techniques [54], which further demonstrated the passivation of recombination-active deep levels. Some of those studies have included silicon material grown by web, ribbon, and EFG techniques, which are now routinely used in solar cell industry. A typical process is done with about 1 – 1.5 KeV ion beam and the sample is usually heated at 200 – 300°C [173]. Modeling results in Chapter 3 showed that this technique could achieve deep hydrogen diffusion and also that mobile traps may be involved. However, the diffusivity values extracted from the diffusion profiles disagreed with the assumption that mobile traps were simply vacancies. Although they are vacancy-related, as shown by PAS analysis, their nature is not clear.

With the sample being heated at 200 – 300°C, hydrogen-induced defects were observed at near surface region after hydrogenation by Kaufman ion source. Those defects include hydrogen platelet, hydrogen segregation and even bubbles. The growth of hydrogen platelets is in connection with temperature-related nucleation. It was shown that in n-type FZ Si (100) sample, platelets grow markedly faster at high temperatures if a low temperature (~150°C) step is added before the high temperature anneal [174]. PV silicon materials usually contain a large amount of crystalline defects and impurities,

which serve well as nucleation centers. Cross-sectional TEM (XTEM) analysis was performed on the surface of Si specimens processed by a 1.5-KeV implant at 250°C, where such defects were present [175]. Figure 4.5 (a) and (b) are XTEM pictures which show the segregation of hydrogen at dislocation loop and along grain boundary. It can be seen that hydrogen-decorated grain boundary shows less defects as it goes deeper into the bulk. It is likely that bulk diffusion is as fast as the diffusion along grain boundaries; otherwise, the defect formation could have retarded the diffusion path along the grain boundaries and formed an abrupt pattern in the XTEM image.

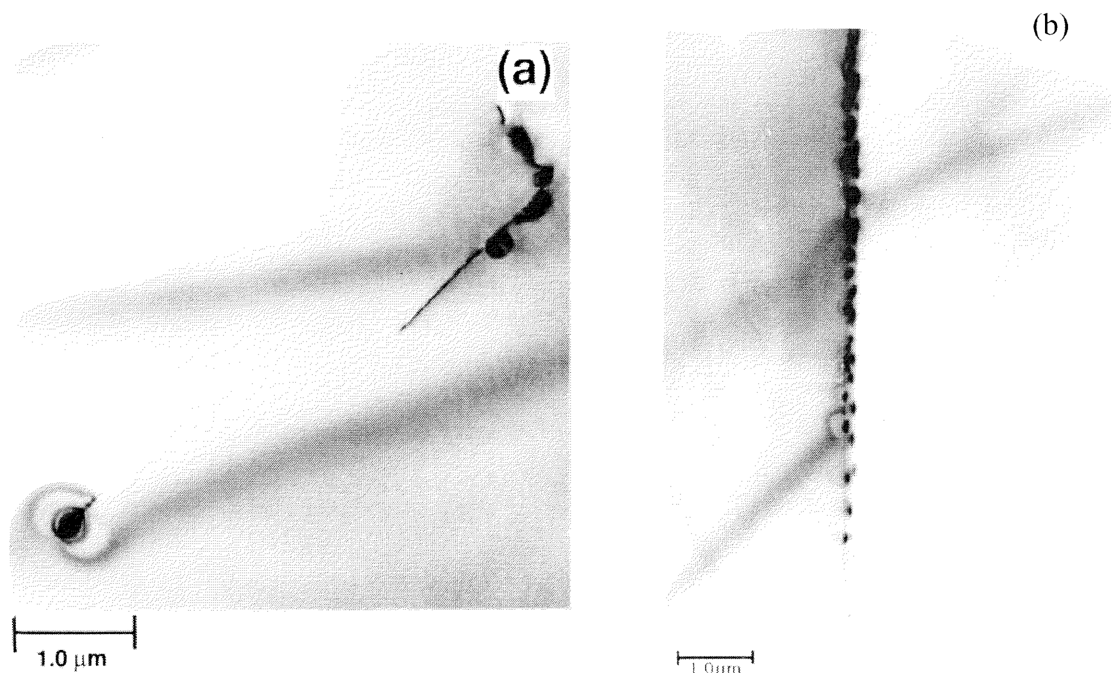

Figure 4.4 XTEM photos of hydrogenated Si samples, showing segregation of H at the dislocations (a) and along a grain boundary (b).

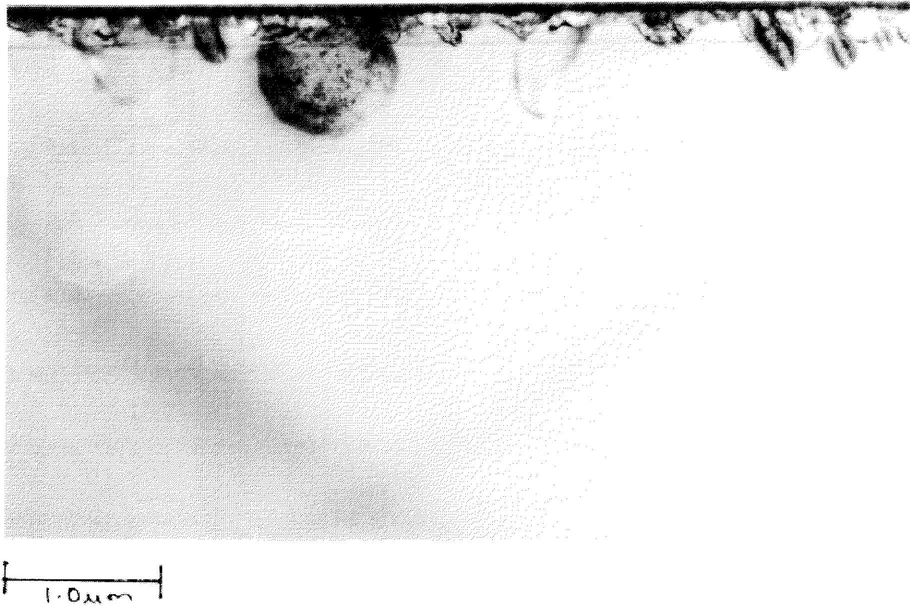

Figure 4.5 XTEM photo showing defects generated near the surface by a 1.5 KeV H-implantation.

When large dose of hydrogen is implanted in a heated sample, segregation can lead to formation of "bubbles" and platelets. Figure 4.5 shows the formation of hydrogen bubbles near the surface. Platelets are disc-like micro-defects that lie along {111} planes and are elongated along [110] directions. XTEM pictures of platelets are shown in Figure 4.6. Figure 4.6 (a) shows a series of platelets, identified by arrows, generated at the surface of a hydrogenated Si sample. Figure 4.6 (b) is a higher-magnification picture showing one tilted platelet. It is seen that such a defect has a core-like structure. The core of the platelet is believed to consist of vacancy clusters that may have trapped molecular hydrogen [123], [176].

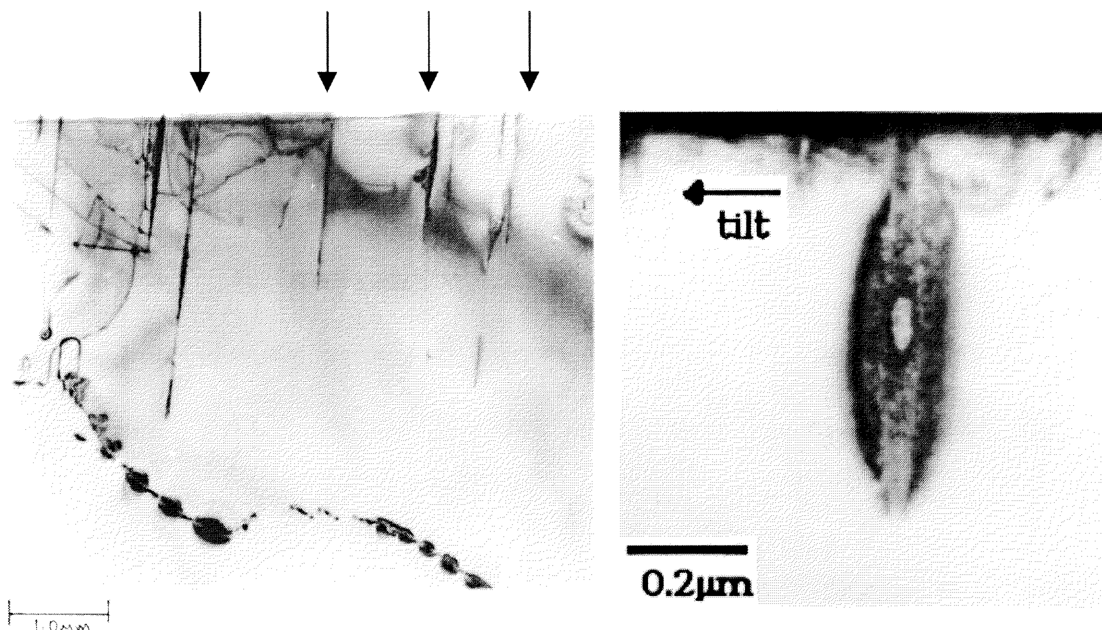

Figure 4.6 XTEM photos showing (a) series of platelets in edge-on position and (b) tilted configuration.

Hydrogen segregation at defect sites and the formation of hydrogen-induced extended defects greatly affect the diffusion profile near the sample surface. A large amount of hydrogen can be involved at such defect sites, and the total concentration of hydrogen observed by SIMS can be as high as 10^{20} cm^{-3}. The defects formed by hydrogen segregation can be detrimental to the devices [177].

To circumvent the difficulty of front side hydrogenation by Kaufman source, a compromise was proposed [173], [178] to process a solar cell from the backside before the back contact formation. After the aluminum layer is deposited at the backside, an RTP-type of process elevate the sample temperature to 300 – 400°C, hoping the vacancy injection, if any, could help enhance the diffusion by forming hydrogen-containing

species of vacancy-hydrogen pairs. Figure 4.7 illustrates the various steps of the backside hydrogenation scheme using Kaufman ion source.

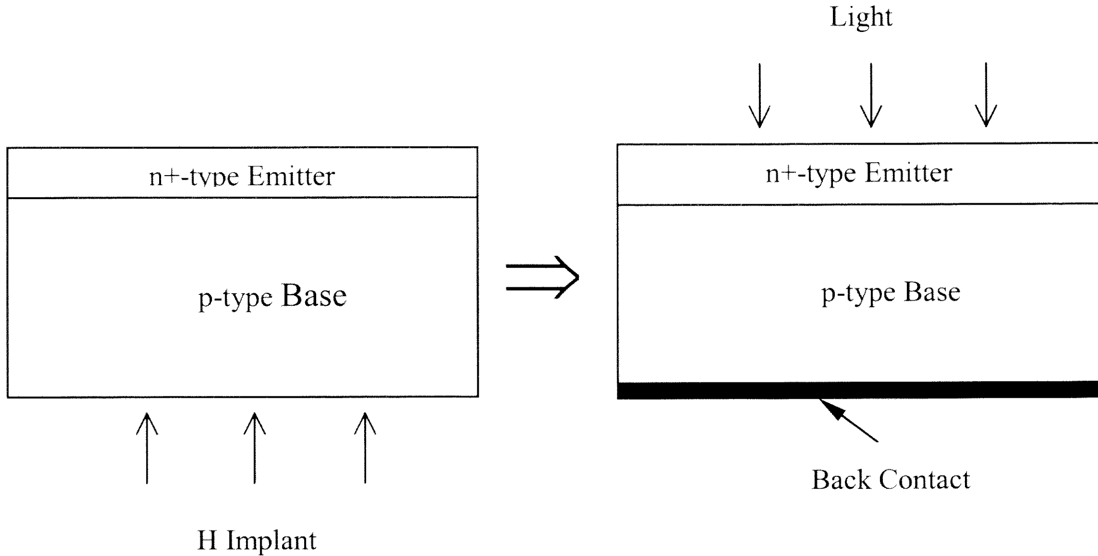

Figure 4.7 Steps used in backside hydrogenation by using Kaufman ion source and RTP.

Backside hydrogenation did show some success. A reduction in dark current was observed, which proved that some amount of hydrogen had reached at least to a distance of minority carrier diffusion length away from the junction depletion edge. The idea of diffusing hydrogen from the backside is a great step forward, but the current procedure is still hoping that low-temperature mechanisms such as vacancy-hydrogen complex formation would give a hand to the diffusion. Since the aluminum layer is used, the Al-Si eutectic temperature (577°C) restricts the maximum value of subsequent processing temperatures. In fact, even as processing temperature approaches 400°C, (not a high temperature yet), Al spikes into silicon, and, hence a stringent process control is needed.

4.3 PECVD - RTP passivation

Until recently, hydrogenation of solar cells was done as a separate solar cell fabrication step using either low-energy ion implantation or hydrogen plasma. Plasma-enhanced chemical vapour deposition (PECVD) silicon nitride (SiN) has emerged as a promising passivation technique as a hydrogen-rich Si_3N_4 antireflection coating (ARC) layer is deposited. Different vendor optimizes their hydrogenation process empirically. Interestingly, it was found that if different PECVD processes were optimized, they end up with a very close improvement on a given quality of material [179]. So far, understanding of the mechanisms is lacking.

It has been generally assumed that atomic hydrogen is released in subsequent RTP-type thermal cycle and diffuses into the silicon bulk. This explanation does not consider H diffusion into Si during the nitridation itself and cannot tell how various process parameters interact with each other. In this section, through quantitative modeling, it is revealed for the first time how hydrogen is introduced in PECVD step and how it diffuses in the subsequent RTP step.

It is a common experience that process temperature and time, required for optimizing H passivation, is much higher than expected on the basis of diffusivity of H in Si. It is now known that this behavior is a direct result of H trapping by dopants, crystal defects, dangling bonds, point defects, and process-induced traps (PITs). PECVD process enjoys the advantages of fast deposition rate. It uses a rf-induced glow discharge to transfer energy into the reactant gas, allowing the substrate to remain at a lower temperature than in APCVD or LPCVD process. Typical reactants used for depositing Si_3N_4 are Si-bearing gas like, silane (SiH_4) or trichlorosilane, and ammonia (NH_3) or

nitrogen (N_2). The deposition is typically done at about 300°-400°C for about 10 minutes. The deposited films, in general, are not stoichiometric because the deposition reactions are quite diverse and complicated. PECVD Si_3N_4 films usually contain an appreciable amount of hydrogen in the form of chemical bonds, Si-H and N-H. Although this film is rich in hydrogen, the amount of hydrogen trapped at sample surface is usually overlooked. After the deposition, the cell is treated in an RTP-like process, typically for a few seconds at ~800°C, which can be part of the contact formation step.

In a PECVD process, the sample surface is exposed to the direct rf-plasma and subjected to energetic ion bombardment. Extensive damage to the sample surface is inevitable. A large amount of process-induced traps (PIT) can be generated near the surface during the process, which trap many of the hydrogen species. Thus, in a low-temperature plasma process, traps serve as "storage" sites for H. The complexes formed are stable at low temperatures. However, at higher temperatures, trap-hydrogen complexes will dissociate, releasing H that can diffuse rapidly in the Si lattice. This concept can be used to explain the diffusion of H accompanying nitridation and RTP anneal. In the following specific case, a PECVD Si_3N_4 film about 900 A thick deposited in 6 minutes is considered. This deposition step introduces a high concentration of hydrogen near the surface which, when processed in a subsequent higher-temperature (~800 °C) RTP anneal, releases free atomic hydrogen and passivate the bulk.

In the low temperature PECVD step, PITs are assumed to be confined near the surface. A typical total trap density may be described by the following expression:

$$[T_{tot}] = T_0 e^{-\frac{x}{a+bt}} + T_b,$$

where the first time-dependent term is due to process damage and T_b is a constant bulk trap level. The fitted parameters from Section 3.3.4 may be borrowed here to describe the trap-limited diffusion in the low-temperature PECVD step. The parameters to be used are $T_0 = 10^{21}$ cm^{-3}, $a = 0.1$ μm, $b = 0.108$ μm, and $T_b = 1.3 \times 10^{18}$ cm^{-3}. Surface concentration of hydrogen supplied from rf-plasma is assumed as 2.75×10^{14} cm^{-3}. Charge state conversion is neglected, because the diffusion is trap-limited due to a high level of T_b.

The second step of the simulation is to perform short-time high temperature diffusion. The dissociation frequency of the trap-hydrogen at 800°C was assumed 2 orders of magnitude higher than at 300°C. The "stored' H is then dissociated from the traps and diffuse into the bulk. The boundaries at surface and at a cutoff depth in the bulk are considered impermeable. Although most of the hydrogen atoms are freed from surface traps, the bulk trap density has a larger influence on the final passivation depth.

Figure 4.8 illustrates the evolution of the total H profile in a PECVD step performed at 300°C for a duration of 6 minutes. The wafer is assumed to have a bulk trap density of 10^{17} cm^{-3}. The figure shows two distinctive portions of a profile: high-density surface area and bulk diffusion area. The inset in Figure 4.8 magnifies the surface portion, where the total H concentration decreases from surface concentration of above 10^{20} cm^{-3} to the bulk level of 10^{17} cm^{-3} at 0.1 μm from the surface. Obviously, the surface diffusion is controlled by PITs. The thickness of it is small, just a few fraction of a micron, but it traps about ~90% of the total hydrogen incorporated. The rest 10% of the hydrogen diffuses into the bulk up to a depth of 11 μm with a concentration equal to that of the bulk trap density.

The diffusion profiles during the second step of the process are shown in Figure 4.9. Those profiles are a series of diffusion snapshots at different time instants up to 10-s. It clearly shows three steps are involved:

1. Shortly after annealing step is initiated, from time 0 – 10^{-3} s, surface portion of trapped hydrogen gets released and diffuses towards the diffusion front set in the first step. There is no change in the bulk profile or diffusion front.
2. From time 10^{-3} – 1 s, the major bulk diffusion is observed. The diffusion front moves from 11-μm to about 35-μm.
3. The last step is from 1 – 10 s, it can be seen that the diffusion front is merely shifted about 5 μm. The dominant mechanism is trapping and detrapping in the vicinity of diffusion front. It is perceivable that as the process goes longer, there will be a much slower movement of the diffusion front compared to step 2. Figure 4.10 shows that the concentration of atomic hydrogen supply is dropping quickly in the diffuse region and that it only increases near the diffusion front but the level is about 2 orders of magnitude lower than C_s.

Another set of simulation was run for a similar case except the bulk level is lower, i.e., 10^{16} cm^{-3}. Figure 4.12 shows the PECVD step, where the diffusion front is at 35-μm, which is deeper than the previous case. The anneal simulation in Figure 4.13 shows a similar diffusion step except the third step is not seen. The reason is that the concentration of atomic hydrogen is decreasing but is always above the bulk trap level up to 10 s, until the whole 100-μm material is flooded with atomic hydrogen at a level slightly above the bulk trap level. As a result, the passivation depth is more than 100-μm deep in this specific case.

Some conclusions can be drawn from the above simulation:

- The PECVD step serves as a predeposition step of H. The majority of the hydrogen atoms are trapped and "stored" near the surface. Bulk diffusion was seen but the diffusion depth is strongly controlled by the PIT density profile.
- In the anneal step, H is released from the surface and may be simply redistributed into the bulk region. H may be also released from the chemical bonds in Si_3N_4 film, but it is a less important process compared to the strong release of hydrogen from the surface, which is able to maintain a high level of hydrogen supply during the bulk diffusion in the second step.
- The diffusion depth of H upon annealing is strongly controlled by the bulk trap density. If the bulk trap level is high, the passivation depth will be mostly controlled by the amount of hydrogen that was trapped during the PECVD step. Increasing time duration of the RTP step does not appreciably change the profile formed within a couple of seconds at the beginning of the process.
- If the bulk trap level is low, e.g., 10^{16} cm^{-3}, H diffuses deeply into the substrate and penetrates through the entire wafer. This is in agreement with experimental observations [179]. Still, the level of atomic hydrogen in the RTP step is controlled by the total amount of hydrogen trapped in the PECVD step.
- For samples with high trap levels, once the diffusion front is stalled, increasing anneal time will not make much difference in passivation depth. However, for samples with moderate trap levels, a certain amount of time is required for released hydrogen to diffuse deep.

- It may be interesting to point that in the RTP step, high temperature such as 800°C in many cases may actually anneal out the plasma-induced defects, making H available for passivation as well as decreasing the detrimental effect from the PECVD plasma process.

As mentioned earlier, besides the passivation effect, PECVD Si_3N_4 films may serve as an ARC layer, replacing the conventional double layer AR (DLAR) coating that consists of MgF_2 layer (1060 – 1100 A) on top of ZnS layer (500 – 560 A), [59], [180], [181]. Interestingly, it was shown that by varying the ratio of SiH_4/NH_3 and the flow rate of SiH_4, and/or with the addition of H_2 in the plasma, the refractive index (n) of the film can range from 1.87 to 2.93 [182], [183]. This implies that, by manipulating the process condition, a DLAR layer or even a varying-n layer may be produced. Caution must be used, however, to take into account the change in extinction coefficient (k) of the film [184].

At present, ASE Americas uses front-side PECVD passivation and finds it gives a satisfactory result for EFG Si material. Improved IQE was seen at long wavelength region in Figure 1.6, which indicated the passivation effect in base region. It should be admitted that PECVD is not a low-cost process. Nevertheless, if the substrate contains too many defects and if double-sided deposition is permitted, an additional PECVD Si_3N_4 layer at backside needs to be considered. This layer not only provides a source of atomic hydrogen but also serves as a capping layer which blocks the hydrogen outdiffusion. Another advantage is that inserting a low-n Si_3N_4 layer between base and back contact constitutes an enhanced reflector structure that can improve the light absorption in the active region. Figure 4.14 illustrates the coherent and non-coherent components of

reflectance at Si/Buffer interface calculated as a function of wavelength corresponding to buffer layers of different *n*'s. It can be seen that, for a given thickness of the buffer layer, a lower *n* leads to a higher back reflectance. For comparison purpose, an extensive study can be found in Ref. [185] for coating materials MgF_2 and ZnO using PV Optics.

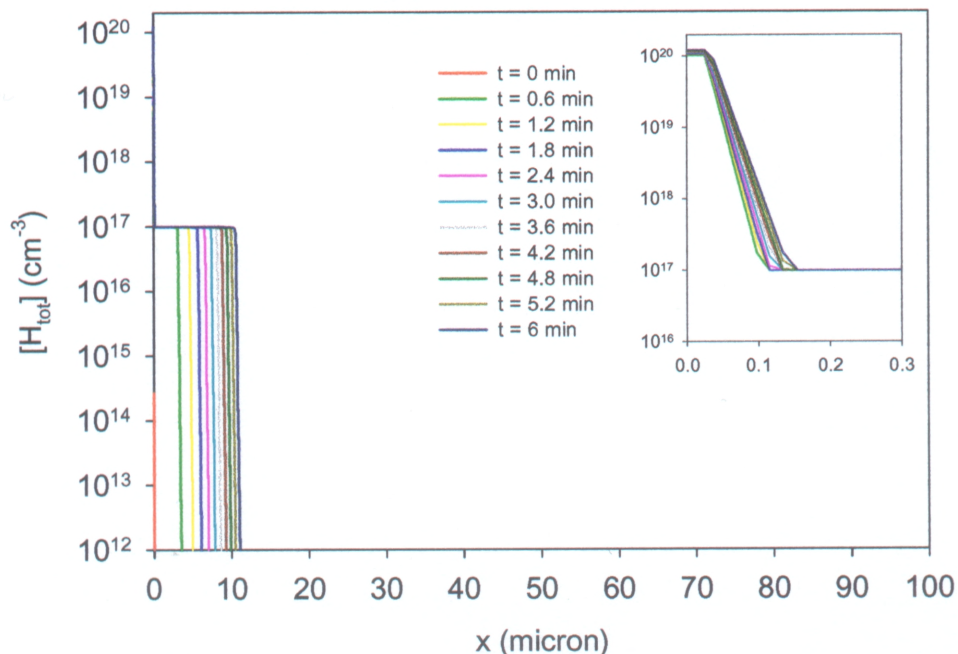

Figure 4.8 Total H concentration in predeposition at 300°C, $N_b = 10^{17}$ cm^{-3}, $C_s = 2.75 \times 10^{14}$ cm^{-3}, Rc = 10 A, k' = 0.2 s^{-1}, t = 6 min.

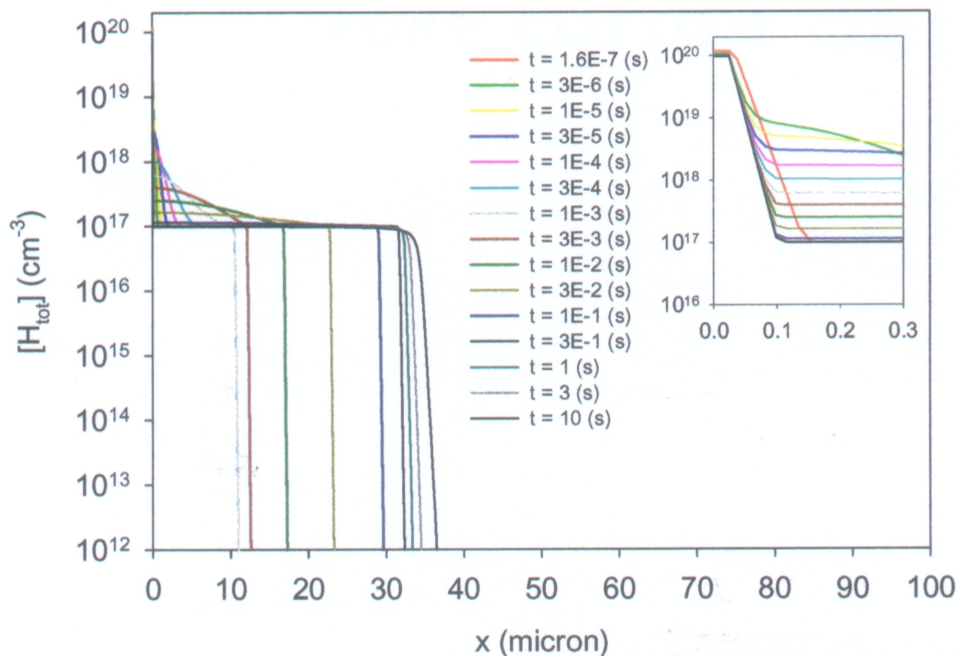

Figure 4.9 Total H concentration in 800°C anneal after 300°C predeposition, $N_b = 10^{17}$ cm^{-3}, $J_s = 0$, $R_c = 10$ A, k' = 40 s^{-1}.

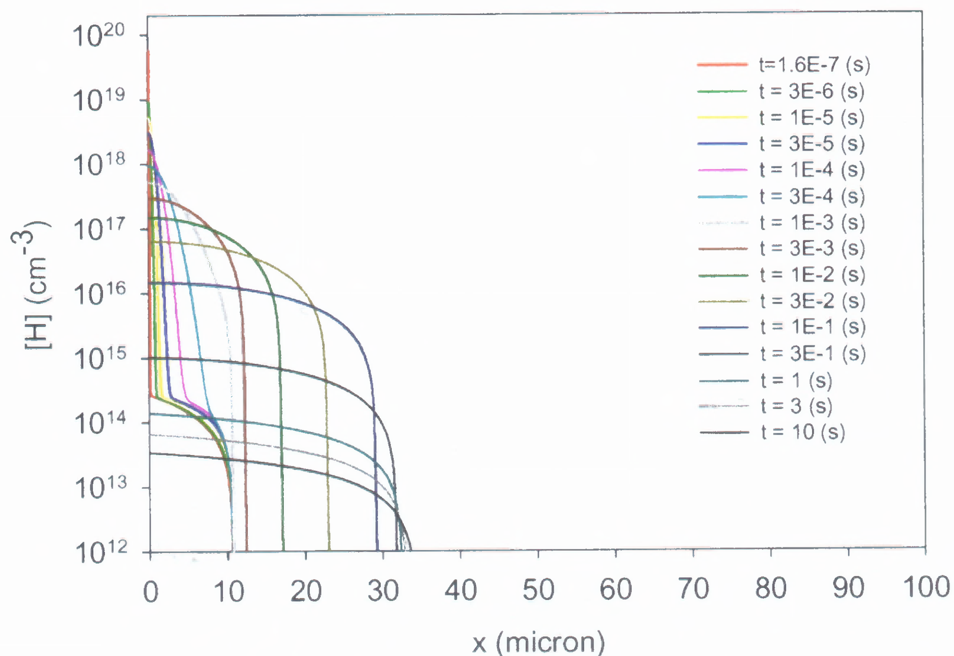

Figure 4.10 Untrapped H concentration in 800°C anneal after 300°C predeposition, $N_b = 10^{17}$ cm^{-3}, $J_s = 0$, $R_c = 10$ A, k' = 40 s^{-1}.

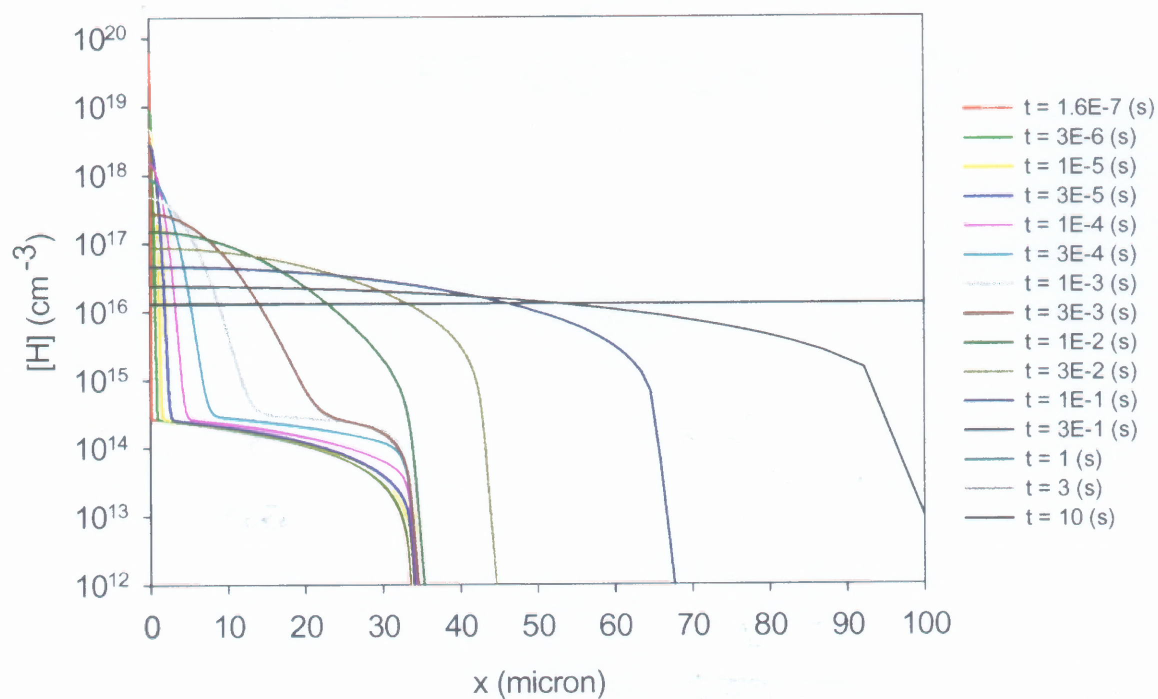

Figure 4.11 Untrapped H concentration in 800°C anneal, $N_b = 10^{16}$ cm^{-3}, $J_s = 0$, $R_c = 1$ A, k' = 40 s^{-1}.

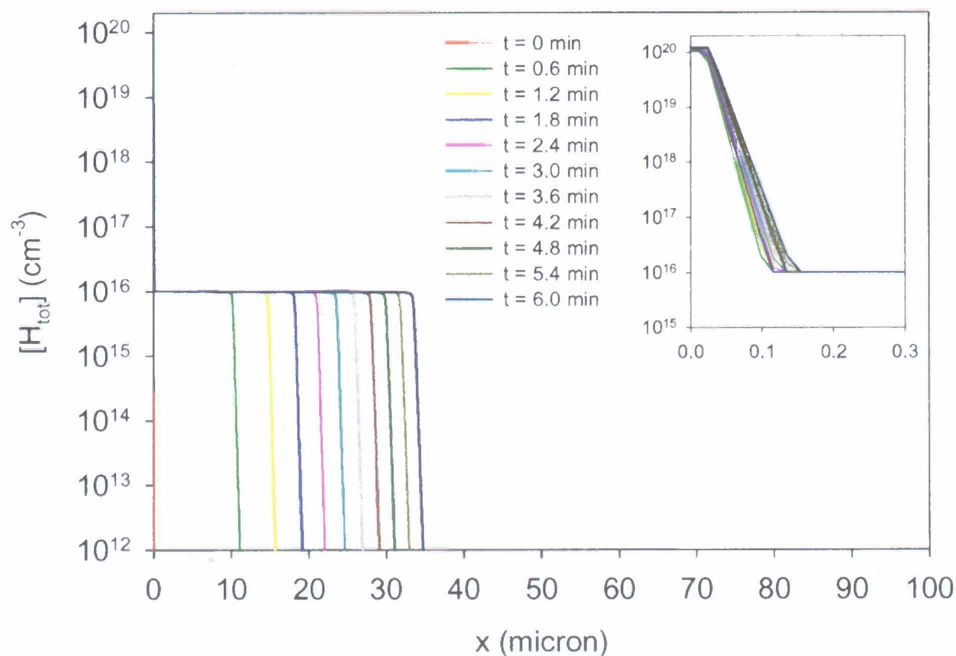

Figure 4.12 Predeposition at 300°C, $N_b = 10^{16}$ cm^{-3}, C_s=2.75 × 10^{14} cm^{-3}, R_c = 10 A, k' = 0.2 s^{-1}, t = 6 min.

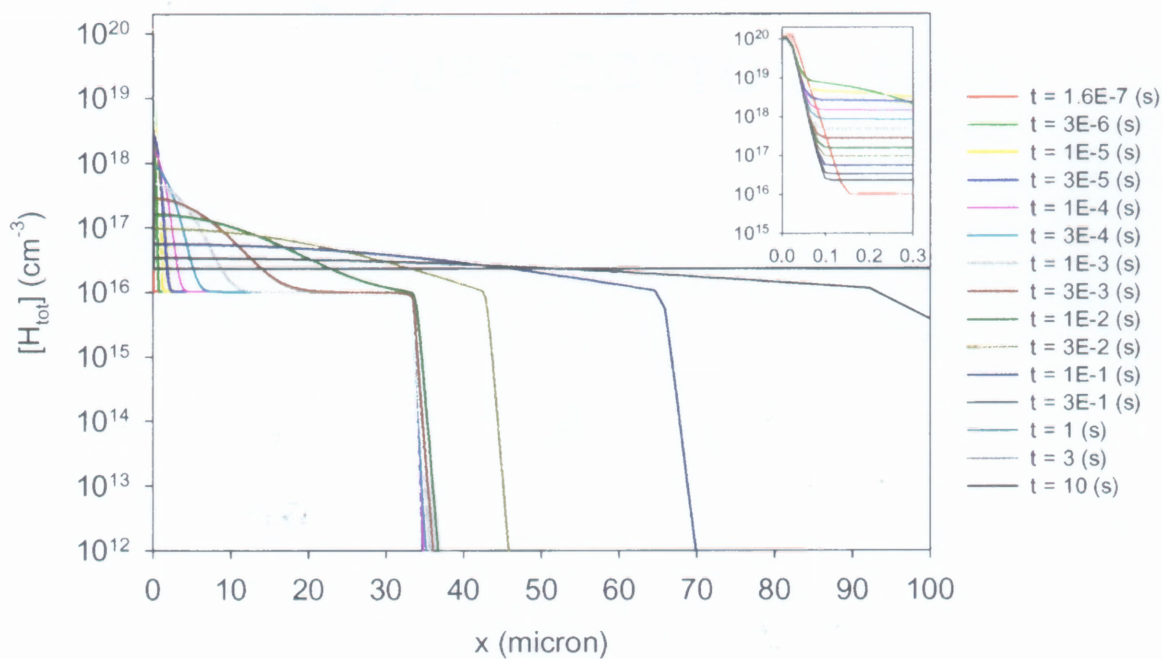

Figure 4.13 Total H concentration in 800°C anneal after 300°C predeposition, $N_b = 10^{16}$ cm^{-3}, J_s = 0, R_c = 1 A, k' = 40 s^{-1}.

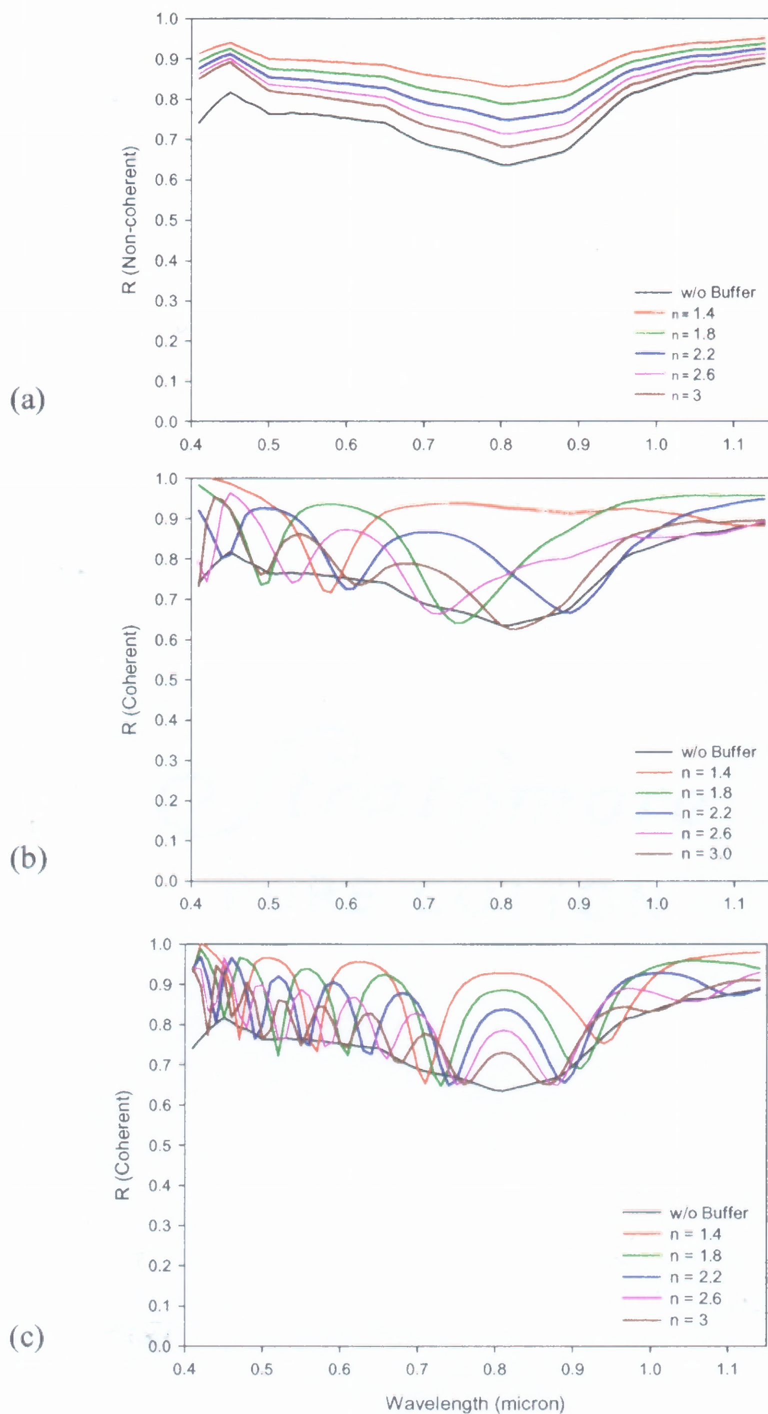

Figure 4.14 Calculated reflectance from Si/Buffer interface of Si/Buffer/Al back reflector structure. (a) shows the noncoherent component same for both 0.4- and 1.0-μm thick buffer layer. (b) and (c) show the coherent component for 0.4- and 1.0-μm thick buffer layer, respectively.

CHAPTER 5

CONCLUSIONS AND FUTURE DIRECTIONS

The purpose of this research is to develop a framework and method of modeling hydrogen diffusion in crystalline silicon and to apply the model to various hydrogen passivation techniques currently in use.

5.1 Conclusions on Hydrogen Diffusion and Process Modeling

A diffusion model was established which takes into account charge state conversion of hydrogen species, complex formation and dissociation at dopant and trap sites, mobile traps, and junction field. Carrier exchange among the various charged species is a "fast" process compared to the diffusion process. In order to evaluate their relative concentrations in a quasi equilibrium state, a simultaneous solution of Poisson's equation that involves a "negative U" impurity, e.g., hydrogen, is needed. A numerical iterative method was developed and the global convergence was proved. Time domain implicit finite difference method was adopted to solve the fully coupled equations. Several limiting versions of the model were applied to cases that are of interest to hydrogen passivation for PV. Several conclusions are summarized in this section.

Early simulation work was intended to fit hydrogen profiles to complementary error functions. But, the best-fit parameters implied a very high concentration of free hydrogen at surface, C_s, and a diffusivity, D, several orders of magnitude lower than the high temperature extrapolated values. By applying trap-limited diffusion model that assumes a constant bulk trap level and trapping / detrapping mechanisms, a better fit was obtained for plasma-deuteration of n-type Si 200°C with a lower C_s (~ 10^{14} cm^{-3}) and

high temperature extrapolated diffusivity value. It proved that, at low temperatures, complex formation and dissociation at dopant or trap sites is the controlling diffusion mechanism.

Process-induced-traps (PIT) are then included in the model. The total trap profile consists of a time dependent PIT distribution near the surface and a constant trap level in the bulk. This trap structure was found necessary to describe the various features of the evolution of diffusion profiles. Again, the simulation consistently assumed a lower surface concentration ($\sim 10^{14}$ cm^{-3}) and high temperature extrapolated diffusivity value.

In some hydrogenation processes, such as ion beam techniques, enhanced diffusion was observed in previous studies. In this study, PAS analysis revealed a higher vacancy-related open volume density in EFG silicon material than in FZ silicon material. A peak in vacancy-related open volume density depth profile was observed in implanted EFG silicon samples, but none was observed in the virgin EFG samples. These results showed a correlation between mobile traps, such as ion beam induced vacancy and vacancy clusters, and the differences in diffusion profiles of samples implanted under the same conditions. By including mobile traps in the model, further simulation studies showed that the shoulder region by the primary peak could be caused by a simultaneous redistribution of mobile traps generated during the ion implantation process. In Kaufman ion beam hydrogenation, prolonged exposure to energetic ion source can induce segregation of hydrogen at defect sites such as dislocation and grain boundaries and sometimes form self-trapping extended defects like bubbles and platelets. Since such structures usually contain a large number of hydrogen, they can greatly affect diffusion

profiles at the surface. Sometimes, surface hydrogen concentration as high as 10^{20} cm^{-3} can be observed by SIMS.

Simulation of hydrogen diffusion in p-n junction was first attempted in this work. The previously fitted C_s (~10^{14} cm^{-3}) in uniform cases was confirmed in the n-p junction data by estimating the value from detailed balance equation. Preliminary simulation results showed that charge state of hydrogen species changes dramatically across the junction depletion region. The dominant atomic hydrogen species at n or n^+ region of a junction is negatively charged, whereas p^- or p^+ region is dominated by position charged ions. In the depletion region, the built-in electric field, ~ 10^4 V/cm, causes the accumulation of H^- (H^+) ion at the n^+ (p^+) region of an n^+-p (p^+-n) junction, which can retard the diffusion. As the hydrogen diffuses through the n^+ region of an n^+-p junction, the diffusion is in the trap-limited diffusion regime. The electric field changes as the diffusion process proceeds, which in turn deviates the diffusion process from the ideal case.

PECVD Si_3N_4 deposition followed by RTP anneal has been practically used in some PV companies and can offer satisfactory passivation for silicon solar cells. Simulations in this work revealed the underlying diffusion mechanisms that match the experimental observations. Basically, PECVD step serves as hydrogen predeposition step by storing hydrogen at process-induced-trap (PIT) sites near the surface. In RTP anneal step, hydrogen is released and redistributed into the bulk region. Three steps are involved during this step: 1) release of hydrogen from surface traps, 2) bulk diffusion, and 3) if bulk trap level is high, the diffusion is stalled and controlled by trapping and detrapping in the vicinity of diffusion front. If the bulk step is low or sample is thin

enough, hydrogen may penetrate the sample without step 3. Otherwise, the final passivation depth is strongly controlled by the bulk trap density and the total amount of trapped hydrogen in the predeposition step.

By changing process parameters, PECVD Si_3N_4 film can have an adjustable refractive index (n) ranging from 1.87 to 2.93. This effect may be used to form double layer AR coating (DLAR) or a varying-n layer to enhance the light absorption in the active region. However, process optimization must consider excessive absorption due to an increase in extinction coefficient (k) of a high-n Si_3N_4 film. If cost permits, a backside PECVD Si_3N_4 layer may be used as an additional atomic hydrogen source and as a capping layer to block hydrogen outdiffusion. Inserting a low-n Si_3N_4 layer between base and back contact also constitutes an enhanced reflector that can reduce loss of light at back contact.

5.2 Future Directions

The future work may consider the following:

1. Although several hydrogenation-induced defects have been identified, more research is needed to identify other process-induced traps and their capture cross sections for hydrogen.
2. More PAS analysis is needed to investigate samples after RTP process. This will show how vacancy-type mobile traps migrate and interact with diffusing hydrogen species.

3. Simulation of hydrogen diffusion in p-n junction was initiated in this work. If more computation resources are available, a thorough simulation will be extremely useful to gain more insight.
4. The implementation of the diffusion model is based on finite different discretization and is applicable to 3-D modeling cases. A fundamental study on its implementation based on finite element discretization will be essential if the model is to simulate a 3-D problem with complicated structure.
5. More detailed analyses need to be done to determine optimum process(es) for PECVD passivation. The analyses should take into account indiffusion as well as outdiffusion during RTP process.

REFERENCES

1. U.S. Department of Energy Photovoltaics Program, *History: PV Timeline*, http://www.eren.doe.gov/pv/history.html (17 December 2001).

2. H. J. Hovel, *Solar Cells*, in R. K. Willardson and A. C. Beer, Eds., *Semiconductors and Semimetals*, Vol. **11**, Academic, New York, 1975, p. 3.

3. Z. Chen, A. Rohatghi, R. O. Bell and J. P. Kalejs, Appl. Phys. Lett. **65**, 1331 (1994).

4. *Principal Conclusions of the American Physical Society Study Group on Solar Photovoltaic Energy Conversion*, American Physical Society, New York, 1979.

5. K. J. Bachmann, "Material Aspects of Solar Cells" in E. Kaldis, Ed., *Current Topics in Material Science*, Vol. **3**, North-Holland, Amsterdam, 1979.

6. S. M. Sze, *Physics of Semiconductor Devices*, John Wiley & Sons, New York, 1981, p. 795.
7. M. B. Prince, "Silicon Solar Energy Converters," J. Appl. Phys., **26**, 534 (1955).

8. M. A. Green, *Solar Cells*, Prentice-Hall, 1982, p. 80.

9. M. A. Green, *Solar Cells*, Prentice-Hall, 1982, p. 96.

10. R. M. Swanson, Solar Cells **17**, 85 (1986).

11. A. Wang, J. Zhao and M.A. Green, Appl. Phys. Lett. **57**, 602 (1990).

12. M. A. Green, et al., IEEE Trans. on Elec. Dev. **37**, 331, (1990).

13. C. Z. Zhou, P. J. Verlinden, R. A. Crane and R. M. Swanson, *Proceedings of the 26th IEEE Photovoltaic Specialists Conference*, Anaheim, September 29 - October 3, 1997, p. 287.

14. B. A. Smith, Aviation Week & Space Technology **155**, no. 8, 47 (2001).

15. J. P. Benner, *10th Workshop on Crystalline Silicon Solar Cell Materials and Processes: Extended Abstracts and Papers* from the Workshop held 14-16 August 2000, Copper Mountain, Colorado, p. 3.

16. T. Saitoh, *11th Workshop on Crystalline Silicon Solar Cell Materials and Processes: Extended Abstracts and Papers* from the Workshop held 19-22 August 2001, Estes Park, Colorado, p. 40.

17. V. V. Voronkov, J. Crystal Growth **59**, 625 (1982).

18. V. V. Voronkov, G. I. Voronkova, N. V. Veselovskaya, M. G. Milvidskii and I. F. Chervonyi, Sov. Phys. Crystallography **29**, 688 (1998).

19. X. Deng and B. L. Sopori, Mat. Res. Soc. Symp. Proc. Vol. **378**, 359 (1995).

20. A. Zunger, Ann. Rev. Mater. Sci. **15**, p.411 (1981).

21. J. Lagwoski, P. Edelman, A. M. Kontkiewicz, O. Milic, W. Henley, M. Dexter, L. Jastrzebski and A. M. Hoff, Appl. Phys. Lett. **63**, 3043 (1993).

22. G. Zoth and W. Berghola, J. Appl. Phys. **67**, 6764 (1990).

23. H. Indusekhar and V. Kumar, J. Appl. Phys. **61**, pp. 1449-1455 (1987).

24. E. R. Weber, A. A. Istratov, S. A. Mchugo, H. Hieslmair, C. Flink, "Minority Carrier Diffusion Length Degradation in Silicon: Who is the Culprit?" *Recombination Lifetime Measurements in Silicon, ASTM STP 1340*, edited by D.C.Gupta, F. R. Bacher, and W. M. Hughes, American Society for Testing and Materials, p. 18 (1998).

25. S. Mahajan and K. S. Sree Harsha, *Principles of Growth and Processing of Semiconductors*, MsGraw-Hill, Chapter 3 (1999).

26. H. F. Mataré, " Carrier Transport at Grain Boundaries in Semiconductors", J. Appl. Phys. **56**, pp. 2605-2631 (1984).

27. B. L. Sopori, *19th International Conference of Defects in Semiconductors. ICDS 19, July 1997, Aveiro, Portugal, Mat. Sci. Forum* Vol. **258-263**, pt.1, p.527-34.

28. W. Shockley and W. T. Read, Phys. Rev. **87**, 835 (1952).

29. J. G. Fossum and E. L. Burgess, Appl. Phys. Lett. **33**, 238 (1978).

30. C. H. Seager and D.S. Ginley, J. Appl. Phys. **52**, 1050 (1981).

31. H. E. Ghitanio and S. Martinuzzi, Mat. Sci. and Eng. **B4**, 153 (1989).

32. J. Pankove, N. M. Johnson, *Semiconductors and Semimetals* (Academic Press Inc., 1991) p. 34.

33. J. I. Hanoka, C.H. Seager, D.J. Sharp, and J.K. Panitz, Appl. Phys. Lett. **42**, 618 (1983).

34. L. L. Kazmerski, J. Vac. Sci. Technol. **A3(3)**, 1385 (1985).

35. S. J. Pearton, J. W. Corbett, M. Stavola, *Hydrogen in Crystalline Semiconductors,* Springer Series in Materials Science **16** (Springer-Verlag, 1992) pp. 153-183.

36. N. H. Nickel, N. M. Johnson, and W. B. Jackson, Appl. Phys. Lett. **62**, 3285 (1993).

37. H. E. Elgamel, A. Rohatgi, Z. Chen, C. Vinckier, J. Nijs, and R. Mertens, in IEEE Trans. Elec. Dev., 1323 (1994).

38. P. Sana, A. Rohatgi, J. Kalejs and R. O. Bell, Appl. Phys. Lett. **64**, 111 (1994).

39. L. Cai, and A. Rohatgi, in IEEE Trans. Elec. Dev. **44**, 97 (1997).

40. B. L. Sopori, X. Deng, J. P. Benner, A. Rohatghi, P. Sana, S. K. Estreicher, Y. K. Park, and M. A. Roberson, Solar Energy Materials and Solar Cells, **41/42**, 159 (1996).

41. P. Sana and A. Rohatgi, Appl. Phys. Lett. **64**, 97 (1994).

42. L. Ammor, M. Sebbar, M. Zehaf, H. Amzil and S. Martinuzi, in *Poly- Micro-Crystalline and Amorphous Semiconductors,* 77 (1984).

43. M. I. Symko, B. L. Sopori, R. Reedy and K. M. Jones, Mat. Sci. Forum, Vols. **258-263**, pp. 191-196 (1997).

44. Summary Report, *10th Workshop on Crystalline Silicon Solar Cell Materials and Processes, Editor: B. L.Sopori (* Workshop held 14-16 August 2000, Copper Mountain, Colorado).

45. N. M. Johnson, *Hydrogen in Semiconductors, Semiconductors and Semimetals*, Vol. **34**, edited by J. I. Pankove and N. M. Johnson, Academic Press, Inc, 1991, p. 37.

46. J. D. Bernstein, S. Qin, C. Chan and T-J King, IEEE Trans. Elec. Dev. **43**, no. 11, 1876 (1996).

47. C. M. Park, J. H. Jeon, J. S. Yoo and M. K. Han, Mat. Res. Soc. Symp. Proc. **471**, 167 (1997)

48. A. Matsuda and K. Tanaka, J. Appl. Phys. **60**, 2351 (1986).

49. B. M. Abdurakhmanov, R. R. Bilyalov, Renewable Energy **6**, No. 3, 303 (1995).

50. E. Katz, M. Koltun and L. Polyak, Diffusion and Defect Data. Pt. B, Solid State Phenomena. **51/52**, 479 (1996).

51. H. R. Kaufman, J., Vac. Sci. Technol. **15**, 272 (1978).

52. H. V. Boenig, *Fundamentals of Plasma Chemistry and Technology*, Technomic, Lancaster (1988), pp. 382-400.

53. D. J. Sharp, J. K. G. Panitz and D. M. Mattox, J. Vac. Sci. Technol. **16**, 1879 (1979).

54. C. Dube and J. I. Hanoka, Appl. Phys. Lett. **45**, 1137 (1984).

55. Y. S. Tsuo and J. Milstein, Appl. Phys. Lett. **45**, 971 (1984).

56. J. M. Heddleson, M. W. Horn and S. J. Fonash, J. Vac. Sci. Technol. **B6**, 280 (1988).

57. B. L. Sopori, K. M. Jones, X. Deng, R. Matson, M. Al-Jassim, S. Tsuo, A. Doolittle and A. Rohatgi, *Hydrogen in silicon: diffusion and defect passivation*. 22th IEEE Photovoltaic Specialists Conference 1991, 7-11 Oct. 1991, Las Vegas, NV, USA. New York, NY, 1991, Vol. **2**, pp. 833-41.

58. S. Wolf and R. N. Tauber, *Silicon Processing for the VLSI era, Vol. 1: Process Technology*, Lattice press, Sunset Beach, California (1986), p. 195.

59. H. E. A. Elgamel, IEEE Trans. Elec. Dev. **45**, 2131 (1998).

60. N. M. Johnson and M. D. Moyer, Appl. Phys. Lett. **46**, 787 (1985).

61. W. L. Fite, *Chemical Reactions in electric Discharges*, Ed., B. D. Blaustein. Amer. Chem. Soc., Washington D. C., Chapter 1.

62. C. H. Seager, D. J. Sharp and J. K. G. Panitz, J. Mater. Res. **2**, 96 (1987).

63. Yablonovich, D.L. Allara, C.C. Chang, T. Gmitter, and T.B. Bright, Phys. Rev. Lett. **57**, 249 (1986).

64. A. J. Tavendale, A. A. Williams and S. J. Pearton, Appl. Phys. Lett. **48**, 590 (1986).

65. P. Balk, *Extended Abs., Electronics Div.; Electrochem. Soc.* **14**, 237 (1965).

66. N. M. Johnson, D. K. Biegelsen, and M. D. Moyer, J. Vac. Sci. Technol. **19(3)**, 390 (1981).

67. E. H. Nicollian and J. R. Brews, *MOS (Metal Oxide Semiconductor) Physics and Technology*, John Wiley, New York, NY (1982), p. 781.

68. I. Lundstrom, M. S. Shivaraman and C. Svenson, J. Appl. Phys. **46**, 3876 (1975).

69. K. L. Brower, Phys. Rev. B **38**, 9657 (1988).

70. A. H. Edwards, J. Non-crystal. Sol. **187**, pp. 232-243 (1995).

71. H. A. Kurtz and S. P. Karna, J. Phys. Chem. A **104**, pp. 4780-4784 (2000).

72. M. I. Symko, B.L. Sopori, R.Reedy, K. Jones, and R. Matson, *International Conference on Defects in Semiconductors* (ICDS) (1997).

73. A. Marwick, Met. Trans. A **20A**, 2627.

74. J. Bird and J. Williams, *Ion Beam for amaterials Analysis*. Academic Press, Sydney (1989).

75. C. T. Sah, J. Y. C. Sun and J. J. T. Tzou, Appl. Phys. Lett. **43**, 204 (1983).

76. J. W. Corbett, D. Peak, S. pearton,and A. G. Sganga, *Hydrogen in Disordered and Amorphous Silicon*, NATO ASI Series B, Physics, **136**, Editors Gust Bambakidis, R. C. Bowman Jr., Plenum Press, 1986, p. 61.

77. S. Picraux and F. Vook, Phys. Rev. B **18**, 2066 (1978).

78. B. D. Patterson, Rev. Mod. Phys. **60**, 69 (1988).

79. S. Estreicher, Phys. Rev. B **36**, 9122 (1987).

80. P. Deak, L. C. Snyder, J. L. Lindstrom, J. W. Corbett, S. J. Pearton, and A. J. Tavendale, Phys. Lett. A **126**, 427 (1988).

81. K. Bonde Nielson, B. Bech Nielsen, J. Hansen, E. Andersen and J. U. Andersen, Phys. Rev. B **60**, 1716 (1999).

82. S. R. Kreitzman, B. Hitti, R. L. Lichti, T. L. Estle and K. H. Chow, Phys. Rev. B **51**, 13117 (1995).

83. F. Buda, G. L. Dhiarotti, R. Car and M. Parrinello, Phys. Rev. Lett. **63**, 294 (1989).

84. Y. V. Gorelkinskii and N. N. Nevinnyi, Mat. Sci. Engr. B **36**, 133 (1996).

85. C. G. Van de Walle, P. J. H. Denteneer, Y. Bar-Yam, and S. T. Pantelides, Phys. Rev. B **39**, 10791 (1989).

86. K. B. Nielsen and B. B. Nielson, Mat. Sci. Engr. B **36**, 133 (1999).

87. N. M. Johnson, C. Herring and C. G. Van de Walle, Phys. Rev. Lett. **73**, 130 (1994).

88. C. H. Seager, R. A. Amderson and S. K. Estreicher, Phys. Rev. Lett. **74**, 4565 (1995).

89. S. K. Estreicher, J. L. Hastings and P. A. Fedders, Appl. Phys. Lett. **70**, 432 (1997); J. L. Hastings, S. K. Estreicher and P. A. Fedders, Phys. Rev. B **56**, 10215 (1997).

90. M. Budde, B. B. Nielson, P. Leary, J. Goss, R. Jones, P. R. Briddon, S. Öberg and S. J. Breuer, Phys. Rev. B **57**, 4397 (1998).

91. C. H. Seager and D. S. Ginley, Appl. Phys. Lett. **34**, 337 (1979).

92. N. M. Johnson, *Hydrogen in Semiconductors, Semiconductors and Semimetals*, Vol. **34**, edited by J. I. Pankove and N. M. Johnson, Academic Press, Inc, 1991, p. 98.

93. N. V. Harrick, *Internal Reflection Spectroscopy*, Wiley, New York (1967).

94. N. M. Johnson, Phys. Rev. B **31**, 5525 (1985).

95. T. Zundel and J. Weber, Phys. Rev. B **39**, 13549 (1989).

96. N. M. Johnson, Mat. Res. Soc. Symp. Proc. **68**, 381 (1986).

97. K. Bergman, M. Stavola, S. J. Pearton and J. Lopata, Phys. Rev. B **37**, 2770 (1988).

98. K. Bergman, M. Stavola, S. J. Pearton and T. Hayes, Phys. Rev. B **38**, 9643 (1988).

99. S. B. Zhang and D. J. Chadi, Phys. Rev. B **41**, 3882 (1990).

100. J. Zhu, N. M. Johnson and C. Herring, Phys. Rev. B **41**, 12354 (1990).

101. R. Gale, F. J. Feigl, C. W. Magee and R. D. Young, J. Appl. Phys. **54**, 6938 (1983).

102. S. J. Pearton and A. J. Tavendale, J. Phys. C. Solid St. Phys. **17**, 6701 (1984).

103. R. Singh, S. J. Fonash and A. Rohatgi, Appl. Phys. Lett. **49**, 800 (1986).

104. S. J. Pearton and A. J. Tavendale, J. Appl. Phys. **54**, 1375 (1983).

105. S. J. Pearton and A. J. Tavendale, Phys. Rev. B **26**, 7105 (1982a).

106. M. Stavola, *7th Workshop on the Role of Impurities and Defects in Silicon Device Processing*, NREL/CP-520-23386 (1997), p. 63.

107. J. Weber in *MRS Proc.* **513** (1998).

108. J. U. Sachse, E. Ö. Sveinbjörnsson, N. Yarykin and J. Weber, Mat. Sci. Engr. B **58**, 134 (1999).

109. R. Jones, S. Öberg, J. Goss, P. R. Briddon and A. Resende, Phys. Rev. Lett. **75**, 2734 (1995); A. Resende, R. Jones, S. Öberg and P. R. Briddon, Phys. Rev. Lett. **82**, 2111 (1999).

110. R. E. Pritchard, M. J. Ashwin, J. H. Tucker, R. C. Newman, E. C. Lightowlers, M. J. Binns, S. A. MacQuaid and R. Falster, Phys. Rev. B **56**, 13118 (1997); R. C. Newman, R. E. Pritchard, J. H. Tucker and E. C. Lightowlers, Phys. Rev. B **60**, 12775 (1999).

111. V. P. Markevich and M. Suezawa, J. Appl. Phys. **83**, 2988 (1998).

112. Van Vieringen and N. Warmoltz, Physica **22**, 849 (1956).

113. T. Ichimiya and A. Furuichi, Int. J. Appl. Rad. Isotopes **19**, 573 (1968).

114. C. H. Seager and R. A. Anderson, Appl. Phys. Lett. **53**, 1181 (1989).

115. A. Chari, P. de Mierry and M. Aucoxturier, *Proc 7th E. C. Photovoltaic Solar Energy Conf., Seville, CEC, Paris*, p. 995 (1986).

116. W. L. Hansen, S. J.Pearton, and E. E.Haller, Appl. Phys. Lett. **44**, 606 (1984).

117. N. M. Johnson, Hydrogen in Semiconductors, *Semiconductors and Semimetals*, Vol. **34**, edited by J. I. Pankove and N. M. Johnson, Academic Press, Inc, 1991, pp. 293.

118. S. J. Pearton, *13th International Conference on Defects in Semiconductors*, eds., L.C. Kimerling and J. M. Parsey, Jr., Metallurgical Soc. A.I.M.E., p. 737.

119. A. Mogro-Campero, R. P. Love, and R. Schubert, J. Electrochem. Soc. **132**, 2006 (1985).

120. N. M. Johnson, C. Herring, and D. J. Chadi, Phys. Rev. Lett. **56**, 769 (1986).

121. N. M. Johnson, C. Herring, *Inst. Phys. Conf.* Ser. **95**, 415 (1989).

122. M. Capizzi and A. Mittiga, Appl. Phys. Lett. **50**, 918 (1987).

123. B. L. Sopori, K. Jones, X. J. Deng, Appl. Phys. Lett. **61**, 2560 (1992).

124. P. W. Anderson, Phys. Rev. Lett. **34**, 953 (1975).

125. M. von Smoluchowski, Phys. Z. **17**, 585 (1916).

126. H. Reiss , C. S. Fuller, and F. J. Morin, Bell System Tech. J. **35**, 535 (1956).

127. Rose, A., *Concepts in Photoconductivity and Allied Problems*, Huntington, NY: Robert E. Krieger Publishing Co., 1978, Chapter 7, pp. 121-128.

128. M. Lax, Phys. Rev. **119**, 1502-1523 (1960).

129. J. S. Makris and B. J. Master, J. Electrochem. Soc. **120**, 1252 (1973).

130. A. Bourret, *13th International Conference on Defects in Semiconductor*, L. C. Kimerling and J. M. Parsey eds, The Metallurgical Society of the AIME, Warrendale, PA, 129.

131. M. A. Roberson, and S. K. Estreicher , Phys. Rev. B **49**, 17040 (1994).

132. Y. K. Park, S. Etreicher and C. W. Myers, Phys. Rev. B **52**(3), 1718 (1995).

133. S. K. Estreicher, J. L. Hastings and P. A. Fedders, Mat. Sci. Eng. B **58**, 31 (1999).

134. G. D. Watkins, *Deep Centers in Semiconductors*, in: S. T. Pantelides (Ed.) Gordon and Beach, New York, NY, 1986.

135. G. D. Watkins, J. W. Corbett, Phys. Rev. **138**, A543 (1965).

136. G. D. Watkins, in *Deep Centers in Semiconductors*, (edited by S.T., 1990).

137. C. G. Van de Walle, Phys. Rev. B **49**, 4579 (1994).

138. B. N. Mukashev and S. Tokmoldin, Mat. Sci. Forum **196-201**, pp. 843-848 (1995).

139. B. B. Nielsen, l. Hoffman, M. Budde, R. Jones, J. Goss, and S. Oberg, Mat. Sci. Forum **196-201**, pp. 933-938 (1995).

140. J. W. Corbett and J. L. Lindström, Solar Cells **24**, 127 (1988).

141. R. Rizk, P. de Mierry, D. Ballutaud, M. Aucouturier, and D. Mathiot, Phys. Rev. B **44**, 6141 (1991).

142. S. J. Pearton, Mat. Sci. Eng. B **23**, 130 (1994).

143. E. M. Pell, J. Appl. Phys. **31**, 291 (1960).

144. M. Capizzi and A. Mittiga, Physica **146B**, 19 (1987).

145. D. Mathiot, Phys. Rev. B **40**, 5867 (1989).

146. J. P. Kalejs and S. Rajendran, App. Phys. Lett. **55**, 25 (1989).

147. J. T. Borenstein, D. Tulchinski and J. W. Corbett, Mat. Res. Soc. Symp. Proc. Vol. **63**, 633 (1990).

148. D. T. Tulchinsky and J. W. Corbett, Phys. Rev. B **42**, 11881 (1990).

149. L. P. Korpas, J. W. Corbett, and S. K. Estreicher, Phys. Rev. B **46**, 12365 (1992).

150. J. T. Borenstein, J. W. Corbett and S. J. Pearton, J. Appl. Phys. **73**, 2751 (1993).

151. N. M. Johnson, *Hydrogen in Semiconductors, Semiconductors and Semimetals*, Vol. **34**, edited by J. I. Pankove and N. M. Johnson, Academic Press, Inc, 1991, Chapter 10.

152. H. K. Gummel, IEEE Trans. Elec. Dev. **ED-11**, 455 (1964).

153. T. I. Seidman and S. C. Choo, Solid-State Electron. **15**, 1229 (1972).

154. M. S. Mock: *Analysis of Mathematical Models of Semiconductor Devices*. Dublin: Boole Press 1983.

155. *PISCES-II Input Specification*, TCAD group, Stanford University.

156. S. Selberherr, *Analysis and Simulation of Semiconductor Devices*, Springer-Verlag / Wien New York, 1984, p. 211.

157. I. D. Mayergoyz, J. Appl. Phys. **59**, 195 (1985).

158. R. P. Brent, *Algorithms for Minimization without Derivatives* (Englewood Cliffs, NJ: Prentice Hall 1973), Chapter 3 and 4.

159. A. B. Vasil'eva and V. G. Stel'makh, Zh. Vychisl. Mat. Mat. Fiz. **17**, 339 (1977).

160. J. Crank and P. Nicolson, Proc. Camb. phil. Soc. Math. Phys. Sci. **43**, 50 (1947).

161. T. Zundel and J. Weber, Phys. Rev. B **46**, 2071 (1992)

162. B. Y. Tong, X, W, Wu, G. R. Yong, and S. K. Wong, Can. J. Phys. **67**, 379 (1989).

163. A. Mayer, Solid St. Technol. **15**, 38 (1972).

164. Z. Chen, K. Yasutake, A. Doolittle, and A. Rohatgi, Appl. Phys. Lett. **63**, 2117 (1993).

165. B. L. Sopori and Y. Zhang, *Proc. NCPV Review*, Oct. 14—17, 2001, Lakewood, Colorado.

166. H. V. Boenig, *Plasma Science and Technolgy*. Cornell University Press, Ithaca, NY.

167. N. M. Johnson, *Hydrogen in Semiconductors, Semiconductors and Semimetals*, vol. **34**, edited by J. I. Pankove and N. M. Johnson, Academic Press, Inc, 1991, pp. 329.

168. J. I. Pankove, C. W. Magee, and R. O. Wance, Appl. Phys. Lett. **47**, 748 (1985).

169. N. M. Johnson, *Hydrogen in Semiconductors, Semiconductors and Semimetals*, Vol. **34**, edited by J. I. Pankove and N. M. Johnson, Academic Press, Inc, 1991, pp. 313.

170. M. Symko, *Hydrogen Diffusion Mechanisms in Silicon Solar Cells*, Ph. D. Dissertation, University of Denver, 1998.

171. Per discussion with Dr. B. L. Sopori, cell efficiency was seen to increase after FGA treatment of solar cells in Dr. A. Rohatgi's team at Georgia Tech.

172. M. W. Horn, J. M. Heddleson and S. J. Fonash, Appl. Phys. Lett. **51**, 490 (1987).

173. X. Deng, Ph.D dissertation, T-4386, Colorado School of Mines.

174. N. M. Johnson, C. Herring, C. Doland, J. Walker, G. Anderson, and F. Ponce, *Mat. Sci. Forum*, Vol. **83-87**, 33 (1992).

175. B. L. Sopori, Y. Zhang, and N. M. Ravindra, J. Electronic Mat. **30**, pp. 1616-1628 (2001).

176. S. Muto, Mat. Sci. Forum, Vol. **143-147**, 879 (1994).

177. B. L. Sopori, T. Q. Zhou and G. A. Rozgonyi, *Defect Generation/Passivation by Low Energy Hydrogen Implant for Silicon Solar Cells*. Conference Record of the 21th IEEE Photovoltaic Specialists Conference – 1990, Kissimmee, Florida, May 21-25, 1990, New York, pp. 644-649.

178. B. L. Sopori, "Back-side hydrogenation technique for defect passivation in silicon solar cells", US patent # 05304509, issued 04/19/1994.

179. A. Rohatgi, Georgia Institute of Technology, private communications.

180. M. Ghannam, G. Palmers, H. E. Elgamel, J. Nijs, R. Mertens, R. Peruzzi, and D. Margadonna, Appl. Phys. Lett. **62**, 1280 (1993).

181. P. Sana, A. Rohatgi, J. P. Kalejs, and R. O. Bell, Appl. Phys. Lett. **64**, 97 (1994).

182. S. Winderbaum,, F. Yun, S. O. Martin, A. Marriage and O. Reinhold, *Proceedings of the 33rd Annual Meeting of the Australian and New Zealand Solar Energy Society (ANZSES Solar'95)*, Hobart, Tasmania, 29 November-2nd December, 1995.

183. J. Caughman, D. Beach, J. Jellison, W. Gardner, and H. B. George, in *46th AVS National Symposium*, Seattle, Washington, October 25, 1999.

184. Per discussion with Dr. B. L. Sopori, extinction coefficient (k) increases as the refractive index (n) of PECVD silicon nitride film increases.

185. B. L. Sopori, J. Madjdpour, Y. Zhang, W. Chen, S. Guha, J. Yang, A. Banerjee, and S. Hegedus, *MRS Spring 99 Meeting, April 5-9, 1999, San Francisco.*